# On Vibrations in the Gerbil Middle Ear Under Static Pressures

**Orhun Kose**

Graduate Program in Biological

and Biomedical Engineering

McGill University, Montréal

April 2022

A thesis submitted to McGill University

in partial fulfillment of the requirements of the degree of

Doctor of Philosophy

*to my mother Gulsen and father Faruk, my hero and teacher*

*to my wife Saba, my heart*

*and to my son Alp, my soul*

# Abstract

Tympanometry is a clinical test that records the response of the ear to sound during large air-pressure sweeps, to determine the status of the external and middle ear. The acoustical and mechanical response of the ear during this test is not well understood. To help improve our understanding, in this thesis we investigate the effects of quasi-static pressures on vibrations of the gerbil eardrum. Using a single-point laser Doppler vibrometer (LDV), the vibration magnitudes at several locations on the eardrum were measured. A pressurization cycle included decreasing the middle-ear pressure from 0 Pa to −2500 Pa, increasing it back to 0 Pa, increasing it to +2500 Pa, and then decreasing it back to 0 Pa. The acoustic input was a linear chirp ranging from 0.5 to 10 kHz.

The first experimental study used a step-wise pressurization protocol in which the pressure was changed in 500-Pa increments and held constant for 10 s at each step. The low-frequency vibration magnitude decreased for both negative and positive pressures, with larger changes at smaller pressures; the magnitudes were smaller for negative middle-ear pressures than for the corresponding positive ones. At zero middle-ear pressure, as the frequency increased the vibration magnitude initially increased slightly up to a broad peak (R1), but as the pressure was made more negative the low-frequency vibration magnitude became constant with frequency and later decreased with frequency, and R1 shifted to slightly higher frequencies. R1 was visible at all locations for small pressures, and on the manubrium it was also visible for larger negative pressures. There was a magnitude dip around −1000 to −1500 Pa. A higher-frequency peak (R2) shifted gradually for large pressures, and was visible at all locations; it was seen as a cluster of peaks on the pars tensa. A small low-frequency peak at about 0.7 kHz was only visible on the pars flaccida. The overall vibration magnitude at the umbo was slightly higher than at mid-manubrium. The largest vibration magnitudes were observed on the posterior pars tensa. The frequency response on the pars flaccida was smooth near ambient pressure, similar to that at the umbo, but it changed rapidly when pressurized, already displaying a series of pronounced peaks and troughs by ±500 Pa.

The second experimental study used a continuous pressure sweep instead of steps, with the same overall cycle duration as in the first study. The response behaviours were similar to those seen for pressure steps but many more details could be observed. For example, the magnitude dip started near R2 and then expanded quickly to frequencies below that peak. A trough on the posterior pars tensa, which shifted in a way similar to R2, appeared as a peak on the anterior pars tensa.

A previous finite-element model, which simulated responses to both sounds and large quasi-static pressures, was further developed to accommodate both pressure steps and pressure sweeps. The simulation results were compared with our data and with data from other groups. The model replicates some of the experimentally observed behaviours but there are some discrepancies.

Collectively these experimental and modelling studies will ultimately lead to being able to extract more information from tympanometry and thus to improvements in clinical decision making.

# Résumé

La tympanométrie est un test auditif qui enregistre la réponse de l'oreille au son lors de grands balayages de pression d'air, afin de déterminer l'état de l'oreille externe et moyenne. La réponse acoustique et mécanique de l'oreille au cours de ce test n'est pas bien comprise. Pour aider à améliorer notre compréhension, dans cette thèse on étudie les effets des pressions quasi-statiques sur les vibrations du tympan de la gerbille. À l'aide d'un vibromètre laser Doppler (LDV) à point unique, les amplitudes de vibration à plusieurs endroits sur le tympan ont été mesurées. Un cycle de pressurisation consistait à diminuer la pression de l'oreille moyenne de 0 Pa à −2 500 Pa, à l'augmenter à nouveau à 0 Pa, à l'augmenter à +2 500 Pa, puis à la réduire à 0 Pa. L'entrée acoustique était un bip ('chirp') linéaire allant de 0,5 à 10 kHz.

La première étude expérimentale a utilisé un protocole de pressurisation transitoire dans lequel la pression était modifiée par incréments de 500 Pa et maintenue constante pendant 10 s pour chaque incrément. L'amplitude des vibrations à basse fréquence a diminué pour les pressions négatives et positives, avec des changements plus importants à des pressions plus faibles ; les amplitudes étaient plus faibles pour les pressions négatives de l'oreille moyenne que pour les pressions positives correspondantes. À une pression de l'oreille moyenne nulle, à mesure que la fréquence augmentait, l'amplitude des vibrations augmentait initialement légèrement jusqu'à un large pic (R1), mais à mesure que la pression devenait plus négative, l'amplitude des vibrations à basse fréquence devenait constante avec la fréquence et diminuait plus tard avec la fréquence, et R1 s'est déplacé vers des fréquences légèrement plus élevées. R1 était visible à tous les endroits pour les faibles pressions; sur le manubrium, il était également visible pour les pressions négatives plus importantes. Il y a eu une baisse d'amplitude d'environ −1000 à −1500 Pa. Un pic de fréquence plus élevée (R2) s'est déplacé progressivement pour les fortes pressions et était visible à tous les emplacements ; il a été vu comme un groupe de pics sur la pars tensa. Un petit pic de basse fréquence à environ 0,7 kHz n'était visible que sur la pars flaccida. L'amplitude globale des vibrations à l'umbo était légèrement plus élevée qu'à mi-manubrium. Les plus grandes amplitudes de vibration ont été observées sur la pars tensa postérieure. La réponse en fréquence sur la pars flaccida était lisse près de la pression ambiante, similaire à celle de l'umbo, mais elle changeait rapidement lorsqu'elle était sous pression, affichant déjà une série de pics et de creux prononcés de ± 500 Pa.

La deuxième étude expérimentale a utilisé un balayage de pression continu au lieu des variations de pression transitoires, avec la même durée de cycle globale que dans la première étude. Les comportements de réponse étaient similaires à ceux observés pour les variations transitoires, mais beaucoup plus de détails ont pu être observés. Par exemple, le creux de magnitude a commencé près de R2, puis s'est étendu rapidement à des fréquences inférieures à ce pic. Un creux sur la pars tensa postérieure, qui s'est déplacé d'une manière similaire à R2, est apparu comme un pic sur la pars tensa antérieure.

Un modèle d'éléments finis précédent, qui simulait les réponses et aux sons et aux pressions quasi-statiques importantes, a été développé pour s'adapter à la fois aux variations de pression transitoires et aux balayages de pression. Les résultats de la simulation ont été comparés à nos données et aux données d'autres groupes. Le modèle reproduit certains des comportements observés expérimentalement, mais il existe des divergences.

Collectivement, ces études expérimentales et de modélisation permettront à terme d'extraire davantage d'informations de la tympanométrie et ainsi d'améliorer la prise de décision clinique.

# Table of Contents

# Acknowledgements

I would like to first and foremost thank my family. Throughout a time that had the largest impact on my life, I was lucky enough to build a family of my own during my PhD. My wife Saba and my newborn son Alp taught me how to live for more than one, each day.

If I ever get half the meticulous determination and perfectionism that Dr. W. Robert J. Funnell portrays as an academic, I will have achieved my goals. His ever so available manner, unyielding support, and somehow perfect memory astonishes me. I know that before anything else, his supervision will be what I will miss from my PhD program. As they say “They just don’t build them like this anymore”.

As a perfect pair with Dr. Funnell, Dr. Daniel makes doing everything at once seem easy. Whenever I had a concern or a setback, he managed to make my studies continue and excel. His love for research is only limited by his commitment to his craft.

From a colleague that just graduated, to my co-supervisor, Dr. Hamid Motallebzadeh has been the ideal support throughout my degree. He has managed to show me the ropes, keep in touch when away, and carry me over the finish line when I took a tough turn. His debt cannot be paid easily.

I would like to say thanks to my thesis committee members: Dr. Allen Ehrlicher, Dr. Gary Scavone, and Dr. Brandon Xia. Through their wisdom and patience, they have helped me stay on track and define the scope of my studies. Always constructive and kind, they made me a better academic by improving how I translate my science.

The wonderful members of AudiLab and MOSL, of which I am proud to be a part, also have my debt. I would like to thank Zinan He, who was kind enough to help me with my first experiments; Sahar Choukir and Xuan Wang, who were friends and the first colleagues that I learned the life at McGill with; Sajjad Feizollah and Tina Qian, whose studies laid the basis for my thesis; Majid Soleimani, with whom I had great discussions; Royan Jafari and Marzieh Golabbakhsh, who helped me develop my model, as well as support me throughout the pandemic. Last but the least, Aren Bezdijan has been a great friend and a mentor for me, helping me develop my career and supporting me through the early stages of the experimental study. Our shared memories, I will always be honoured to carry forward with me. I wish them all the best.

I would like to also thank the BBME faculty and staff, especially Dr. Ross Wagner and Pina Sorrini. Dr. Wagner has been there from the beginning, making me remember that first and foremost I am always an engineer. I have asked for his advice on so many occasions that I was worried he would start billing me. Pina Sorrini is a wonderful person who has devoted her time and energy to this program. It was my luck that I got to be a student managed by her. I would like to also thank Trang Q. Tran, for her support and enthusiasm, a face that never fails to make me smile. There are many faculty members that I have had the honour to meet and work with throughout seven years. I would like to thank them for guiding me and spending time with me whenever they could. As BME grew, their hearts have grown also.

I have the privilege of having served in the BBME Student Society for many years, getting to know both the faculty and the students. I have met people of many backgrounds thanks to the inter-disciplinary nature of the program. I would like to thank each and every one of my peers whom I had the pleasure of meeting. This program brought together many brilliant people of diverse backgrounds. I would like to highlight the help and dear friendship of Michelle Y. Tran, Pouria Tirgar Bahnamiri, and Camille Cassel de Camps. Having a close-knit group of friends is already tough to find, but among them you are the diamonds among the rough.

This work was supported in part by the Canadian Institutes of Health Research, the Fonds de recherche en santé du Québec, the Natural Sciences and Engineering Research Council of Canada, the Montréal Children’s Hospital Research Institute and the McGill University Health Centre Research Institute.

# CONTRIBUTIONS OF AUTHORS

**Chapters III and IV:**

**Vibration measurements of the gerbil eardrum under quasi-static pressure steps**, *Journal of the Association for Research in Otolaryngology*, August 2020, Volume 21(Issue 4):287-302.

**Vibration measurements of the gerbil eardrum under quasi-static pressure sweeps**, Submitted to *Journal of the Association for Research in Otolaryngology*, September 2021.

**First author: Orhun Kose**

Involved in designing the experimental protocol and the setup. Performed the experiments (anesthesia, surgery, measurements, etc.). Analyzed and interpreted the results, wrote the manuscripts.

**Second author: W. Robert J. Funnell**

Conceived the study, supervised the research and writing.

**Third author: Sam J. Daniel**

Helped conceive the study, provided the experimental facilities, provided comments and suggestions, reviewed the manuscripts.

**Chapter V:**

**A non-linear finite-element model of the gerbil middle ear under quasi-static pressures**, to be submitted to the *Journal of the Association for Research in Otolaryngology*.

**First author: Orhun Kose**

Revised the previous finite-element model, designed and performed the simulations, analyzed and interpreted the results, wrote the manuscript.

**Second author: W. Robert J. Funnell**

Conceived the study, supervised the development of the model and writing.

**Third author: Hamid Motallebzadeh**

Helped conceive the study, supervised the development of the model, provided comments and suggestions, reviewed the manuscript.

**Fourth author: Sam J. Daniel**

Helped conceive the study, reviewed the manuscripts.

# Chapter 1: Introduction

## 1.1 Motivation

Hearing loss is one of the most common birth defects, affecting at least 1 to 3 per 1000 children in the U.S.A., and can inhibit social and language development (CDC, 2019). Hearing loss can be divided into four categories according to its source: conductive hearing loss (issues in the transmission of the sound from the external ear to the inner ear), sensorineural hearing loss (issues in the transduction of the sound within the inner ear), auditory neuropathy (issues in the transmission of the auditory signal to the brain), and mixed hearing loss. Early distinction between the different types of hearing loss is required to find the appropriate intervention (Spivak and Sokol 2005). Tympanometry is a hearing assessment tool that provides an objective measurement of the status of the outer and middle ear.

Tympanometry measures the impedance or admittance of the ear by measuring the sound pressure in the ear canal in response to an acoustic stimulus of known volume velocity while varying the static pressure in the canal. The admittance is related to the average vibration velocity of the eardrum, and is largest when the middle-ear pressure is equal to the ear-canal pressure. Introducing pressure in the ear canal makes the ear-canal wall, the eardrum and the rest of the middle ear stiffer, reducing the admittance. Any pathology that changes this pathway may be observed in the tympanogram. Since the admittance is heavily dependent on the condition of the eardrum, measuring the vibration response of the eardrum to sound under static pressures can provide critical insight into the mechanics of the middle-ear.

Early clinical tympanometry utilized a single low-frequency probe tone (e.g., 220 Hz or 660 Hz). Later, 800-Hz (Alberti & Jerger, 1974) and 1000-Hz pure tones were found to be more useful in children due to the anatomical differences in their ears (e.g., Kei et al., 2003; Alaerts et al., 2007). Single-frequency tympanometry gives only a limited view of the status of the middle ear. Hence, multi-frequency tympanometry (Colletti, 1975) and later wideband tympanometry (Keefe et al., 1992) were introduced to provide more information and detect features that are visible only in a small frequency range. However, the response of the middle ear under quasi-static pressures is not well understood. Under various conditions, tympanometry can have highly variable sensitivity (Szucs et al., 1995). Even for the lowest pressurization rates, viscoelastic

effects can change the admittance at all frequencies (Shanks & Wilson, 1986). There is a need for a model of the response of the ear to both static pressures and sound pressures to help predict the effects of anatomical variations and pathologies (e.g., Chen & Shen, 1996). Infant ears can have larger variations in the response and are more sensitive to changes in the static pressure profile used in wideband tympanometry (WBT) (e.g., Park, 2017). Hence, establishing a model for tympanometry can help predict the response of the infant ear under various conditions.

## 1.2 Rationale and objectives

There have been many prior measurements of the vibration response of the middle-ear in both humans and other species. Animal models allow for in-vivo measurements that are otherwise impossible. Animal specimens also have less variability and can provide fresher post-mortem measurements. The Mongolian gerbil (*Meriones unguiculatus*) is a relatively inexpensive species that has a large eardrum/body ratio. It has been used before in our lab and by other groups to study the vibration response of the middle ear to sound pressure.

To complement experimental studies, computational models can help investigate features that are observed in the measurements, and predict the effects of various parameters on the vibration response. Finite-element modelling allows for simulating the complex geometric structure and material properties of the middle ear.

The specific objectives of this research are the following:

- To develop a technique for measuring in-vivo vibrations on the gerbil eardrum under quasi-static pressures.
- To study the vibration response of the in-vivo gerbil eardrum under pressure steps (i.e., various levels of constant static pressure).
- To study the vibration response of the in-vivo gerbil eardrum under quasi-static pressure sweeps.
- To investigate the similarities and differences between the vibration responses to a series of pressure steps and to pressure sweeps with a similar cycle length.
- To develop a computational model of the gerbil middle ear that can simulate the response to sounds in the presence of large quasi-static pressures.

- to compare the simulated behaviour with the experimental results and to investigate the various features of the eardrum vibration response during pressurization.

## 1.3 Thesis outline

Chapter 2 describes the anatomy of the ear, differences between human and gerbil ears, and details of laser Doppler vibrometry (LDV) measurements. It continues with the principles of tympanometry, previous measurements on the eardrum and the middle ear, and earlier computational models that simulate the response of the middle ear to sound and quasi-static pressures. Chapters 3 to 5 include the manuscripts of journal articles. Chapter 3 describes in-vivo experimental measurements of the vibration response of the gerbil eardrum under quasi-static pressures using a step-wise pressurization protocol. Chapter 4 describes follow-up measurements on the response of the gerbil eardrum under quasi-static pressure sweeps. Chapter 5 describes a finite-element model that simulates the combination of sound pressures and quasi-static pressures, and compares the simulation results with the previous measurements.

Chapter 6 summarizes the findings from the studies, discusses the significance and limitations of the work, and proposes the next steps in understanding the mechanics of the middle-ear under static pressures.

# Chapter 2: Literature Review

## 2.1 Introduction

This chapter is divided into 4 sections. In Section 2.2, transmission of sound through the ear is described briefly. The components of the gerbil middle ear and its surroundings, with emphasis on the differences between gerbil and human ears, are discussed in detail in Section 2.3. The basic principles of laser Doppler vibrometry and our vibration response measurement system are described in Section 2.4. Section 2.5. includes a description of tympanometry, and related mechanical properties. A review of previous experimental studies in the field of middle-ear mechanics is presented in Section 2.6. Finally, a review of finite-element models of the middle ear is presented in Section 2.7.

## 2.2 Overview of hearing

Mechanical vibrations of an object create sound, which is transmitted through a medium, like the air. These acoustic signals reach the peripheral auditory system, or the ear, where they are converted to the perception of sound in the brain. The peripheral auditory system consists of three parts: the outer ear, the middle ear, and the inner ear (Figure 2.1). The outer ear includes the visible pinna and the external ear canal, and is filled with air. The eardrum, or tympanic membrane, resides at the end of the external ear canal and separates the outer ear from the middle ear, which is also filled with air. The middle ear contains three bones (the malleus, incus, and stapes) that connect the eardrum to the oval window, an opening that separates the middle ear from the inner ear. The inner ear contains the cochlea, filled with liquid, where sound is transduced to nerve signals via hair cells. This pathway from the ear canal to the cochlea corresponds to air-conduction hearing, which is complemented by bone-conduction hearing through the temporal bone directly, as well as by less well-known soft-tissue conduction (e.g., Shimokura et al. 2014).

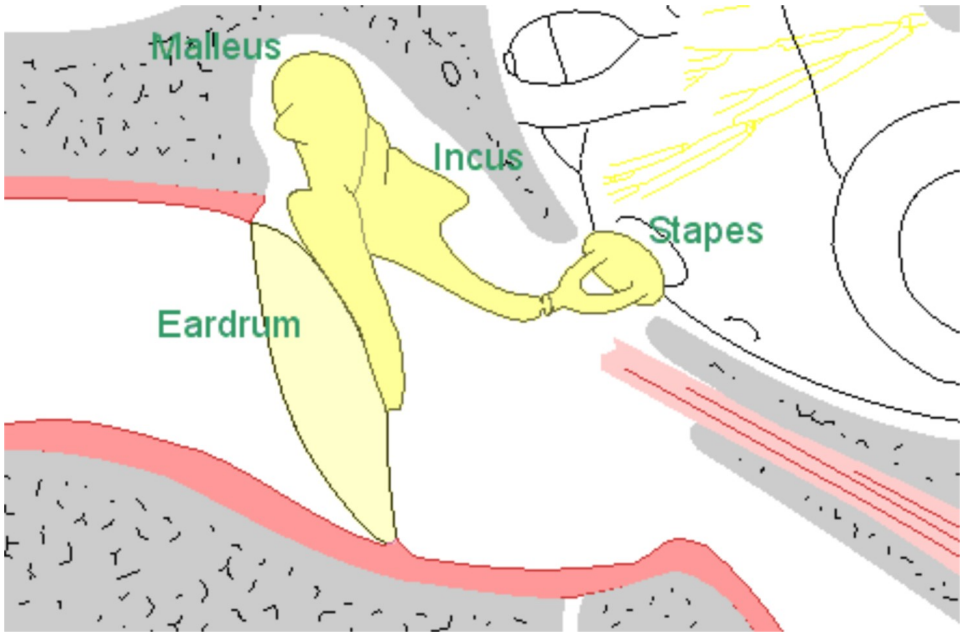


*Figure 2.1: Anatomy of the human middle ear. (After Cull, 1989)*

Further details about the anatomy of the human ear can be read in anatomy textbooks and in atlases of the temporal bone (e.g., Gulya, 2007). The following section focuses on the anatomy of the specific structures in the middle ear that are encountered during the vibration measurements of the gerbil eardrum under static pressures. The last part of the section highlights key differences between gerbil and human ears.

## 2.3 Anatomy of the middle ear

The overall gerbil ear and its orientation with respect to the rest of the skull are displayed in Figure 2.2A. The ear canal is composed of a soft cartilaginous material. The middle ear is covered by a bony shell called the bulla, with the opening at the ear canal called the bony meatus. The eardrum resides slightly medial to the bony meatus, at a steep angle with respect to the opening. The middle-ear cavity (MEC) is an egg-like shape with the ossicles and the cochlea residing in the inferior half. The following sections will describe these parts in more detail.

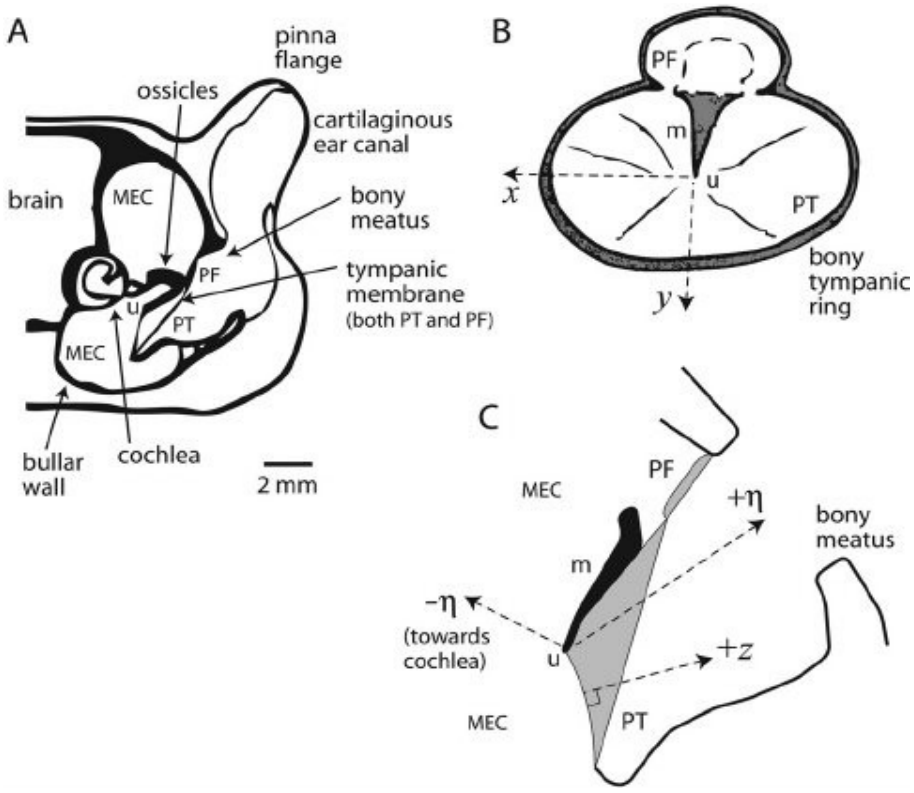


*Figure 2.2: Anatomy of gerbil ear. (A) Cross section of left* ear. *(B) Eardrum. (C) Bony meatus and orientation of eardrum. (After Bergevin & Olson, 2014). (See A1)*

### 2.3.1 Tympanic membrane

The tympanic membrane is a thin fibrous structure, roughly in the shape of a cone. It is composed of two regions (Figure 2.2B): the thick pars flaccida (PF) and larger but thinner pars tensa (PT). At the centre of the PT resides the attachment of the malleus to the eardrum, the manubrium (m in the figure). At the end of the manubrium, and at the apex of the TM, is the umbo (u in the figure). The eardrum joins the ear canal at a thick fibrocartilaginous ring attached to the bony annulus. The shape of the eardrum in Figure 2.2B is roughly the shape seen through the microscope after experimental preparation of the bulla (direction +η in Figure 2.2C), with the PF approximately perpendicular to the viewing direction and the manubrium angled at a roughly 45° angle.

Both PT and PF are composed of three layers: an outer simple squamous epithelium layer that is an extension of the epithelial layer of the ear-canal, a middle fibrous layer called the lamina propria, and an inner mucosal layer (Lim, 1968a, 1968b). The outer layer of the PT has a so-called self-cleaning property that is achieved by migration of cells from the centre to the annulus

(Boedts & Kuijpers, 1978). The fibres in the lamina propria differ between PT and PF. In the PT, there are two thin layers of fibrous collagen-rich connective tissue, with fibres in radial (from the centre to the annulus) and circular directions, while in the PF, there is only loose connective tissue with elastin and collagen fibers. Information about the mammalian tympanic membrane and its properties can be found in Decraemer and Funnell (2008) and Anthwal and Thompson (2016), for example.

### 2.3.2 Ossicles

The middle-ear ossicles, the three smallest bones in the body, are attached to the cavity walls via ligaments and by a bony attachment in the case of the malleus. The largest ossicle, the malleus, is tightly attached to the PT along the manubrium (e.g., de La Rochefoucauld & Olson, 2010). The shape of the manubrium resembles a T-beam with a flat end at the umbo. The manubrium connects to the head of the malleus, medial to the PF. Out of the head of the malleus project the anterior process connected to the bulla by a thin bony attachment (Rosowski et al., 1999) and a shorter lateral process. One of the two muscles in the middle ear, the tensor tympani, is connected to the malleus by a tendon and is buried in the MEC wall.

The malleus head and the incus body form a saddle-shaped synovial joint called the incudomallear joint (IMJ). The incus body extends into a short posterior process and a long process that tapers to a short pedicle before the lenticular process. The incudostapedial joint (ISJ) is the smallest joint in the body and is formed between the lenticular plate and the head of the stapes. The joint consists of layers of articular cartilage with a fluid-filled synovial gap and an enclosing joint capsule (e.g., Funnell et al., 2005; Karmody et al., 2009; Soleimani et al., 2020).

The medial-most and smallest ossicle, the stapes, is composed of a head and a neck that splits into two legs (called crura) posteriorly and anteriorly. These legs converge at the footplate, a thin base at the oval window attached with an annular ligament that allows for the ossicular motion to create vibrations in the liquid-filled cochlea. The stapedius muscle is connected by a tendon to the neck of the stapes. The tensor tympani and stapedius muscles contract in the presence of high-intensity sounds (acoustic reflex) to prevent over-stimulation of the cochlea; and also during head motions, chewing and swallowing, among other situations (e.g., Møller, 1984, chap. 1).

### 2.3.3 Middle-ear cavity

The bulla, which encases the gerbil middle ear and defines the cavity in which the ossicles are suspended, medially becomes integrated into the rest of the skull. The cavity is lined by a mucous membrane (Anthwal & Thompson, 2016). Unlike the case in some other mammals, the middle-ear cavity of the gerbil has only a single chamber, with a smaller cross-section near the ossicles (Rosowski, 2013, pp. 31–65, as cited in Anthwal and Thompson, 2015). The middle ear has an opening to the pharynx through the Eustachian tube. This tube can be closed with a muscle and acts as both a drain and a pressure-equalization device for the MEC.

In addition to the oval window at the stapes footplate, the membrane-covered round window also connects the cochlea to the MEC. Near the round window, buried in the cavity, resides the labryinth, the sensory organ that detects the orientation and acceleration of the head. In the vestibule, the utricle detects linear accelerations while the saccule detects tilts. Semicircular canals, oriented more posteriorly, detect angular acceleration.

### 2.3.4 Manipulation of the surgical area

The surgical area of the gerbil external and middle ear is depicted in Figure 2.3. An incision was made between the jaw and the shoulder, about 3 cm in length (top-centre panel). The bulla was exposed starting posteriorly (top-right panel) and moving clockwise, and then the ear canal was removed down to the bony meatus (mid-left panel). A small hole was created in the bulla to allow access to the middle ear for pressurization (mid-centre panel). The thin membranous lining of the bulla prevents excessive bone chips from falling into the MEC and helps seal the bulla around the ventilation tube. In order to provide a larger access to the eardrum, a small part of the bony meatus (dashed red line in centre-right panel) was cut away. A 3D-printed acoustic coupler (not pictured) was attached to the ear canal with dental cement to provide an enclosed access to the eardrum for the laser vibrometer (HLV-1000, Polytec, Waldbronn, Germany). A glass window (BBA, Edmund Optics Inc., Barrington, NJ), coated to be anti-reflective around the frequency of the measurement laser (620 nm), allowed access for the laser beam to focus on the glass-coated plastic beads on the eardrum. A bead was placed at the umbo, and another one roughly at the middle of the manubrium. One bead was placed on the posterior PT and one on the anterior PT, between the mid-manubrium and the annulus (red circles, bottom panels).

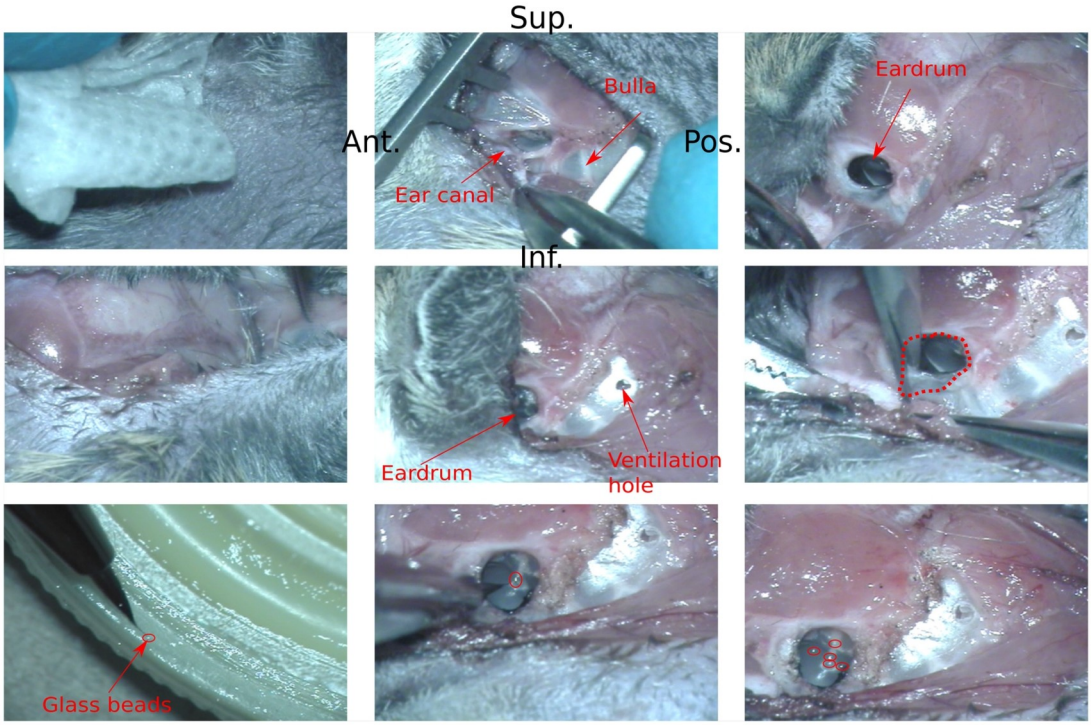


*Figure 2.3: A collage of* photographs *detailing the surgical area*

### 2.3.5 Notable differences between human and gerbil middle ears

There are several key differences between the human middle ear (Figure 2.1) and the gerbil middle ear (Figure 2.2):

1. The gerbil MEC is enclosed in an inflated thin bulla while the human temporal bone is much thicker and is less rounded, with small air cells in the mastoid part.
2. The human MEC air volume ranges from 1.5 to 22 cc in adults (e.g., Stepp & Voss, 2005), including the mastoid, while the gerbil MEC volume is on the order of 0.2 cc (e.g., Ravicz and Rosowski 1997a).
3. The human TM contains more and denser collagen fibres (Chole & Kodama, 1989).
4. The human manubrium is loosely attached to the PT in its middle portion while tightly connected near the umbo and near the lateral process of malleus (Graham et al., 1978; De Greef et al., 2016). The human manubrium is also more rounded in shape.
5. The human anterior mallear process is attached to the MEC by a ligament instead of a bony attachment.

6. The posterior incudal ligament in the human has two bundles instead of a single body (e.g., Winerman et al., 1980).

## 2.4 Laser Doppler vibrometry

### 2.4.1 Principles of laser Doppler vibrometry

Several methods have been used throughout the years to measure both shape and vibration patterns of the eardrum (e.g., Kessel, 1874; Békésy, 1941; Kobrak, 1948). Our lab focuses on one of the interferometry techniques called laser Doppler vibrometry (LDV), and that will be the focus of this section.

LDV is a surface velocity measurement technique that exploits the Doppler effect on the frequency of the laser when it is reflected from a moving surface (e.g., Rossi & Tomasini, 1995). It is a non-invasive and non-contact technique that can measure one or more of the three velocity components of a point on the surface. The Doppler effect is the change in the wavelength of reflected radiation (such as the laser beam) proportional to the velocity of the targeted object.

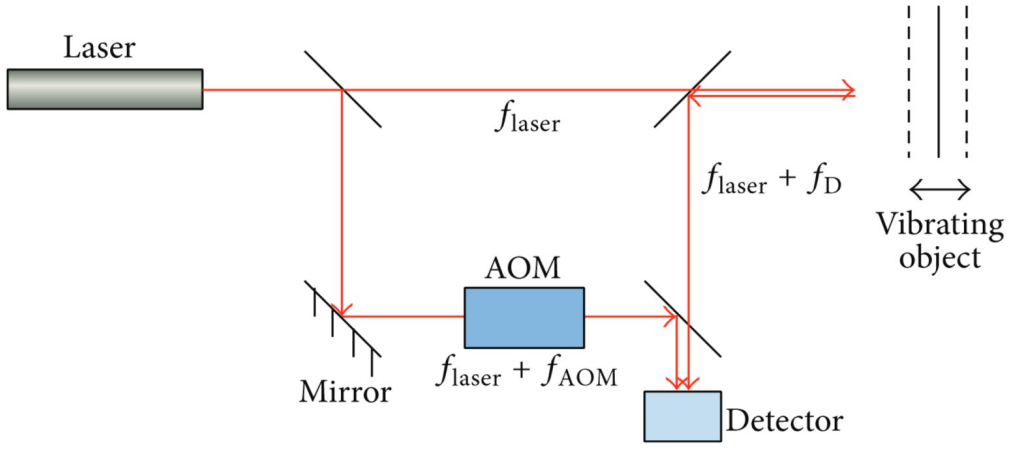


*Figure 2.4: Schematic for a laser Doppler vibrometer (After Fu et al., 2014)*

An LDV system uses this effect by measuring the frequencies of a Doppler-shifted measuring beam and a reference beam. Figure 2.4 shows a diagram for a typical single-point heterodyne LDV system. (A heterodyne measurement system uses the interaction between two signal frequencies). The original laser beam is split into two pathways; the first is directed to the object, and the second is reflected through an acousto-optical modulator (AOM). The vibrating object

reflects the former as a beam with shifted frequency, and both the reflection and the one that goes through AOM are collected at the detector. Using the Doppler effect, the shift in the frequency can be calculated as

$$f_D(t) = \frac{\mathbf{V}(t) \cdot S}{\lambda}$$

where $\mathbf{V}(t)$ is the speed of the vibrating object, $\lambda$ is the wavelength of the laser beam (e.g., 316 nm for a He-Ne laser) and $S$ is a constant (e.g., Yeh & Cummins, 2004).

### 2.4.2 Characteristics of LDV measurements

There are several benefits of using LDV over other velocimetry techniques such as holography (e.g., Khanna & Tonndorf, 1972; Khaleghi et al., 2015) to measure the vibration response of the eardrum. As an LDV sensor head can be mounted on a microscope, it can be easily focused on the small structures in the external and middle ear. LDV can also measure very high-frequency (bandwidth of 80 kHz) vibration responses (e.g., up to 50 kHz for HLV-1000; Polytec 2015) with high frequency resolution.

The reflectivity of the surface is important for obtaining a high signal-to-noise ratio of the LDV measurements. The eardrum is a semi-transparent and thin structure that is angled with respect to the ear canal. Therefore, maintaining a high reflectivity on the eardrum, especially at the PT, requires a reflective bead (or reflective tape or powder). The size of these beads is 40 to 70 microns (A-RET, Polytec, Waldbronn, Germany), while the laser beam spot size in our case is around 50 microns (Polytec 2015) when focused at the optimal range (at 316 mm away from the sensor head). The size of this reflective bead creates a limit to the signal strength if the eardrum displaces in a direction perpendicular to the laser beam as the signal strength falls rapidly when the beam is no longer focused directly on the bead.

The data acquisition method of the LDV system uses an analog-to-digital converter (ADC). The ADC used here is a 24-bit, which gives a very fine resolution for the signal magnitude (e.g., less than 0.2 μm/s for HLV-1000 at full scale magnitude of 20 mm/s converted at 24 bits). Choosing a sampling frequency is an optimization problem between the temporal resolution of the signal and allocation of the computer memory. For a sampling frequency of 128 kHz, the memory of each measurement was reasonable while minimizing the effect of anti-aliasing for the

signal frequency range of interest. The experiments in Chapters 3 and 4 involve sound frequencies up to 10 kHz. This limit is due to assumptions about the uniformity of the sound pressure. Bergevin and Olson (2014) measured the sound distribution in the ear canal and across the gerbil eardrum. They found that the sound pressure in the ear canal was mostly uniform up to 10 kHz. Therefore, the microphone (ER-7C, Etymōtic Research) used in the experiments of this thesis was selected to provide a linear response for frequencies up to 10 kHz. The data acquisition board in the HLV-1000 (NI PCI-4451, National Instruments, Austin, TX, USA) uses sigma-delta ADC converters (Polytec, 2015). These ADCs achieve a low noise and distortion by oversampling.

## 2.5 Principles of tympanometry

Tympanometry is a physiological test (as opposed to a behavioural test) that gives information about the status of the external and middle ear. It measures the acoustic input admittance at the ear canal. Acoustic input admittance is a measure of how much a system displaces (a volume velocity) in response to an input (a sound pressure). In tympanometry, a probe tip is placed in the ear canal (Figure 2.5). The probe applies static pressure to the ear canal and eardrum at the same time as an acoustic signal is introduced by a speaker, and it records the sound pressure level by means of a microphone. The speaker displaces the air with a known volume velocity in the form of a pure tone or a chirp. The microphone measures the resulting sound pressure in the cavity.

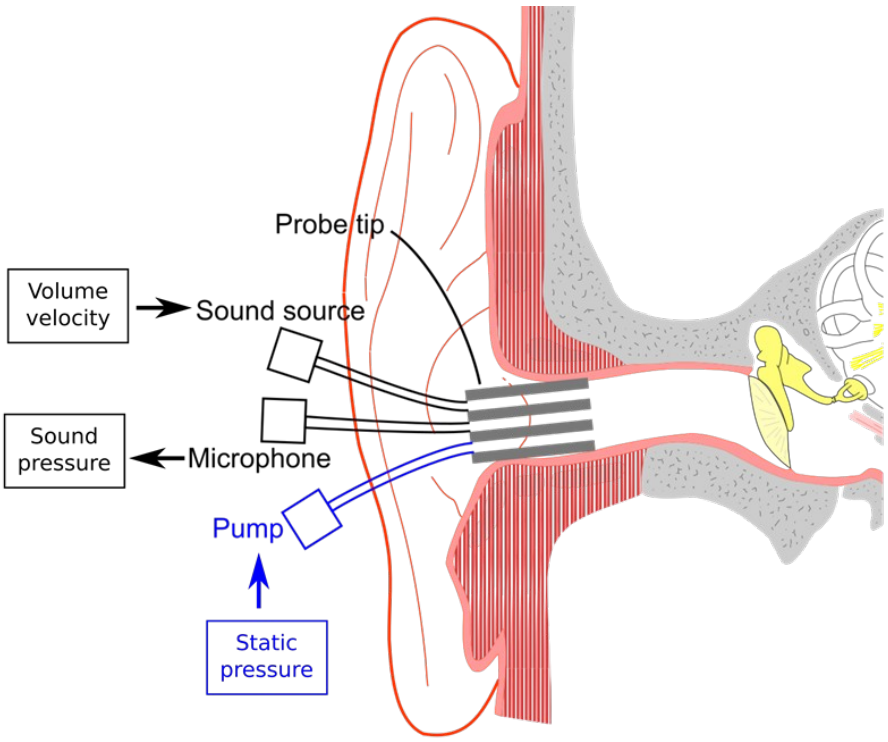


*Figure 2.5: Schematic of* tympanometry

The quasi-static pressures introduced in the ear canal are very small compared with atmospheric pressures, and the sound pressures that are generated in the ear canal by displacing the air via the speaker are many orders of magnitude smaller still. A typical static pressurization cycle consists of a linear continuous ramp that ranges from −4000 Pa to +2000 Pa. Conventional tympanometry uses a 220 or 226 Hz pure-tone signal as the acoustic input. A higher-frequency input of 1000 Hz is often used with newborn and children. In wideband tympanometry, a linear chirp that increases in frequency with time is used as the stimulus (e.g., 226 to 8000 Hz chirp every 0.05 s for an Interacoustics Titan tympanometer). One pressure sweep of a tympanogram lasts on the order of seconds, while the acoustic signals have lengths in the order of milliseconds. Typical pressure and time scales are given in Table 1.

*Table 1: Pressure (top) and time (bottom) scales for signals present in tympanometry*

| Pressure (Pa) | | |
|---|---|---|
| Atmospheric<br>~$1\times10^5$ | Quasi-static<br>up to ~$4\times10^3$ | Sound<br>Up to ~0.5 |
| Typical time (s) | | |
| Pressure sweep length<br>Up to 20 | Total chirp length<br>~0.1 | Pure-tone sound period<br>Down to $10^{-4}$ |

A tympanogram displays the measured acoustical admittance (or its real and imaginary components) over the range of the sweep of the quasi-static pressure. The admittance is calculated by dividing the air volume velocity by the sound pressure level:

$$Y = \frac{U_{acoustic}}{p_{acoustic}}$$

where $U_{acoustic}$ is the air volume velocity generated by the speaker, and $p_{acoustic}$ is the resulting acoustic sound pressure. In clinical tympanometry, the admittance measured at a reasonably high negative middle-ear pressure (e.g., −2000 Pa), where the eardrum becomes very stiff like a wall, is assumed to be only the admittance of the ear canal (Keefe & Levi, 1996). Hence, the typanograms usually compensate for the ear-canal admittance to display only the estimated middle-ear admittance. A normal canal and middle ear would would have a peak acoustical admittance at zero static pressure difference between the ear canal and the middle ear. Admittance and the pressure at which its peak occurs will be changed by, for example, the presence of a built-up middle-ear pressure (Dai et al. 2007).

## 2.6 Previous experimental work

This section reviews past studies that were related to measurements of the middle ear, especially the eardrum. Section 2.6.1 includes the relevant unpressurized vibration studies, followed by the admittance and shape measurements (Sections 2.6.2 and 2.6.3). Finally, Section 2.6.4 includes the pressurized vibration studies. In each section, non-gerbil studies are described before the gerbil ones.

### 2.6.1 Unpressurized vibration measurements

There have been many studies that focused on the vibration pattern of the eardrum. Early ones were summarized by Funnell and Laszlo (1982). Some of the major milestones will be mentioned below. More than 100 years ago, Helmholtz (1868) imagined the role of eardrum as an impedance-matching transformer. He used controlled fluid pressure changes across the eardrum and observed that the mean displacement of the eardrum was at least 3 times more than that of the manubrium. He did not have any tools to observe the vibration pattern itself. Kessel (1874) used a magnifying lens and a stroboscope to observe the vibrations of human cadaver eardrums at 256 and 512 Hz. Much later, Kobrak (1941) used high-speed cinematography to visualize the vibrations of the eardrum, the ossicles and the cochlear windows. He observed a change in the rotation axis of the ossicles at higher intensities. He reported the largest magnitudes at the central region, with the posterior region having larger magnitudes compared to the anterior region. Békésy (1941) used a capacitive probe, again in cadaver eardrums, and concluded that the manubrium did not bend and that, except for near the annulus, the eardrum vibrated as a stiff structure around an axis of rotation.

Tonndorf and Khanna (1968a) used an interferometric method using a laser (LDV, as described in Section 2.4) to measure the vibration at the cat umbo in-vivo. This method provided a large signal to noise ratio, and allowed for measuring very small vibration magnitudes. They observed that the vibration magnitude at the umbo was more or less constant until around 1 kHz. They reported a notch around 2 kHz that at first they attributed to a small hole in the bulla acting as a Helmholtz resonator. However, the notch remained when the hole was plugged with cotton balls. They also reported an anti-resonance followed by a resonance at around 4 kHz. Finally, they reported the phase for these features. The phase reached several cycles at frequencies above 4 kHz. They later made holographic measurements (Tonndorf & Khanna, 1968; Khanna & Tonndorf, 1972) on both human and cat eardrums and reported the vibration patterns. They did not observe a stiff plate-like motion, and reported that until 1.5 kHz the eardrum vibrated in phase. They found that around 3 kHz this pattern was broken up into sub-patterns localized in various regions of the pars tensa. They also concluded that the cat eardrum behaved the same for 1 to 2 hours after death (Khanna & Tonndorf, 1972). Manley et al. used Mössbauer technique on bats (1972) and guinea pigs (1974), a method utilizing a tiny gamma-radiation source on the eardrum where the velocity of the source can be calculated. They reported at three different

frequencies, and found the smallest displacements on the manubrium and the largest on the inferior pars tensa.

Decraemer et al. (1989) measured at multiple points on the cat manubrium and at several locations on the pars tensa for a wide frequency range of 130 Hz to 20 kHz using a similar LDV technique. They also confirmed that up to 1 kHz all points vibrated in phase, but above 5 kHz local resonances emerged. They also observed that, for frequencies above 10 kHz, vibrations of points along the manubrium did not behave like those of a simple rotational element, and did not decrease with increasing frequency as expected. They concluded that multiple points on the manubrium for vibration measurements are necessary to specify the mechanical input to the middle ear, especially at these higher frequencies. Decraemer et al (1997) measured the post-mortem cat eardrum with a better spatial resolution. With the phase data for multiple points on the eardrum, they concluded that the motion of the TM was better represented by a travelling wave. Decraemer and Khanna (2000) recorded 3D vibration measurements of the cat ossicular chain, and observed that for higher frequencies the ossicles in general did not rotate around a fixed axis.

Rosowski (2003) assessed the utility of LDV to provide insight into pathologies and variations in the human ossicles by measuring the in-vivo vibration response at the umbo. He found a significant decrease in magnitude for frequencies below 1 kHz when the ossicular motion was restricted. His group later measured the vibration pattern on multiple post-mortem mammalian species (cat, chinchilla, and human) and live chinchilla using computer-assisted laser holography (Rosowski et al., 2009). This method allowed for vibration measurements with a high spatial resolution and up to 25 kHz. In addition to the ‘in phase’ region for low-frequencies, and more complex vibration patterns with local maxima at mid-level frequencies, Rosowski et al. (2009) reported an ordered pattern of local peaks for higher frequencies (above 8 kHz).

There have been more recent holographic measurements of the vibration pattern of the eardrum. Cheng et al. (2010) used stroboscopic holography on temporal bones, and observed the in-phase vibration pattern at 0.5 and 1 kHz with the largest magnitude in the posterior PT. At 4 kHz and more so at 8 kHz, they observed 4 to 10 ordered local maxima. Rosowski et al. (2011) extended the same setup with vibration (and shape) measurements and interpreted the TM as a thin shell with surface waves. They observed very little in-plane vibration on the TM. They later

expanded their holographic measurement frequency range to 18 kHz (Cheng et al., 2013), and found that the eardrum's motion was a combination of standing and travelling waves, and had slower waves than a simple mechanical delay of a wave from the peripheral to the umbo. They compared their holographic measurements of the TM with measurements on artificial membranes (Khaleghi et al. 2015). Intra-operative LDV measurements of the ossicles were also made recently (Gladiné et al., 2019). They fixed the incus and were able to observe the significant change in the mobility of the incus at lower frequencies.

Akache et al. (2007) measured the vibration response of the post-mortem rat eardrum using single-point LDV in our lab. They used microbeads for multiple points at the manubrium and on the pars tensa to enhance the signal quality and presented displacement magnitudes in the frequency range of 1 to 10 kHz. Contrary to previous studies mentioned here, they observed in-phase vibration magnitude up to 10 kHz. This was attributed to dehydration and consequent stiffening of the middle ear in their post-mortem measurements.

Ellaham et al. (2007) measured the spatial vibration at points on a line perpendicular to the gerbil manubrium up to 10 kHz, similar to the experiments of Akache et al. (2007) in rats. They observed similarity in the vibration magnitude on the pars tensa along a line perpendicular to manubrium, with the lowest magnitude observed at the manubrium. This similarity in the vibration magnitude was explained as the gerbil TM vibrating in a simple pattern until 10 kHz, all in phase. Since the vibration magnitude was more or less constant until 6 kHz in their experiments, this observed pattern was most likely again due to dehydration and stiffening of the TM.

de la Rochefoucauld and Olson (2010) measured the post-mortem vibration response at the gerbil manubrium and on a line perpendicular to it at the umbo, with the bulla and pars flaccida kept open. They saw that the magnitude along the manubrium decreased from the umbo to the lateral process of the malleus. They modelled the motion of the eardrum as a superimposition of a piston-like motion and a slow travelling wave. They also observed a bending motion at the manubrium, even at low frequencies.

Maftoon et al. (2013) measured the in-vivo vibration response on both the pars tensa and pars flaccida with a closed MEC. They observed a common broad resonance around 1.6 to 2 kHz on the pars tensa and on the manubrium. For manubrial points, the vibration magnitudes above this

resonance were similar with an increasing magnitude towards the umbo. For pars-tensa points, there were significant irregularities. When the pars flaccida was flat, the vibration magnitude was significantly higher with a resonance around 800 Hz that coincides with a feature at the umbo. They later reported similar results for an open cavity (Maftoon et al., 2014) where the vibration magnitude at the umbo increased and the broad resonance shifted to between 0.7 and 1 kHz.

### 2.6.2 Admittance measurements

Møller (1963) measured the acoustic input impedance (the inverse of admittance) as well as malleus, incus and round-window vibrations in the ears of anaesthetized cats. He found that the relationship between the impedance at the eardrum and the ratio of sound pressure to malleus velocity was linear for frequencies up to 4 kHz, well above the cutoff frequency of the in-phase eardrum response observed in vibration measurements. He concluded that the impedance of the eardrum up to this frequency was sufficient for understanding the transfer function of the middle ear.

Since static pressures were introduced for tympanometry, changes in pressurized admittance have also been studied extensively. For example, Peterson & Lidén (1970) conducted tympanometry on fresh cadaver ears (up to 48 hours after death). They looked at the tympanograms of several healthy ears and ones with ossicular disarticulation and TM perforations. They observed that for 800-Hz pure tones, the peak admittance could look normal due to superposition of multiple peaks, even for abnormal ears. They still suggested this probe-tone frequency for clinical tympanometry for measuring ME muscle reflexes (Lidén et al., 1970, 1972). They also reported that the peak admittance shifted to a positive ear-canal pressure when the Eustachian tube was closed.

Von Unge et al. (1991) measured the admittance of post-mortem gerbil eardrums under pressure steps (up to ±4, 10 and 20 cm $H_2O$, or about 400, 1000 and 2000 Pa) using a commercial tympanometer. They opened the bulla and removed the incudostapedial joint. Even though they kept the medial side of the eardrum moist throughout the measurements, they attributed the large hysteresis in displacements to the preparation method. This effect was consistent across specimens. They found larger displacements in the posterior PT than in the anterior PT. They compared the tympanograms at 220 and 660 Hz and described the emergence of multiple peaks at the higher frequency. They theorized that TM stiffness changes, but not mass

changes, affected the admittance significantly. They did not observe any significant changes between flat and retracted pars-flaccida conditions.

Rosowski's group, in a series of papers (Ravicz et al. 1992, 1996; Ravicz and Rosowski 1997), reported the input admittance of the gerbil eardrum and ear canal up to 18 kHz. They concluded that the middle-ear cavity volume contributed around 70% of the stiffness of the middle ear and that the larger the middle-ear cavity volume, lower the acoustic stiffness up to 1 kHz. (Zwillenberg (1981) earlier found a similar effect, where filling the MEC with fluid decreased the middle-ear admittance by up to 70%). Teoh et al. (1997) measured the effect of the gerbil pars flaccida on the middle-ear input admittance. They concluded that the pars flaccida acted as a resonator, and observed that, below the low-frequency resonance of the pars flaccida at 500 Hz, the pars flaccida's admittance was mainly acting as a compliance element.

There have been other studies that focused on the effects of tympanometric parameters on measurements in human temporal bones and in-vivo ears, which are described in more detail in Chapter 4. The focus of this section is the overall input admittance measurements.

### 2.6.3 Shape measurements

Early shape studies focused on the shape and displacement of the middle ear in response to everyday quasi-static pressure changes. Kobrak (1948) measured the displacement of the umbo in human cadaver ears optically using a mirror. They varied the pressure between −4 and +6 cm $H_2O$ (roughly −400 to +600 Pa). They observed larger displacements for negative ear-canal pressures than for positive ones. Their displacements were observed to be linearly proportional to the static pressure, probably due to the limited pressure range. They highlighted the need for knowledge about the material properties of the eardrum, the ossicles, and the soft tissue in order to gain insight into the response of the middle ear to sound and static pressure. Khanna and Tonndorf (1975) measured the shape of the cat eardrum using moiré topography for a pressure range of −15 to +30 cm $H_2O$ (roughly −1500 to +3000 Pa) in 5-cm $H_2O$ increments with the Eustachian tube sealed. They reported the differences among the shapes.

Hüttenbrink (1988) performed extensive middle-ear measurements in temporal bones under various conditions such as fixing the incudomallear joint and pulling on the tensor tympani and stapedius muscles. He varied the static pressure up to ±40 cm $H_2O$ (roughly ±4000 Pa). He

observed a complex 3D movement of the stapes during static pressurization of the middle ear, with no complete immobilization even at the highest pressure level. He also saw that the effect of the muscle activation diminished as the static pressure on the eardrum became larger. He concluded that 'gliding' movements in the incudomallear and incudostapedial joints are crucial; and that spontaneous activation of the middle-ear muscles acts to prevent excessive displacement of the ossicular joints. These observations are important for understanding what may contribute to the shape changes of the TM during pressurization.

Dirckx and Decraemer (1991) recorded the shape of the TM in human temporal bones while pressurizing the middle ear (up to ±1500 Pa) using a phase-shift moiré technique and showed how these measurements could be used to evaluate geometric properties of the TM. They observed that the displacement of the malleus could not be modelled as undergoing a simple fixed-axis rotation at higher static pressures. Funnell & Decraemer (1996) incorporated their results into finite-element modelling, and reported on the inter-specimen variability.

Decraemer and Dirckx (1998) later measured the displacement of both pars flaccida and pars tensa simultaneously under a static pressure range of ±2500 Pa in a series of 500-Pa steps. They concluded that for human, the pars flaccida accounted for a very small part of the middle-ear pressure-compensation function of the eardrum. Even the overall eardrum displacements accounted for less than 25%. They concluded that the TM plays only a small role in middle-ear pressure compensation.

Ladak et al. (2004) measured the shape of the cat eardrum under middle-ear pressure steps (up to ±2200 Pa). They observed more symmetry in PT measurements compared to the manubrium. When they immobilized the malleus, the eardrum had more symmetric responses to negative and positive middle-ear pressures, compared to the mobile malleus.

Dirckx et al. (2006) measured the displacement of the post-mortem rabbit umbo and stapes under a pressure sweep up to ±2500 Pa with varying pressurization rates (200 to 1500 Pa/s). They confirmed the previous notion (Lee & Rosowski, 2001) that the umbo displacements are higher at negative middle-ear pressures compared to positive at the same pressure level. Even though the vibration amplitude decreased with increased pressurization rate, it started to plateau for rates higher than around 1000 Pa/sec. They saw a diminishing stapes hysteresis for larger pressurization rates, while the umbo and the malleus hysteresis persisted. From this observation,

they concluded that a complex transfer of motion is present between the ossicles. They also reported a less than 20 microns peak-to-peak amplitude change at the umbo within the 80 minutes of consecutive pressurization cycles.

They maintained the humidity of the dead tissue by a continuous stream of water-saturated vapour from a humidifier; this method was also implemented in future studies in our lab (e.g., Maftoon et al., 2013, 2014). This was not possible for the journal articles that form Chapters 3 and 4 here, because the viewing window of our acoustic coupler was not removable during the experiments.

Von Unge et al. reported gerbil pars-tensa shape measurements (1993) under ear-canal pressure steps. The displacement was quite symmetrical between the negative and positive ear-canal pressures. The dehydration of the eardrum affected the shape and elasticity of the pars tensa significantly. They found two points of maximum displacement at each of the pressure levels, in the posterior and anterior regions respectively.

Dirckx & Decraemer (2001) performed deformation measurements with a step-wise middle-ear pressure protocol (8 steps between 100 Pa and 2000 Pa) for the intact gerbil ear, as well as after removing several structures including the cochlea, stapes, tensor tympani and bony mallear process, and finally after exposing the incudomallear joint. The exposure of the joint increased eardrum displacement, but the other interventions did not have any significant effects.

Larsson et al. (2001) focused on the displacement of the pars flaccida in gerbils, and found that it had a non-linear and asymmetric response to static pressure similar to that of the rest of the eardrum. They reported that the largest displacement was at the centre of the PF, which ballooned drastically at ±100 Pa. The difference between PT and PF displacements was more significant in the positive pressure range.

Gea et al. (2010) measured the static displacements of both gerbil and human eardrums under static pressure steps with X-ray microCT and compared both with their computational model. They found that the annulus of the gerbil PT could be considered as a simply supported boundary, while the border between the PT and PF was more complex and could be pressure dependent. They also observed a bulge near the annulus fibrosis of the gerbil TM.

### 2.6.4 Pressurized vibration measurements

Several studies also introduced pressure steps and sweeps to investigate the vibration of the ossicles and the vibration pattern of the TM under static pressures. Murakami et al. (1997) measured the vibration magnitudes of the umbo and the stapes in temporal bones with a tympanometer probe placed in the Eustachian tube to pressurize the middle ear. They saw that, for both positive and negative middle-ear pressures, the low-frequency vibration magnitudes decreased as the pressure was increased, and the frequency-response peaks shifted to higher frequencies. The displacements at higher frequencies increased as the pressure was increased.

Gan et al. (2006) measured the vibration response of the umbo and the stapes footplate in temporal bones under up to ±2000 Pa and in the presence of middle-ear fluid. The vibration magnitude decreased more up to 1.5 kHz compared to higher frequencies. The middle-ear fluid had drastic effects at the umbo, reducing the vibrations for frequencies above 300 Hz.

Another measurement on temporal bones was conducted by Homma et al. (2010). They measured at the umbo and the ossicles during air conduction, as well as bone conduction (with the use of a shaker), up to ±4000 Pa. They also compared the results with their finite-element model. They observed the largest reduction in vibration velocity for frequencies below 1 kHz, and found that the structural stiffening of the middle ear was the source of this reduction. They also observed that the middle ear had two resonances between 1 and ~~2 kHz with the lower~~frequency one being for air conduction and the higher frequency one being for bone-conduction sound transmission. They also reported that the bone-conduction resonance also shifted to higher frequencies in the presence of static pressures.

Warnholtz et al. (2021) measured the vibration response at the umbo and the stapes for flexible and restricted incudomallear joints in human temporal bones. They observed attenuation of the low-frequency vibration at the umbo with the presence of middle-ear pressure, and the attenuation was bigger when the joint was fixed. They concluded that the flexible joint allows better sound transmission in the presence of static pressures.

Pressurized vibration measurements in the gerbil were first addressed by Lee and Rosowski (Lee & Rosowski, 2001; Rosowski & Lee, 2002) in a series of measurements of the eardrum under static-pressure steps (referred to as a pressure sweep in the articles). They recorded for both free and immobilized pars flaccida, and the difference was mostly insignificant on the pars

tensa. The small effect was only observed for pressures lower than 1 cm $H_2O$ (roughly 100 Pa) and at low frequencies. This pressure range coincides with their observation that the pars flaccida ballooned for small pressures, and did not change for larger pressures. They also observed a lower umbo magnitude in the negative middle-ear pressure half-cycle compared to the positive, with a possible change of mode at large negative middle-ear pressures (roughly around −2000 Pa). They attributed the change of mode to some uncoupling of the umbo from the rest of the pars tensa.

As a follow up to unpressurized vibration experiments in the gerbil (Maftoon et al., 2013, 2014), Shapiro (2014) (also in our lab) measured the vibrations of several points on post-mortem gerbil eardrums under quasi-static steps, similar to those in Dirckx and Decraemer (1991, 2001). They reported the vibration response for a frequency range of 0.5 to 11 kHz, and showed shifting of the peaks as the pressure was increased. They also reported a low-frequency feature that was comparable to the pars flaccida feature observed at the umbo in the previous study (Maftoon et al., 2014). They also reported the hysteresis for consecutive cycles, and found the largest hysteresis in the positive middle-ear-pressure half-cycle. Chapters 3 and 4 below report our follow-up to Shapiro's work.

Salih et al. (2016) measured post-mortem rabbit and gerbil 3D ossicular vibrations under harmonic quasi-static pressures using an X-ray stereoscopy technique. They varied the pressure amplitudes from 500 Pa to 2000 Pa, and measured for frequencies from 0.5 Hz to 50 Hz. They theorized that since ossicle displacements increased with frequency, the middle ear was designed to damp large amplitude low-frequency stimuli. They also recorded a 40% drop between the umbo and the lateral process of the malleus.

## 2.7 Finite-element modelling of the middle ear

Finite-element (FE) modelling is a computational modelling technique that breaks down a system's geometry into discrete connected elements. The motion of each element in response to the input is computed simultaneously, taking into account the material properties, boundary conditions and loads. This method allows for solving problems too complex to be described analytically. The basics of the finite-element modelling technique can be found in textbooks (e.g., Zienkiewicz et al., 2013).

Due to the complexity of the geometry, the differences among the mechanical properties of different biological tissues, and non-linear effects, middle-ear mechanics has been a prominent application for the finite-element method. Finite-element modelling of the middle ear was first introduced by Funnell and Laszlo (1978) for the cat ear. They focused on comparison with the experimental observations of Khanna and Tonndorf (1972, 1975) for frequencies below 1 or 2 kHz where the ear is stiffness-dominated. This linear model included uniform isotropic shell elements for the TM. They identified the parameters that the model was most sensitive to as the TM thickness, its curvature and shape, and anisotropy. They later studied the undamped natural frequencies of the TM with a finer mesh and reported the first six as being from 1.7 kHz to 3.1 kHz (Funnell, 1983).

Funnell et al. (1987) carried out a higher-frequency analysis by implementing Rayleigh damping. They observed a common peak on the manubrium and pars tensa at low frequencies (~2 kHz), and individual peaks for higher frequencies. By increasing the damping, they were able to damp the response at the common peak and make the vibration response smoother. The responses also were smoother on the manubrium than on the pars tensa. The same authors modelled the rigidity of the manubrium (Funnell et al., 1992) and found that a more rigid manubrium increased the vibration magnitude at the umbo at higher frequencies. Their model supported experimental findings of manubrial bending.

Ladak and Funnell (1996) added a stapedial footplate and a cochlear load modelled as discrete springs at the footplate. They saw that for frequencies below 1 kHz the addition of the new elements brought the displacements closer to the experimental data compared to the model of Funnell and Laszlo (1978). In addition to the full middle-ear model, they also modelled middle-ear reconstructions using partial or total ossicular replacement prostheses (PORP or TORP). Funnell (1996) concluded that the curvature of the eardrum may be an important factor in determining how sound pressure drives the manubrium, and that neither tension nor anisotropy is required.

Another area of interest was the lenticular process near the incudostapedial joint. The thin bony pedicle right before the joint was suspected of having an effect on the flexibility of the joint and movement of the ossicles. Funnell et al. (2005) developed a simplified model for the pedicle and the joint, and found that the pedicle could be bending significantly, reminiscent of the

bending of the manubrium. The nature of the joint and the pedicle has been revisited in a more recent model (Soleimani et al., 2020). They developed a ISJ model using histological sections. They modelled the ISJ with a Mooney-Rivlin material and 2-term Prony series, and were able to simulate both tension and compression. They concluded that the model was more sensitive to the geometrical parameters, especially the synovial gap. They suggested further investigation of the material properties of the cartilage layer, and suggested implementation of their model in a full middle-ear model to provide more realistic boundary conditions.

FE models were also developed for human middle ears in many studies. Wada et al. (1992) developed an eardrum model to compare with their own middle-ear analyzer measurements. They studied two boundary conditions between the TM and the annulus: the previously studied "fully clamped" condition, and an elastic boundary. They concluded that the latter fit their experimental data better. They later added more elements to their model (Koike et al., 2002), including the ligaments and tendons, the MEC, and cochlear damping. In addition, they reported vibration modes up to 4 kHz. Their additions allowed the ossicular chain to have a more complex motion, with three different reported rotation axes. The addition of the MEC reduced the vibration response on the TM up to 1.5 kHz, and had insignificant effects for higher frequencies.

Beer et al. (1999) developed a middle-ear model that included the ligaments and muscles. They performed a modal analysis. The TM had its first elastic mode (all in-phase) at 856 Hz. Natural frequencies for the ossicles were around 4 kHz. Hence, they concluded that the ossicles could be modelled as rigid bodies up to 3.5 kHz. Prendergast et al. (1999) developed a model of the outer and middle ear with TM damping, and simulated an implementation of a partial ossicular prosthesis. They found that the prosthesis had the largest effect for frequencies below 1 kHz. They also modelled the stapes footplate tilting and suggested that the rotational movement of the footplate could affect the displacement of cochlear fluid.

Sun et al. (2002) developed a human middle-ear model that was fitted to LDV experimental measurements on temporal bones. They compared five different umbo and stapes measurements with the model, and found that the model predicted vibration magnitudes near the lower end of the experimental range. Their model included the ligaments and muscles, as well as the cochlear damping represented by an array of dashpots, and the annular ligament with an array of springs. They later developed a model with an ear canal and applied the sound pressure in the canal away

from the TM (Gan et al., 2004). They showed that the sound pressure in the ear canal increased closer to the TM, with the exception at the external auditory meatus due to the nozzle geometry. They found that this pattern shows the amplification role of the EAC at higher frequencies. They also included a full MEC with oval and round windows as well as a Eustachian tube opening. They modelled the cochlear damping as 10 dashpots, split on two sides of the footplate with a total impedance of 20 GΩ. Wang et al. (2007) introduced a static pressure in addition to the acoustic pressure to their human model. This model used a five-parameter Mooney-Rivlin material for the TM, ligaments and tendons, which were assumed to be isotropic and homogeneous, and used purely stiffness-proportional Rayleigh damping. They introduced a static pressure range of ±2000 Pa and reported for frequency ranges from 200 to 8000 Hz. They modelled the dynamic response separately from their non-linear static response. Their model results were close to earlier pressurized measurements (Murakami et al., 1997; Gan et al., 2006), but their model had a larger decrease in the low-frequency vibration magnitude due to pressurization. At a middle-ear pressure of +500 Pa, the vibration response at the umbo increased until the first broad peak around 1 kHz.

Qi et al. (2006, 2008) developed the first ear models for newborns that simulated static pressures. They reported TM volume displacement for pressures up to ±3000 Pa. They found that MEC volume and TM stiffness were the two major factors that determined the volume displacement. Their model did not plateau like adult tympanograms, which is a difference also observed in pediatric tympanometry. In a later non-linear model of strips of TM (Motallebzadeh et al., 2013), a 3-term Prony series was used. They were able to simulate both loading and unloading phases of relaxation experiments. Motallebzadeh et al. (2017a, b) further developed the newborn model to simulate linear dynamic responses. They observed similar levels of admittance for the MEC and the ear-canal wall up to 250 Hz, and resonances in the middle ear for higher frequencies.

Ihrle et al. (2013) developed a non-linear human model that included the ear canal and the MEC as elastic bodies in addition to the TM and the ossicles. To reduce the number of degrees of freedom, they used Petrov–Galerkin projection. They reported the response for static pressures up to ±3000 Pa, and observed that the main resonance shifted to higher frequencies when the pressure was changed, more so for the positive ear-canal pressures. They reported an asymmetric static pressure response, which was larger for the negative ear-canal pressures.

More recently, Zhang et al. (2020) simulated the soft tissues in the middle ear and modelled them as both elastic and viscoelastic to investigate their effect. The static displacement was similarly asymmetric, as the positive middle-ear pressure displacements were more than twice the negative ones. Their vibration response showed that the middle-ear pressure reduced mainly the low-frequency (below 1 kHz) magnitude. They concluded that the material properties of the middle-ear soft tissues were especially important in the frequency range between 1 and 3 kHz. In a recent paper, Muyshondt and Dirckx (2021) developed a model that included a complete middle ear that had tympanic membrane annulus, IMJ and ISJ capsules, the latter joint based on the model presented in Soleimani et al. (2020). They modelled the hyperelasticity with a Veronda–Westmann model and viscoelasticity using a Prony series. Their model introduced a significant loss factor in the frequency ranges of $10^{-3}$ to $10^{-1}$ Hz (static pressure) and $10^{1}$ to $10^{3}$ Hz (sound pressure) but not in between. The umbo vibration magnitude showed a significant asymmetry between positive and negative static pressures, especially for frequencies below the first peak (<1 kHz). There was more hysteresis in the negative ear-canal pressure half-cycle. They concluded that viscoelasticity of the IMJ had a significant effect on the transmission of the sound between the umbo and stapes, unlike ISJ.

Gerbil models are relatively newer, mostly adopted after the cat model due to ease of experimentation availability of data. Elkhouri et al. (2006) adapted the previous cat model to gerbil incorporating microCT and histology measurements and introduced a low-frequency 1-Pa sound-pressure input. The model included the ligaments as well as the footplate. Both the anterior mallear ligament and posterior incudal ligament restricted the vibration response of the TM, and specifically increasing the Young's modulus of the anterior mallear ligament decreased the vibration magnitude at the umbo drastically. They also studied the change in the vibration pattern of the TM due to a change in shape, and saw that, even though the pattern changed drastically, the largest magnitude was in the posterior pars tensa for both cases.

Buytaert et al. (2011) combined microCT imaging data with a newer orthogonal-plane fluorescence optical-sectioning technique in order to improve the geometric accuracy for both the bony and soft tissues in the gerbil middle ear. Their geometry also included the MEC as well as the inner-ear cavity. Due to its thickness and geometry, the TM was only visible under μCT, but tendons and muscles in the middle-ear were developed using the newer technique.

A gerbil model was developed in our lab by Maftoon et al. (2015), that includes the ossicular chain and cochlear load. They compared their umbo and pars-flaccida responses with their earlier measurements (Maftoon et al., 2014) and those of Ravicz and Rosowski (1997b). They observed larger low-frequency vibration magnitudes on the posterior pars tensa compared to the anterior pars tensa. The low-frequency response was similar for all nodes on the TM. Above the break-up frequency (1.8 kHz), similar to the one reported in Maftoon et al. (2014)(between 1.0-2.2 kHz), multiple peaks and troughs that differed from node to node in the pars tensa were observed. They replicated their experimental observation that a low-frequency resonance at the umbo is present for a model with a flat pars flaccida, while for a retracted pars flaccida this peak is missing. They also performed an extensive sensitivity analysis for the geometrical and material properties involved in the model. Several conclusions of note include: the shift in umbo resonance and high-frequency smoothing due to increased pars tensa damping; the decreased resonance magnitude at the umbo due to increased cochlear damping; and the decreased overall vibration magnitude on the TM due to an increased Young's modulus of the pars tensa. Their sensitivity analysis highlighted the importance of studying the high-frequency features that were affected even for small changes (±10%) in the parameters.

In order to simulate both large quasi-static pressures and smaller acoustic pressures simultaneously for a nonlinear viscoelastic gerbil model, Choukir (2017) simplified the middle-ear geometry with a large wedge with a fixed rotation axis that replaced the ossicles from Maftoon et al. (2015). She solved the model in both Code_Aster, which was also used in Maftoon et al. (2015), and FEBio (https://febio.org), and compared the results. She applied an acoustic step of 1 Pa and later superimposed a quasi-static pressure sweep with a pressurization rate of 1500 Pa/s, with pressure extremes of ±2500 Pa, the same as the ones used experimentally by Kose et al. (2020). She modelled the hyperelastic behaviour of the TM with a Mooney-Rivlin model for the PT and PF. To simulate the viscoelasticity, she used a six-term Prony series with time constants from 10 μs to 52 s, roughly 2.2 decades apart. All of the Prony coefficients were set to 0.07, except for the coefficient for 220 μs at the PF which was increased to 0.4 to represent the PF damping seen experimentally by Maftoon et al. (2015).

Choukir first studied the effect of the solver time-step size on the vibration response at the umbo and concluded that 10 μs was sufficient to simulate features up to the selected frequency limit of 10 kHz. The results from the unpressurized model were comparable to the experimental

results of Maftoon et al. (2013, 2014) at the umbo and pars tensa. She replicated the experimental vibration response for frequencies up to the main resonance. She attributed her need for a stiffer PT to the constant thickness assumed for the TM, as opposed to the variable thickness used by Maftoon et al. (2015). For the pressurized model, she observed various non-linearities. She observed a ‘kink’ at +150 Pa and +300 Pa in the positive ear-canal pressure half cycles in the loading and unloading phases, respectively. She attributed the ‘kink’ to buckling of the TM. The PT was slightly convex for smaller pressures and slightly concave for larger positive pressures. She did not observe much hysteresis in the umbo displacements for various pressurization rates between 200 and 1500 Pa/s except at the extreme pressures (larger than 2000 Pa in both half-cycles). Significant hysteresis in the vibration response was present for the full pressurization-rate range.

A significant finding in the pressurized sweeps was the shift in the maximum umbo magnitude pressure when the direction of the sweep was reversed. She reported a peak pressure difference of 42.8 Pa between the directions. She attributed this hysteresis to the viscoelasticity (i.e. the Prony series for the TM).

Recently, Qian (2020) developed another model by modifying the wedge geometry of Choukir (2017). She added another wedge block that replaced the malleus and its ligaments, as well as a simplified stapes, incudostapedial joint, and footplate. In addition to 4 discrete dampers representing the cochlear damping, the stapedial annular ligament was represented by 4 discrete springs. Following Soleimani et al. (2020), Qian (2020) used a 3-term Prony series to represent the viscoelasticity of the ISJ.

When compared with the previous models, Qian’s (2020) unpressurized model response at the umbo was comparable up to the first broad peak. However, for frequencie above this peak (above 2 kHz), it was smoother. It was also able to reproduce the low-frequency peak at the umbo due to a flat pars flaccida that was highlighted in Maftoon et al. (2015). The three model responses (Maftoon et al., 2015; Choukir, 2017; Qian, 2020) had small differences between the resonance frequencies at the pars tensa compared to the experimental results, as the closely-spaced pars tensa peaks are not easy to accurately simulate. For pressurized displacements, the vibration results from Qian’s model were comparable to the displacements reported in Dirckx and Decraemer (2001) in the positive ear-canal-pressure half-cycle, but much larger in the negative

ear-canal-pressure half-cycle. Similar to what Choukir (2017) found, Qian computed almost constant hysteresis for all the pressurization rates. She also reported a similar PPD value, 36.3 Pa compared to 42.8 Pa, between positive and negative sweep directions.

Qian also compared the vibration response at the umbo under step-wise pressurization like what was used by Kose et al. (2020). Her model had a larger unpressurized low-frequency vibration magnitude compared to the experimental results and a resonance at a similar frequency but much sharper and with a higher peak magnitude. For each pressure level, she used a single pressure step followed by a chirp in order to compare with the experimental response. When the ear-canal pressure was increased, she did not observe R1 (the low-frequency peak seen in the experiments) around 2 kHz, but did observe R2 (the largest peak seen in the experiments) around 3.5 kHz shift to higher frequencies, albeit at higher magnitudes. Her low-frequency magnitude plateaued at around +1500 Pa, and stayed constant for higher pressures.

# Chapter 3: Vibration measurements of the gerbil eardrum under quasi-static pressure steps

Published in the *Journal of the Association for Research in Otolaryngology,*

2020 Aug; Volume 21(Issue 4): 287-302. doi: 10.1007/s10162-020-00763-2. E-published on 2020, Aug 11.

This chapter introduces the experimental setup for in-vivo gerbil eardrum measurements under quasi-static measurements. This is a continuation of the post-mortem step-wise pressurization protocol measurements that were conducted by Shapiro (2014). The animal model, the pressurization system and the measurement system are described. The use of the step-wise pressurization protocol provided stable measurements that could be used as a stepping stone to pressure sweeps (or ramps) that are used in clinical tympanometry. With this setup and the pressurization protocol, we were able to make measurements at multiple regions: the pars flaccida, the anterior and posterior pars tensa, and the manubrium including the umbo. In order to verify the repeatability of the measurements, many consecutive cycles were recorded. The behaviour of the peaks was discussed.

**ABSTRACT:** Tympanometry is a relatively simple non-invasive test of the status of the middle ear. An important step toward understanding the mechanics of the middle ear during tympanometry is to make vibration measurements on the eardrum under tympanometric pressures. In this study, we measured in-vivo vibration responses in 11 gerbils while varying the middle-ear pressure quasi-statically, with the ear canal at ambient pressure. Vibrations were recorded using a single-point laser Doppler vibrometer with five glass-coated reflective beads (diameter ~40 μm) as targets. The locations were the umbo, mid-manubrium, posterior pars tensa, anterior pars tensa, and pars flaccida.

As described in earlier studies, the unpressurized vibration magnitude was flat at low frequencies, increased until a resonance frequency at around 1.8–2.5 kHz, and became complex at higher frequencies. At both the umbo and mid-manubrium points, when the static pressure was decreased to the most negative middle-ear pressure (−2500 Pa), the low-frequency vibration magnitude (measured at 1.0 kHz) showed a monotonic decrease, except for an unexpected dip at around −500 to −1000 Pa. This dip was not present for the pars-tensa and pars-flaccida points. The resonance frequency shifted to higher frequencies, to around 7–8 kHz at −2500 Pa. For positive middle-ear pressures, the low-frequency vibration magnitude decreased monotonically, with no dip, and the resonance frequency shifted to around 5–6 kHz at +2500 Pa. There was more inter-specimen variability on the positive-pressure side than on the negative-pressure side. The low-frequency vibration magnitudes on the negative-pressure side were higher for the pars-tensa points than for the umbo and mid-manubrium points, while the magnitudes were similar at all four locations on the positive-pressure side. Most gerbils showed repeatability within less than 10 dB for consecutive cycles.

The results of this study provide insight into the mechanics of the gerbil middle ear under tympanometric pressures.

## 3.1 Introduction

Tympanometry is a clinical test that gives information about the status of the middle ear, to detect conditions like the presence of middle-ear fluid, inflammation, infection and cholesteatoma (e.g., Kei et al. 2003). In tympanometry, a probe tip is placed in the ear canal to introduce a range of quasi-static pressures at the same time as a speaker generates an acoustical signal, which is recorded by a microphone. The speaker may introduce a pure-tone signal (e.g., 226 Hz is common for adult tympanometry), or a chirp (a short signal whose frequency changes with time). A tympanogram displays the measured acoustical input admittance as a function of the quasi-static pressure. The input admittance is sometimes hard to interpret in adults, and even more so for infants. Tympanometry is highly dependent on the behaviour of the eardrum, and studying the response of the eardrum with respect to simultaneous large quasi-static pressures and sound pressures can provide insight into the mechanics of the middle ear during tympanometry. Figure 3.1 shows a typical tympanogram; the input admittance measured at the entrance to the ear canal is displayed as a function of the static pressure for a single pressure sweep. The largest admittance occurs around 0 Pa.

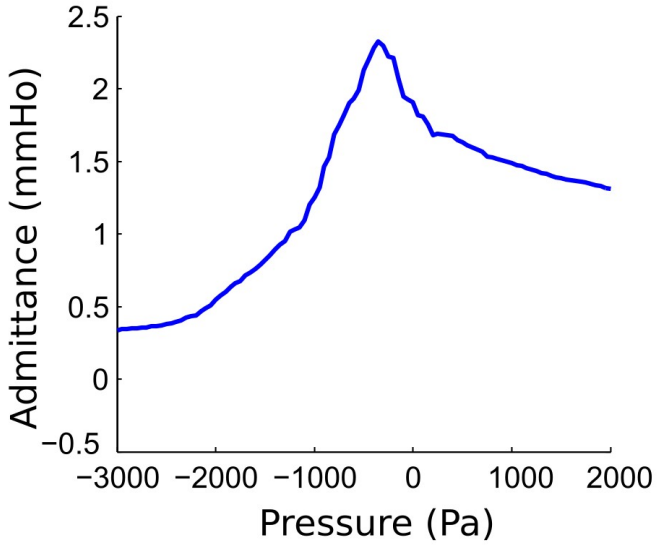


*Figure 3.1: A typical tympanogram of a newborn at 1 kHz.*

As an intermediate step toward understanding the human middle ear, the use of animal models is widely accepted: they provide better-quality data and allow experiments that are not possible in humans. We use Mongolian gerbils for several reasons. There are abundant data available for

both shape and vibration measurements of the gerbil eardrum and ossicles (e.g., Decraemer et al. 1997; Decraemer and Khanna 2000; Akache et al. 2007; Maftoon et al. 2013), which can be used to compare results and validate numerical models. The gerbil eardrum is large relative to the body size, which increases its accessibility. Gerbils have a hearing range that covers most of the human range and more, from about 200 Hz to 50 kHz (Engel 2008). Finally, when compared to chinchillas or larger animals, gerbils are inexpensive for both purchase and maintenance.

Several studies have involved LDV measurements at multiple points on the gerbil eardrum. For example, Ellaham et al. (2007) measured post mortem at a few points on the pars tensa around the umbo, while de La Rochefoucauld & Olson (2010) performed both post-mortem and in-vivo vibration measurements at numerous points along the manubrium and on the pars tensa. More recently, Maftoon et al. (2013; 2014) measured in-vivo vibration responses along the manubrium and on the pars tensa in a line perpendicular to the manubrium close to its mid-point, as well as on the pars flaccida. Above a stiffness-dominated low-frequency region where all points were in phase, they observed a “breakup frequency” that ranged from 1.8 kHz to 2.8 kHz, beyond which many closely packed peaks were observed and the frequency response varied greatly among points, especially on the pars tensa.

In order to better understand the effects of tympanometry-like quasi-static pressures in the gerbil, several studies have introduced quasi-static pressures during measurements of eardrum shape (e.g., von Unge et al. 1993; Dirckx and Decraemer 2001; Gea et al. 2010) and admittance (von Unge et al. 1991), with the pressurization applied in the ear canal; and of umbo and pars-flaccida vibration (Lee and Rosowski 2001), with the pressurization in the middle ear. In a recent LDV study from our lab, Shapiro (2014) measured the vibrations at two locations on each of a small number of post-mortem gerbil eardrums with quasi-static pressures in the middle ear.

In this study we present in-vivo gerbil eardrum vibration measurements under static pressures using the step-wise pressure protocol used in (Dirckx and Decraemer 2001), but with the pressures applied in the middle-ear cavity as done by (Shapiro 2014). The measurements were made at two points on the manubrium, two on the pars tensa and one on the pars flaccida. The results are given for each point as frequency responses for different pressures and also as functions of pressure for a specific frequency. Differences between consecutive cycles and over the course of the experiment are shown.

## 3.2 Materials & Methods

### 3.2.1 Gerbil preparation

This study received ethics approval from the Institutional Review Board of the McGill University Health Centre Research Institute. The experiments were performed on male Mongolian gerbils (Meriones unguiculatus) provided by Charles River Laboratories (St-Constant, QC) with body weights ranging from 50 to 100 g. Of our 15 most recent gerbils, results are reported for the 11 which survived until the end of the experiment and for which there were no problems with pressurization. Carprofen and buprenorphine (20 and 0.05 mg/kg, respectively) were administered subcutaneously 30 minutes prior to the surgery. Pentobarbital and xylazine (35–50 and 10 mg/kg, respectively) were prepared according to the age of the animal (35 mg/kg if the animal was less than 6 months old and 50 mg/kg if 6 months old or older) and administered intraperitoneally.

The health and induction level of the gerbil were monitored using a portable monitoring device (PhysioSuite, Kent Scientific, Torrington, CT), measuring its heart rate and blood $O_2$ saturation level with a paw sensor. Induction level was also checked by the toe-pinch reflex approximately every 5 minutes. A maintenance dose of pentobarbital and xylazine (5–10 and 10 mg/kg, respectively) was given every 30 minutes or whenever needed; the xylazine dose was injected once after two pentobarbital doses. The animal was euthanized with a 3-times anaesthesia overdose when the measurements had been completed, or if the toe reflex was recovered and the anaesthetic level could not be restored.

An incision was made between the left shoulder and the jaw, followed by careful removal of the skin and soft tissue to expose the posterior inferior part of the bulla. The complete exposure of the region was performed methodically, in the order posteriorly, superiorly, anteriorly and finally inferiorly around the ear canal. Finally, the ear canal was removed down to the bony meatus, exposing the eardrum. Care was taken to avoid cutting nearby blood vessels and, in the case of superior facial artery branches where avoidance was not possible, they were cauterized immediately.

To expose the inferior region of the eardrum (providing a complete view of the manubrium and the cone of light), part of the bony meatus was drilled away. A 1-mm hole was also created

on the superior-posterior surface of the bulla at least 20 mm away from the bony meatus to access the middle ear with the pressurization system. Care was taken to prevent any physical damage to the bulla and any debris on the eardrum.

### 3.2.2 Laser Doppler vibrometry

Immediately after exposing the eardrum and drilling the middle-ear pressurization hole, glass-coated plastic beads with an average diameter of 40 µm (A-RET, Polytec, Waldbronn, Germany) were carefully placed in five different regions of the eardrum using a micro brush (XS Artificer Layer, Games Workshop, Memphis, TN). These beads improve the reflection of the beam of the laser Doppler vibrometer (LDV). As seen in Figure 3.2, one bead (indicated by a blue filled circle in the figure) was placed at the umbo and another one (red) at the centre of the pars flaccida. Then, another bead (also blue in the figure) was placed between these, on the manubrium (referred to below as mid-manubrium). Two more beads (green) were placed on the pars tensa, anterior and posterior to the manubrium, at the level of the mid-manubrium bead. Shaded areas in the figure show the estimated range of placement of each bead across specimens. Due to the variability in gerbil anatomy and in the fixation of the acoustic coupler, there were variations in the angle of incidence of the laser beam. These variations are assumed to be

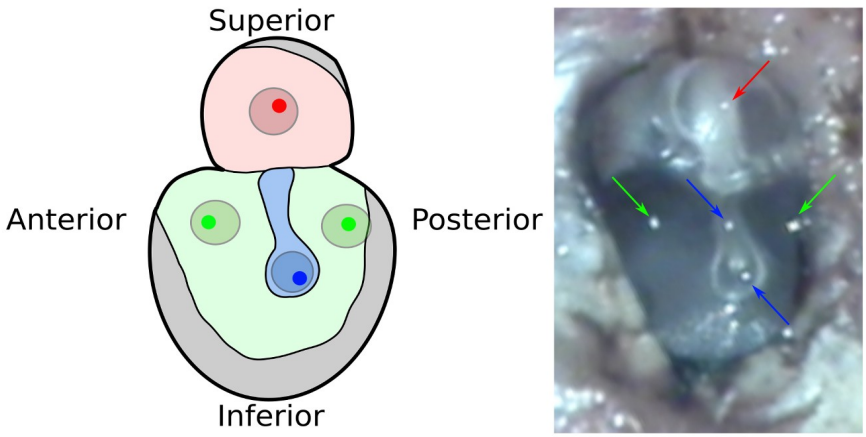


*Figure 3.2: Diagram (left) and photograph (right) of bead placement (blue=manubrium, green=pars tensa, red=pars flaccida; shaded areas represent ranges of bead placement; grey areas represent overhang of the bulla).*

negligible. All measurements within a given animal were recorded without repositioning of the coupler.

The overall experimental setup is shown in Figure 3.3. A 3D-printed acoustic coupler made of a polymer resin (VeroYellow, Stratasys, Valencia, CA) was fixed on the bony meatus using dental cement (Intermediate Restorative Material, Dentsply, York, PA; yellow area in figure). The same dental cement was also used to fix the pressurization tube to the hole in the bulla.

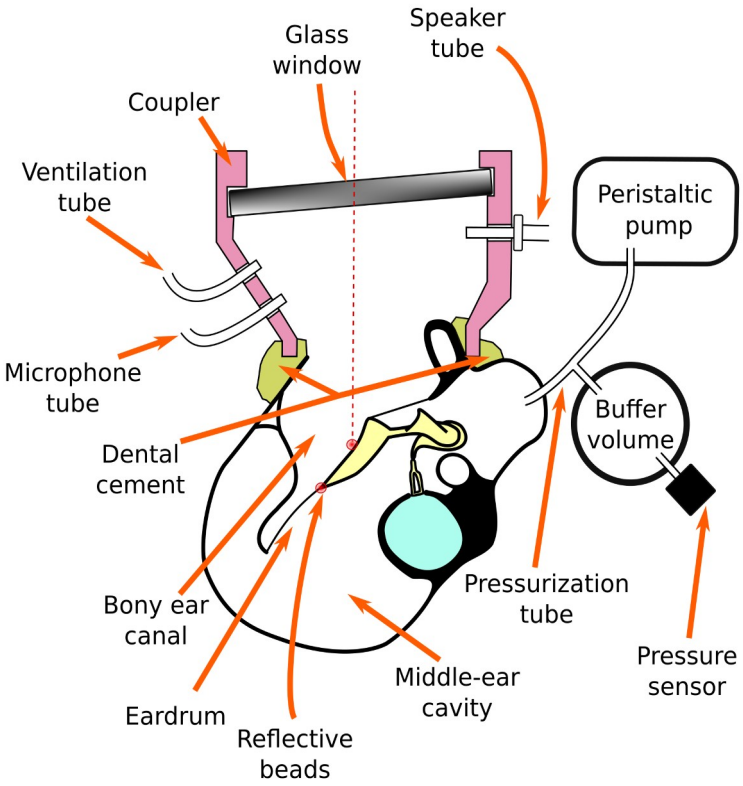


*Figure 3.3:* Experimental setup, with a plastic coupler fixed to the gerbil bony meatus. The static pressure was applied to the middle-ear cavity.

The acoustic coupler supported the microphone probe tube, the speaker tube and the ventilation tube. The speaker (ER-2, Etymōtic Research, Elk Grove Village, IL) introduced sound into the ear canal via the acoustic coupler, and the resulting sound pressure level was recorded by the microphone (ER-7C, Etymōtic Research). A 10-cm-long ventilation tube was used to prevent pressure and moisture build up in the ear canal. A single-point LDV (HLV-1000, Polytec, Waldbronn, Germany) was attached to the operating microscope (OPMI-1 H, Zeiss, Oberkochen, Germany), its laser targeting the beads on the eardrum through a 15-mm-diameter float-glass optical window (Edmund Optics Inc, Barrington, NJ), which had a BBAR anti-reflection coating for the specific wavelength of the laser and was placed at a 5° angle on the top

of the coupler to further reduce reflections. The acoustical stimulus was a linear frequency sweep from 0.5 to 10 kHz in 128 ms with no pause between sweeps. The speaker voltage was kept constant. The sound pressure recorded by the microphone was at least 60 dB SPL at 0.5 kHz and stayed within 5 dB for the frequency range of 0.5 to 10 kHz. The reflected laser signal strength measured at the sensor head was at least 70% for all measurements.

The pressurization system consists of a peristaltic pump controlled by a microcontroller (Arduino Uno, SmartProjects, Strambino, Italy); a pressure sensor (20 INCH-D-4V, Allsensors, Morgan Hill, CA); and the tube that provides access to the middle ear. The speed of the pump motor was kept constant at its maximum. The resulting pressurization rate (4400 Pa/sec) was determined by the combined volume (about 0.2 mL) of the gerbil middle-ear cavity and the tubes and connections of the pressurization system. In contrast to clinical tympanometric practice, the static pressure was applied in the middle-ear cavity and not in the ear canal.

The LDV velocity measurements were recorded using the VibSoft software (Polytec). Ten consecutive chirps at a time were averaged in the time domain, then converted to the frequency domain using a Fast Fourier Transform. The normalized vibration velocity was then converted to displacement and both magnitude and phase were saved using a custom macro which automatically stored the data using a standardized file-naming system and synchronized the timestamps between the vibration and pressure measurements. The pressurization system was controlled by a Python script that transferred pressure-step commands from the computer to the microcontroller. The pressurization protocol was similar to the one used by Dirckx and Decraemer (2001), with the static pressure varying over a range of ±2500 Pa in 500-Pa increments. They actually applied their pressures in the ear canal, but reported them as equivalent middle-ear pressures. The pressure values here are reported in terms of the actual middle-ear pressure. The pressure was held for 10 seconds at each step, corresponding to about 7 or 8 chirp averages. Only chirp averages with a laser strength of more than 50% were considered (usually 4 or 5 chirp averages per step) to ensure a good signal-to-noise ratio. A full pressurization cycle consisted of decreasing from 0 Pa to −2500 Pa, increasing back to 0 Pa, increasing to +2500 Pa, and decreasing back to 0 Pa. The tolerance of the pressurization system was chosen to minimize the transient between pressure steps without introducing oscillations during the step. Hence, there was variability of up to ±100 Pa in the static pressure at each pressure level. The pressure sensor was accurate to within 12 Pa.

### 3.2.3 Measurements

At the beginning of each experiment, at least three consecutive pressurization cycles at the bead on the umbo were recorded. After three or more cycles at each of one or more of the other beads had been recorded, one or more final cycles were recorded at the umbo before sacrifice. (Sometimes pressurization cycles were also measured after sacrifice, but they are not reported here). The laser was manually aimed at the target bead at the beginning of each cycle, and re-aimed after each pressure step when needed. The time required for the manual re-aiming sometimes resulted in losing the measurement for the first one or more chirp averages for the new pressure value. Figure 2.4 shows an example of the middle-ear pressure (black line) and the resulting umbo vibration magnitude measurements (red line) at a single frequency (1.0 kHz) as a function of time throughout one pressurization cycle. The pressure signal shows irregularities at the beginnings of some of the pressure steps (e.g., the upward spike in the −500-to-−1000-Pa transition at t≈20 s and the brief reversal in the −2500-to-−2000 Pa transition at t≈60 s) and in the middles of some pressure steps (e.g., the spike in the 0-Pa step at t≈4 s). These irregularities may be due to the control system for the pump; they are assumed to have negligible effects on the response of the middle ear because they are rather small and very brief. At each step, one chirp average is selected (green square markers). The selection was performed based on visual examination of complete frequency responses, not just a single frequency as shown in the figure, and using the following criteria in order of decreasing priority: having a stable frequency response that does not show noise artifacts; having one or more other chirp averages in the same pressure step with overall magnitude within 2 dB of the selected chirp; and not being in the first two seconds of the pressure step. Due to the difficulty of the manual tracking, some of the steps did not have a chirp average that met all of the criteria (e.g., at the −500-Pa step at t≈20 s, all consecutive chirp averages differed by more than 2 dB). For such a step, the chirp average that satisfied the first criterion was selected, and confirmed by comparing the magnitude at the corresponding pressure steps of the other pressurization cycles for that bead. Especially near ambient pressure, the bead displacements were large in response to the quasi-static pressure change, which often caused the bead to move outside the ~35-μm spot size of the laser beam.

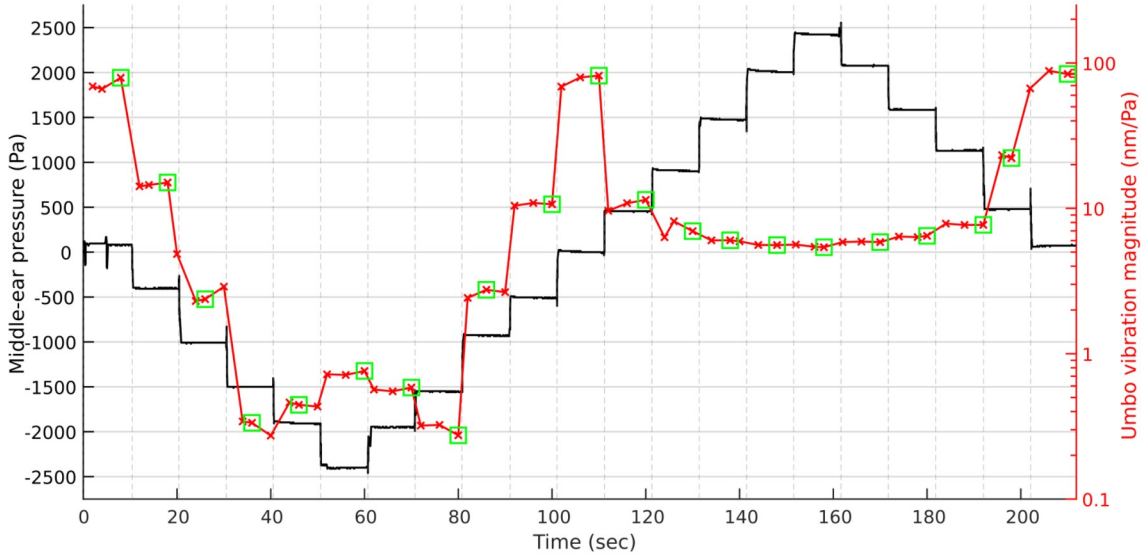


*Figure 3.4: Middle-ear pressure (black) and corresponding vibration response (red) at 1.0 kHz for gerbil G31 at the umbo, for a single cycle. Green squares mark the measurements that were manually selected for each pressure step.*

### 3.2.4 Noise floor

All measurements were recorded in a sound-isolation chamber where the animal and the microscope were placed on an anti-vibration pad on a table. Nevertheless, building vibrations and the vibration of the motor of the pump were sometimes recorded by the LDV. Figure 3.5 shows the vibration levels measured at a point on the inside of the acoustic coupler for several animals, compared with the lowest vibration magnitude response measured in G31 (at mid-manubrium, −1500 Pa). The noise floor in the figure stays below 0.1 nm/Pa up to 10 kHz, apart from a noise peak at 0.55 kHz for one measurement. For the range of frequencies considered here, the measured magnitudes were at least an order of magnitude larger than the noise floor.

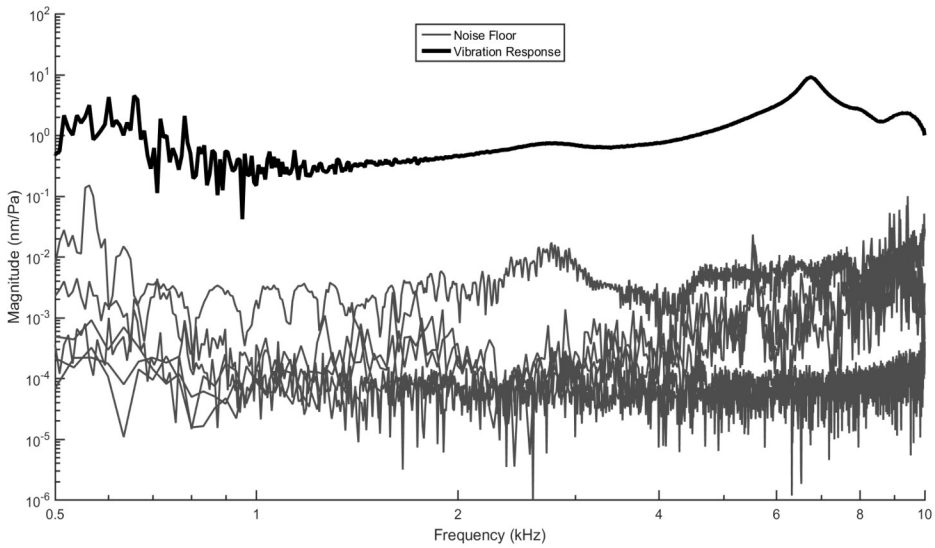


*Figure 3.5: Noise floors of the vibration response (thin grey lines) for several gerbils as measured on the inside of the acoustic coupler. The vibration response with the lowest overall magnitude (G31, mid-manubrium, at −1500 Pa) is provided for comparison (thick black line).*

## 3.3 Results

### 3.3.1 Interspecimen variability

Figure 3.6 shows the unpressurized vibration responses at the umbo for all 11 gerbils. The range of the closed-bulla in-vivo results in Figure 4 of Maftoon et al. (2013) is indicated by the shaded area. The low-frequency (from 0.5 to 1.8 kHz) magnitudes for our gerbils, with the exception of G35, were 27 to 66 nm/Pa at 1 kHz, lower than those of Maftoon et al. (63 to 115 nm/Pa). The low-frequency phases for our gerbils were −7° to −20° at 1 kHz, closer to zero than those of Maftoon et al. (−14° to −35°). The peak caused by the pars flaccida in some of the gerbils of Maftoon et al. was not present in any of our gerbils, possibly due to differences in the experimental setup and the presence of the pressurization system. The range of middle-ear resonance frequencies reported by Maftoon et al. was 1.5 to 2.0 kHz, narrower than our range of 1.3 to 2.6 kHz. (The peaks and troughs in the frequency responses represent maxima and minima of damped combinations of the natural modes of the spatially distributed system, as reflected at the particular location being measured. Such peaks are often loosely referred to as resonance peaks). The phases at this resonance were close to −90° for all gerbils. For frequencies above 2.5 kHz, the vibration magnitudes and the frequencies of the peaks, as well as the phase values,

vary more among ears than at lower frequencies. This variability is smaller than the differences caused by changing the static pressure to ±500 Pa. In the following sections, individual responses are shown for animal G31 (shown with thick lines in Figure 3.6), since it was the only animal for which measurements were recorded for all four regions, and its responses were fairly representative.

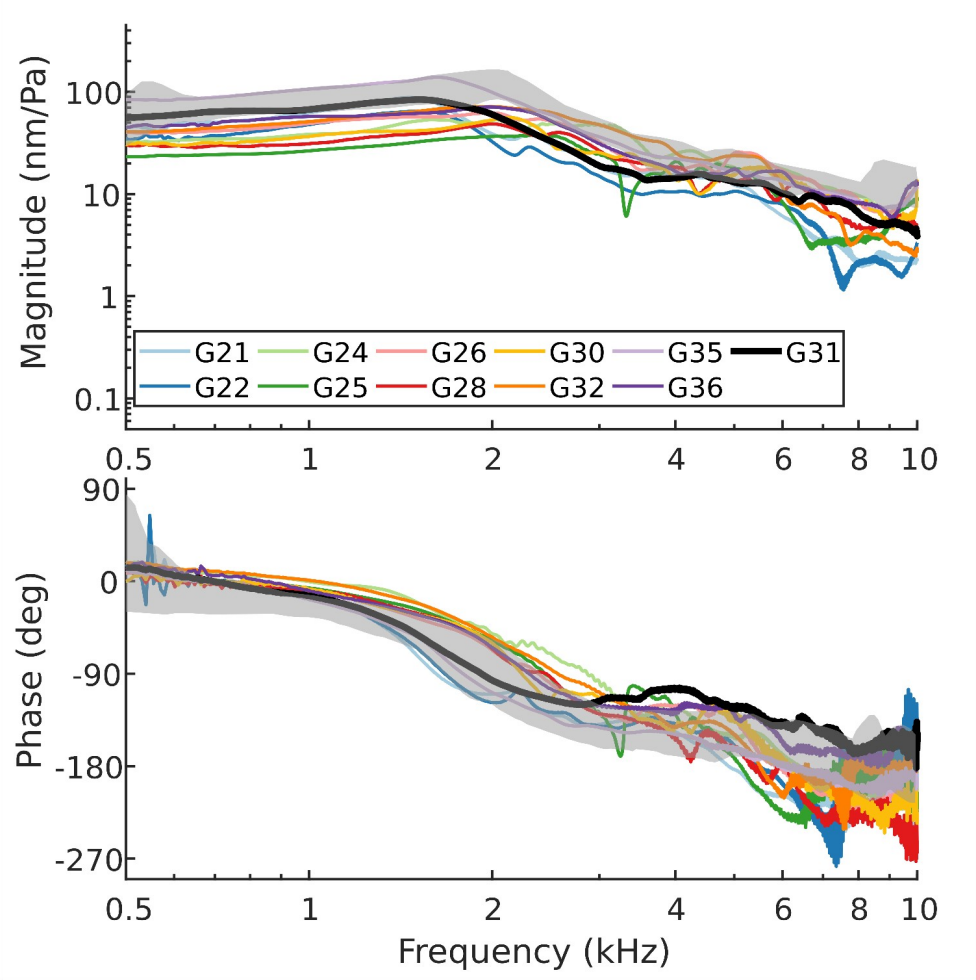


*Figure 3.6: Unpressurized vibration magnitudes (top) and phases (bottom) at the umbo for all 11 gerbils. Grey areas are the vibration magnitude and phase ranges for the 12 gerbils reported in Maftoon et al. (2013).*

### 3.3.2 Temporal variability

Here we present the temporal variability of the vibration magnitude and phase throughout the experiment for animal G31. Figure 3.7 shows the four consecutive cycles at the beginning of the experiment (solid lines), as well as four cycles roughly two hours later (dashed lines). After the

very first pressurization cycle (solid black line), the low-frequency vibration magnitude (measured at 1 kHz) decreased by as much as 9 dB at the second cycle (solid red line), and then stayed within 3 dB for the third (solid green line) and fourth (solid blue line) cycles. The decrease was smaller at frequencies higher than 4 kHz. Due to similar small changes after the first cycle for all ears, in Figure 3.6 the second pressurization cycle was displayed for each umbo measurement.

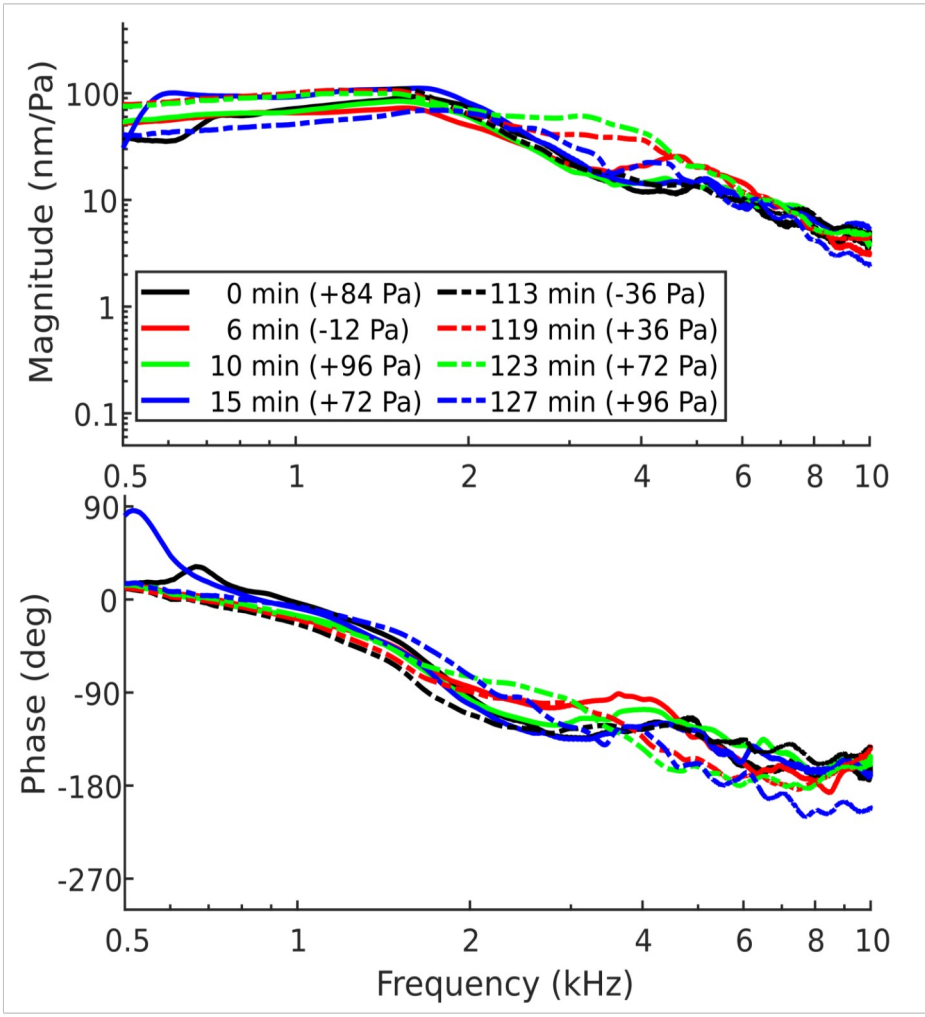


*Figure 3.7: Nominally unpressurized in-vivo vibration magnitudes (top) and phases (bottom) at the umbo for four consecutive cycles at the beginning of the experiment (solid lines) and near the end of the experiment (dashed lines), for gerbil G31. The time of each measurement (in minutes after the first measurement) is given in the legend. (Actual middle-ear pressure values are given in parentheses.)*

Just before sacrifice, after about 2 hours of measurements on other beads, the low-frequency vibration magnitude at the umbo had increased back to its original value for the first three cycles (black, red and green dashed lines, respectively). The low-frequency vibration magnitude decreased by 14 dB for the last cycle (blue dashed line). The variability for consecutive cycles is inconsistent, which may be partly due to the variability in the actual static pressures (±100 Pa) of nominally unpressurized measurements. This variability was present in most ears, but was again smaller than the differences caused by changing the static pressure to ±500 Pa.

### 3.3.3 Manubrium response

This section presents vibration responses at the two manubrium points (umbo and mid-manubrium) for gerbil G31. Figure 3.8 shows the negative-pressure (left panel) and positive-pressure (right panel) half-cycles of the second pressurization cycle at the umbo. For the first measurement at 0 Pa (solid black line in the left panel), the vibration magnitude increases as the frequency increases, from 49 nm/Pa at 0.5 kHz until a broad peak at 1.6 kHz (R1, filled circular marker), with a peak magnitude of 83 nm/Pa, and then decreases. In the roll-off region after the R1 peak, there is another peak (R2) almost buried at 3.2 kHz (filled square marker) with a peak magnitude of 17 nm/Pa. (The identification of R2 with this frequency is ambiguous when looking at this curve alone, but it seems to be consistent with what is seen after the unloading phase, as described below, and with observations both in consecutive cycles and in other ears). Above about 3.6 kHz, the frequency response becomes complex. As the pressure is decreased from 0 Pa to −500, −1000, −1500, −2000 and −2500 Pa (solid red, green, blue, orange, and cyan, respectively), the 0.5-kHz magnitude decreases rapidly until −1500 Pa, then more or less plateaus at about 1 nm/Pa. R1 and R2 both shift to higher frequencies, changing rapidly until −1500 Pa, reaching 3.8 and 6.6 kHz with peak magnitudes of 0.32 and 8.4 nm/Pa, respectively. When the pressure is further decreased, R1 shifts back to lower frequencies and rises in magnitude, reaching 3.3 kHz with a peak magnitude of 1.6 nm/Pa at −2500 Pa; while R2 shifts to slightly higher frequencies and slightly larger magnitudes, reaching 8.0 kHz and 9.1 nm/Pa at −2500 Pa. The drops in the magnitudes of R1 and R2 to minima followed by rises were present in most gerbils, with the minimum occurring at −1000 or −1500 Pa. Several gerbils other than G31 also showed a minimum followed by a small rise in the lower-frequency magnitudes at these pressures.

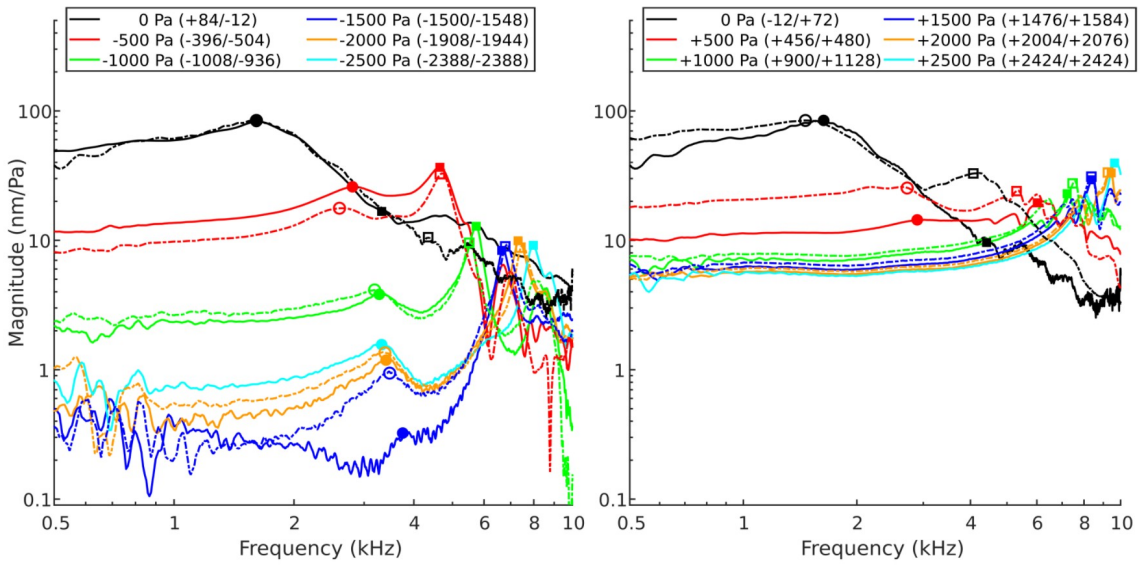


*Figure 3.8: Vibration response of G31 at the umbo for negative-pressure half-cycle (left) and positive-pressure half-cycle (right). Solid curves = loading phase, dashed = unloading phase. Circles (R1) and squares (R2) show the locations of the resonances in the loading (filled symbols) and unloading (empty symbols) phases. (Actual middle-ear pressure values are given in parentheses for both loading and unloading phases.)*

As the pressure is increased through the same pressure levels back to 0 Pa in the unloading phase (dashed lines in left panel), the low-frequency magnitude increases back to about 34 nm/Pa (somewhat lower than the original value of 49 nm/Pa at the start of the pressurization cycle) and both R1 and R2 (empty circular and square markers, respectively) shift back to lower frequencies. By 0 Pa, R1 and R2 have shifted back to 1.8 kHz and 3.7 kHz, respectively, somewhat higher than their original values of 1.6 kHz and 3.2 kHz, with peak magnitudes similar to their original values. Depending on which cycle was considered, the peak frequency for R1 and R2 at the same pressure level varied by as much as ±150 Hz. Hence, for more negative pressures where the peaks shifted less than 150 Hz, the peak frequency was considered to have stayed constant.

The positive-pressure half-cycle is shown in the right-hand panel of Figure 3.8. Overall, the positive-pressure half-cycle shows smaller changes in the vibration magnitude than the negative-pressure half-cycle does. The low-frequency magnitude decreases gradually as the pressure is increased, from 34 nm/Pa at 0 Pa to 5 nm/Pa at +2500 Pa. R1 (filled circular marker), at 1.7 kHz for 0 Pa, becomes very broad at 2.9 kHz for +500 Pa before disappearing for more positive

pressures. In some other ears, R1 was visible at +1000 Pa as well. R2 (filled square marker) also shifts to higher frequencies but becomes sharper as the pressure becomes more positive, reaching a frequency of 9.6 kHz with a peak magnitude of 40 nm/Pa at +2500 Pa. As the pressure is decreased back to 0 Pa (dashed lines), the low-frequency magnitude reaches about 60 nm/Pa (somewhat higher than its original value of 50 nm/Pa at the start of the negative-pressure half-cycle). R1 (empty circular marker) shifts back to 1.4 kHz, close to its original value of 1.6 kHz, while R2 (empty square marker) shifts back to 4.2 kHz, higher than its original value of 3.2 kHz. At each pressure level, the overall vibration magnitude is larger in the unloading phase than in the loading phase. This feature in the positive-pressure half-cycle was consistent across all gerbils, although the magnitude and frequency differences between loading and unloading were small in some gerbils.

Threshold criteria were used to identify the peaks. Most peaks exceeded a width threshold (200 Hz, measured at half height) and a height threshold (peak-to-base magnitude ratio greater than 1.05). If a peak was harder to identify, such as the nearly buried peaks at 0 Pa, it was confirmed in subsequent cycles at the same pressure level (or adjacent pressure levels where applicable) and for other gerbils (where the feature was in a similar frequency range). Any features that were not visible in other cycles were not considered as peaks. After a peak was identified, we confirmed that there was a corresponding positive slope in the phase.

Some of the trends seen in Figure 3.8 are illustrated in a different way in Figure 3.9, in which the frequencies and peak magnitudes of R1 (left panels) and R2 (right panels) are plotted as functions of the static pressure for all 11 gerbils. In the upper left panel, for G31, R1 is seen to quickly shift from 1.6 kHz at 0 Pa to 3.2 kHz at −1000 Pa, and then stay close to about 3 kHz for higher pressures. For other gerbils, the R1 frequency can shift to as high as 4.4 kHz (G21) or as low as 2.2 kHz (G22). In the positive-pressure half-cycle of G31, R1 shifts only slightly higher at +500 Pa and was not visible for more positive pressures. In other ears also, for positive pressures the R1 frequency usually shifted only slightly, with a few exceptions. In G28, R1 was still visible even at +1000 Pa. R2 (upper right panel) shifts to much higher frequencies than R1 does. For G31, R2 keeps shifting to higher frequencies until −2500 Pa, reaching around 8.0 kHz. In the positive-pressure half-cycle, R2 shifts to even higher frequencies, reaching 9.6 kHz at +2500 Pa. The R2 frequencies are fairly similar from ear to ear in the negative-pressure half-cycle, varying from 6 to 9 kHz at −2500 Pa. In the positive-pressure half-cycle, the variability is much larger,

with some ears showing a progressive shift to frequencies up to around 10 kHz, while others rise up to about 6 kHz. G22 is an exception, with the R2 frequency staying at about 3 kHz.

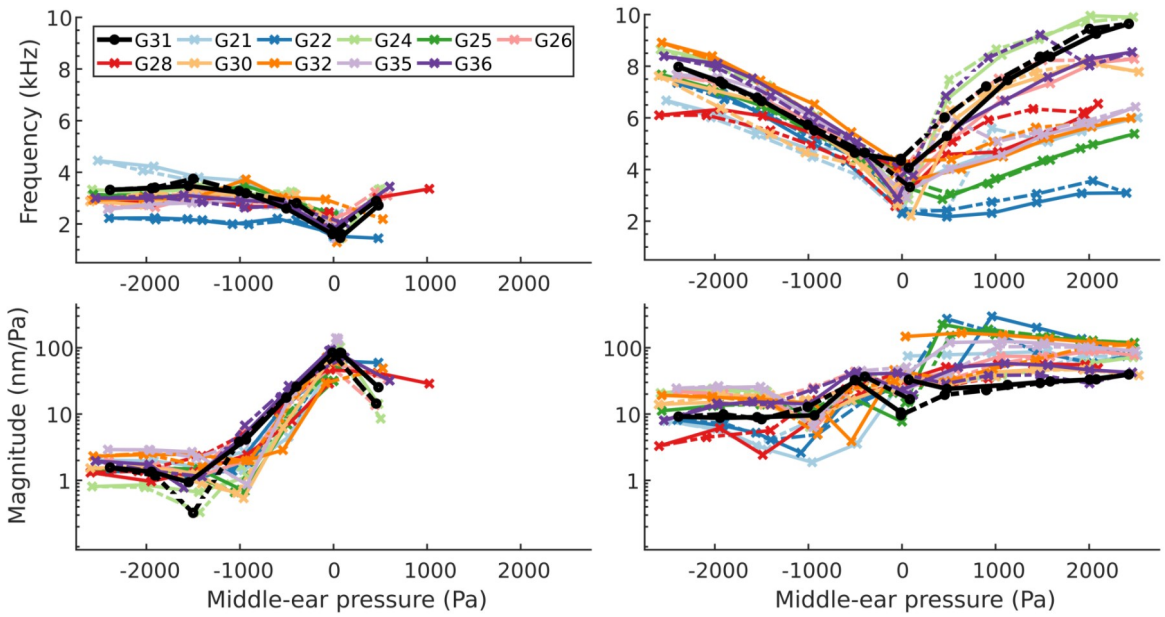


*Figure 3.9:* Behaviour of frequency-response peaks (as defined in the text) at the umbo, as functions of middle-ear pressure, for all 11 gerbils. Left panels = R1, right panels =R2. Top panels = peak frequency, bottom panels = peak magnitude. The green arrow indicates the dip in magnitude mentioned in the text.

In the lower left panel of the figure, the R1 peak magnitude for G31 decreases as the static pressure decreases to −1500 Pa, and then increases slightly to 1.6 nm/Pa when the pressure is decreased further to −2500 Pa. The minimum occurs at −1000 Pa for some gerbils. The R1 peak magnitudes at −2500 Pa vary from 0.9 to 3.0 nm/Pa. The R1 peak magnitude decreases slightly in the positive-pressure half-cycle at pressures where it was visible. The R2 peak magnitude (lower right panel) for G31 stays almost constant throughout the cycle, but some gerbils show a slight decrease in the negative-pressure half-cycle, and a slight increase in the positive-pressure half-cycle. All of the gerbils tend to show larger magnitudes for positive pressures than for negative pressures.

Figure 3.10 shows the vibration responses for a point at the mid-manubrium, again for gerbil G31. The initial nominally unpressurized vibration in the left panel has a low-frequency magnitude of about 50 nm/Pa (the same magnitude as at the umbo). R1 has a broad peak at

1.6 kHz (the same frequency as at the umbo) with a magnitude of 77 nm/Pa (similar to the 83 nm/Pa seen at the umbo). R2 has a small peak at 3.6 kHz (close to the frequency of 3.2 kHz seen at the umbo) with a magnitude of 16 nm/Pa (similar to the 17 nm/Pa seen at the umbo). As the pressure is decreased, the low-frequency magnitude again decreases, this time to about 2 nm/Pa (compared to the 1 nm/Pa seen at the umbo). The R1 and R2 frequencies shift upward, reaching 2.7 kHz and 8.1 kHz, respectively, at −2500 Pa (compared with 3.3 and 8.0 kHz, respectively, at the umbo). A dip in magnitude, similar to what was observed at the umbo, occurs at about −1500 Pa, where the R1 peak magnitude drops to 0.3 nm/Pa. Similar to what was observed at the umbo, when the pressure is increased back to 0 Pa, the low-frequency magnitude rises and the R1 and R2 peaks shift back to close to their original values. In the positive-pressure half-cycle, the low-frequency magnitude decreases from about 34 nm/Pa at 0 Pa to about 7.6 nm/Pa at +1500 Pa, then increases slightly to about 8.5 nm/Pa at +2500 Pa. The R1 broad peak at 2.0 kHz at 0 Pa shifts to about 2.8 kHz at +500 Pa and then becomes buried at about 3.0 kHz for more positive pressures, similar to what is seen at the umbo where the R1 peak becomes buried at about the same frequency and pressure(Several gerbils showed a slight R1 peak up to +1000 Pa at the umbo and/or the mid-manubrium). R2 shifts upward to 7.6 kHz at +1500 Pa before shifting back downward to 6.9 kHz at +2500 Pa. When the pressure is decreased back to 0 Pa, the low-frequency magnitude increases up to 52 nm/Pa, close to its original value of 50 nm/Pa. As seen at the umbo, the low-frequency vibration magnitudes (up to about 1.5 kHz) are higher in the unloading phase than in the loading phase. R1 and R2 shift back to 1.4 kHz and 3.2 kHz, respectively, compared with their original values of 1.6 kHz and 3.6 kHz. The low-frequency magnitude decreases more when the pressure is decreased to −2500 Pa than when it is increased to +2500 Pa, similar to what is seen at the umbo.

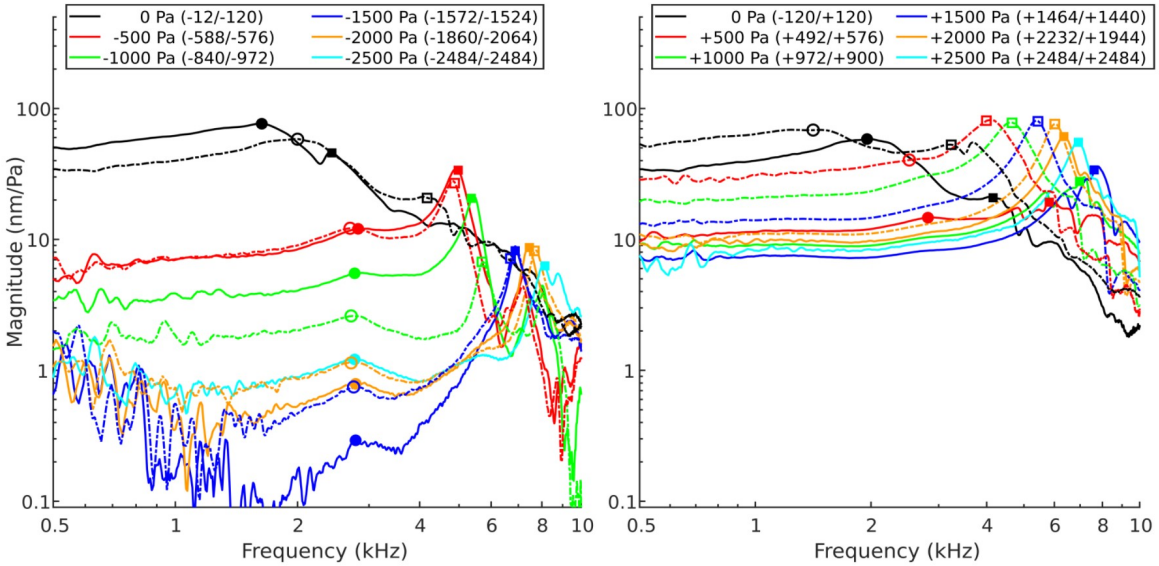


*Figure 3.10: Vibration response of G31 at the* mid-manubrium *for negative-pressure half-cycle (left) and positive-pressure half-cycle (right). Solid curves = loading phase, dashed = unloading phase. Circles (R1) and squares (R2) show the locations of the resonances in the loading (filled symbols) and unloading (empty symbols) phases. (Actual middle-ear pressure values are given in parentheses for both loading and unloading phases.)*

### 3.3.4 Pars-tensa response

Figure 3.11 shows the pressurized vibration responses for a point on the posterior pars tensa, again for G31. At the beginning of the negative-pressure half-cycle (solid black curve in left panel), the vibration magnitude increases with frequency from about 60 nm/Pa until a broad peak at 1.7 kHz (similar to the R1 peak at manubrial points) with a peak magnitude of 85 nm/Pa, immediately followed by a sharp minimum with a minimum magnitude of 60 nm/Pa at 2.3 kHz. There is then a double-peak feature with peak frequencies at 2.7 kHz (similar to the peak frequency of R2 on the manubrium) and 3.7 kHz, with individual peak magnitudes of 280 and 225 nm/Pa, respectively. When the pressure is decreased, the low-frequency (0.5-kHz) magnitude decreases to about 4 nm/Pa at −2500 Pa. At −500 Pa, the R1 peak is almost buried at about 2.8 kHz, and it is not seen at all at more negative pressures. The following minimum has already disappeared at −500 Pa. The R2 double-peak feature merges into a single peak, at higher frequencies, as the pressure is decreased, reaching as high as 8.1 kHz with a peak magnitude of 42 nm/Pa at −2500 Pa. When the pressure is increased back to 0 Pa, the low-frequency magnitude increases back to 71 nm/Pa; R1 shifts back to 1.7 kHz; the sharp minimum returns at 2.8 kHz; and R2 is visible as closely spaced peaks again, at 3.4 and 4.4 kHz. In the positive-

pressure half-cycle, the low-frequency magnitude decreases gradually to 5.3 nm/Pa at +1000 Pa and stays approximately constant for more positive pressures. R1 and the following minimum shift to 2.9 kHz and 4.0 kHz at +500 Pa, and both disappear for pressures more positive than +500 Pa. R2 shifts to higher frequencies in a cluster of peaks, the earliest of them reaching 7.8 kHz at 55 nm/Pa by +2500 Pa. For some of the other pressurization cycles, the R2 peaks shift beyond 10 kHz. When the pressure is decreased back to 0 Pa, the low-frequency magnitude recovers back to 58 nm/Pa, similar to its original value of 61 nm/Pa; R1 reappears as a broad peak of 123 nm/Pa at 1.7 kHz, close to its original value; and R2 appears as a single peak at 2.5 kHz with a peak magnitude of 255 nm/Pa, close to the original double-peak values of 280 and 255 nm/Pa, respectively. For some of the other cycles measured in this gerbil, and for all three consecutive cycles in the other gerbil (G32) in which posterior pars-tensa responses were measured, R2 reappeared as a double-peak feature when the pressure was increased back to 0 Pa. (The anterior pars-tensa responses in G32 had similar vibration magnitudes for all pressure steps but R2 appeared as a single peak, even at 0 Pa). Similar to what is seen at the manubrial points, the unloading curves for the positive-pressure half-cycle have higher magnitudes than the loading curves do at the same pressure levels, at least at frequencies lower than 5 kHz.

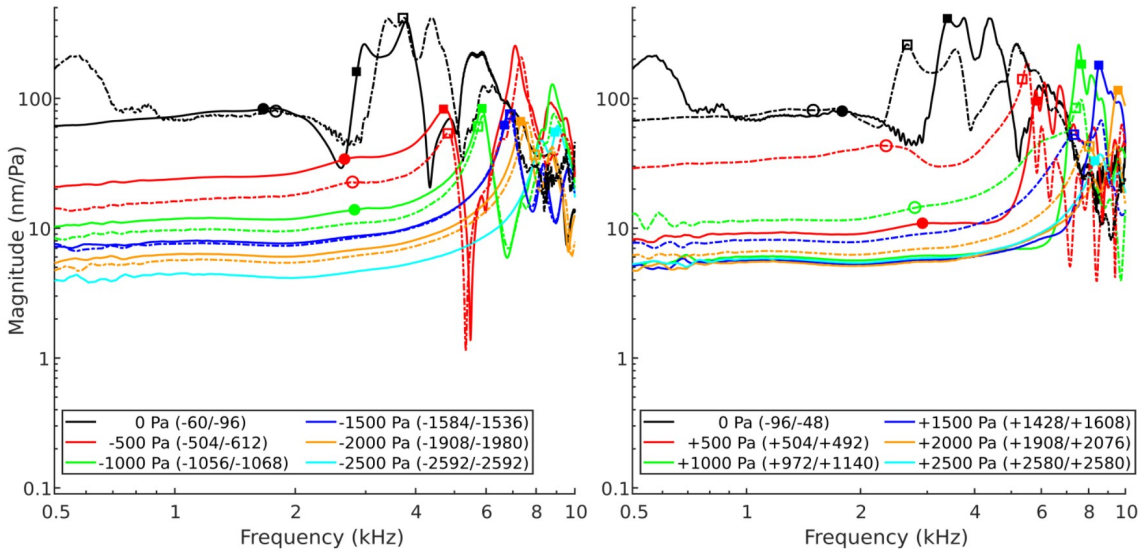


*Figure 3.11: Vibration response of G31 at the* posterior pars tensa *for negative-pressure half-cycle (left) and positive-pressure half-cycle (right). Solid curves = loading phase, dashed = unloading phase. Circles (R1) and squares (R2) show the locations of the resonances in the loading (filled symbols) and unloading (empty symbols) phases. (Actual middle-ear pressure values are given in parentheses for both loading and unloading phases.)*

Figure 3.12 shows the peak frequencies and magnitudes for R1 and R2 on the posterior pars tensa over the pressure cycle, analogous to Figure 3.9. Posterior pars-tensa responses were recorded in 4 gerbils: G24, G30, G31, and G36. For G31, R1 (upper left panel) can only be identified for pressures between −1000 and +1000 Pa, and the pressure range was even smaller for other gerbils. The R1 frequency increases when pressure is applied. The R2 frequency (upper right panel) shows a monotonic increase as the pressure is decreased (with the exception of the value at −500 Pa for G36), reaching as high as 8.9 kHz at −2500 Pa, and there is little difference between the loading and unloading curves. In the positive-pressure half-cycle, except for G36, the R2 frequency increases rapidly until +1000 Pa, then stays approximately constant for more positive pressures, at frequencies similar to those of the negative-pressure half-cycle. For G36 the R2 frequency shifts much less. There is a large difference between the loading and unloading curves in the positive-pressure half-cycle for G31, especially for pressures more positive than +1000 Pa. When G36 is excluded, there is similar variability in the R2 frequencies in the negative-pressure and positive-pressure half-cycles. The R1 peak magnitudes (lower left panel) decreased (until the peak disappeared) when the pressure was either decreased or increased from

0 Pa. There was less variability among the gerbils in the negative-pressure half-cycle. The R2 peak magnitude (lower right panel) for G31 shows a sharp decrease from 0 Pa to −500 Pa, and then stays mostly constant for more negative pressures. The initial sharp decrease seen in G31 is smaller for some other gerbils. In the positive-pressure half-cycle, the R2 peak magnitude shows an irregular decrease, decreasing to a lower magnitude than in the negative-pressure half-cycle, except for G36, where the R2 peak magnitude increases slightly between 0 Pa and +500 Pa before decreasing monotonically. As the pressure is decreased back toward 0 Pa, the magnitude returns to nearly the value it had at the beginning of the negative-pressure half-cycle for all gerbils.

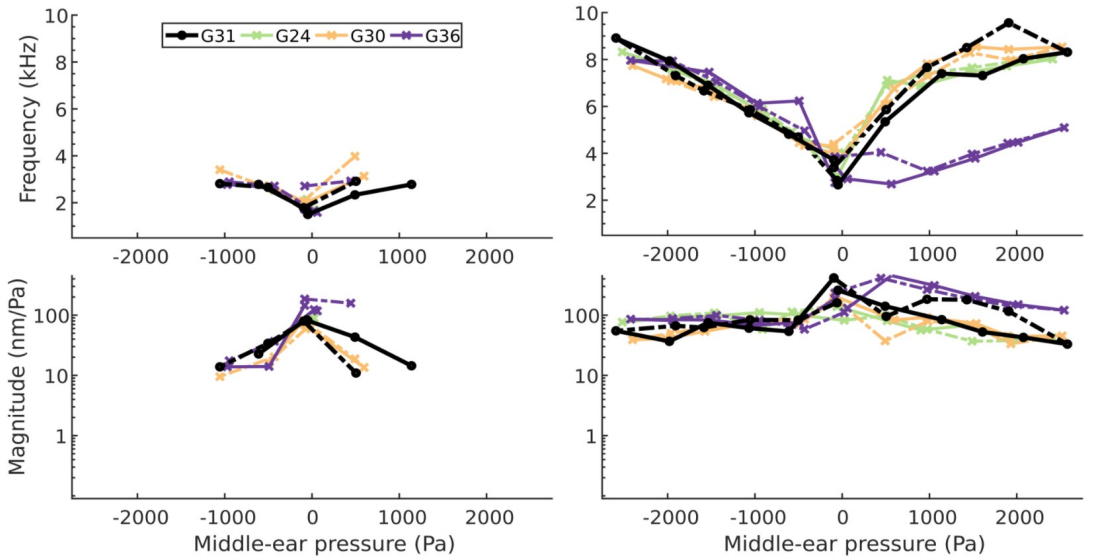


*Figure 3.12:* Behaviour of frequency-response peaks (as defined in the text) at the posterior pars tensa, as functions of the middle-ear pressure, for four gerbils. Left panels = R1, right panels =R2. Top panels = peak frequency, bottom panels = peak magnitude.

### 3.3.5 Pars-flaccida response

The pressurized vibration responses for a point on the pars flaccida of G31 are shown in Figure 3.13. At the beginning of the negative-pressure half-cycle (solid black curve in left panel), the vibration magnitude shows an almost buried peak at 1.4 kHz (R1 – circular marker, corresponding to the R1 observed on the pars tensa and manubrium), with a peak magnitude of

145 nm/Pa. After a broad peak at 2.2 kHz (R2 – square marker, corresponding to the R2 observed on the pars tensa and the manubrium) with a peak magnitude of 182 nm/Pa, and a small notch at 3.7 kHz, the vibration magnitude decreases steadily at about 35 dB/octave. This rate is calculated by fitting a line between the beginning of the descent, after the small peak around 3.7 kHz, and about 10 kHz. Unlike the manubrial and pars-tensa points, an additional low-frequency peak (R0 – triangular marker) is visible at 0.75 Hz with a peak magnitude of 96 nm/Pa. This peak was only visible on the pars flaccida, and is designated R0 since it occurs at lower frequencies than R1. As the pressure is becomes negative, however, the shape of the frequency response changes drastically. At −500 Pa, the 0.5-kHz magnitude is down to around 8 nm/Pa; the vibration magnitude increases slowly as the frequency increases until R0 at around 1.1 kHz; decreases rapidly until a sharp minimum at 2.0 kHz; then increases until a distinct R1 at 2.7 kHz; followed by numerous peaks and troughs at higher frequencies with R2 at 4.9 kHz. As the pressure is decreased further to −2500 Pa, the low-frequency magnitude decreases to about 2 nm/Pa; R0 becomes buried in the region before the sharp minimum at around 1.8 kHz; and R1 and R2 shift to higher frequencies, reaching 3.7 and 8.1 kHz, respectively, by −2500 Pa. When the pressure has returned back to 0 Pa, R0 is barely visible at 0.8 kHz with a peak magnitude of 25 nm/Pa; the sharp minimum before R1 disappears; and R1 and R2 shift back to around 1.5 kHz and 4.1 kHz, with peak magnitudes of 38 and 14 nm/Pa, respectively. Numerous peaks and troughs at frequencies higher than R1 are still visible, unlike the original smooth frequency-response shape at the beginning of the cycle.

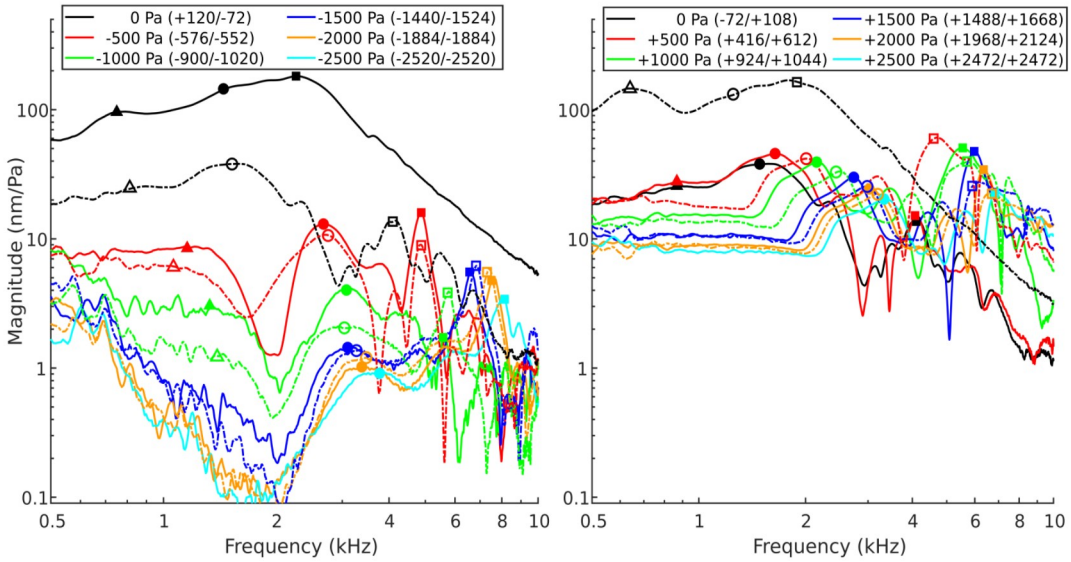


*Figure 3.13: Vibration response of G31 at the* pars-flaccida *for negative-pressure half-cycle (left) and positive-pressure half-cycle (right). Solid curves = loading phase, dashed = unloading phase. Circles (R1) and squares (R2) show the locations of the resonances in the loading (filled symbols) and unloading (empty symbols) phases. (Actual middle-ear pressure values are given in parentheses for both loading and unloading phases.)*

In the positive-pressure half-cycle (right-hand panel), as the pressure is increased from 0 Pa to +500 Pa, the peak magnitudes of R0, R1, and R2 actually increase slightly. (This increase in magnitudes was larger for other pressurization cycles, where they increased significantly between 0 Pa and +500 Pa or +1000 Pa). As the pressure is then made more positive, R0 disappears, and R1 and R2 shift to higher frequencies; their peak magnitudes start to decrease after +1000 Pa for R1 and after +1500 Pa for R2. R1 and R2 reach 3.3 and 6.7 kHz, respectively, at +2500 Pa. When the pressure is decreased back to nominally 0 Pa, the frequency response (dashed black curve in right panel) returns nearly to the shape of the original curve (solid black curve in left panel), with the 500-Hz magnitude now at 100 nm/Pa (larger than its original value of 58 nm/Pa); followed by R0 and an almost buried R1 at 0.64 and 1.3 kHz (somewhat lower than their original values of 0.75 and 1.4 kHz), followed by a broad R2 at 1.9 kHz (somewhat lower than its original value of 2.3 kHz) with a peak magnitude of 163 nm/Pa (somewhat lower than its original 182 nm/Pa); followed by a steady decrease of about 35 dB/octave (the same as originally).

The behaviour of the frequencies and magnitudes of R1 and R2 as functions of the static pressure are shown for the pars flaccida in Figure 3.14. Pars-flaccida responses were recorded in

G31 and G32. In the negative-pressure half-cycle, the R1 frequencies (upper left panel) for both G31 and G32 shift gradually from around 1.4 kHz at 0 Pa to higher frequencies for both negative and positive pressures. The R1 frequency for G31 is higher than that of G32 at all pressure levels, reaching 3.7 and 3.3 kHz at −2500 and +2500 Pa, respectively. The R2 peak frequency of G31 (upper right panel) starts at 1.9 kHz at 0 Pa, and shifts more than R1 does, reaching 8.1 and 6.8 kHz at −2500 and +2500 Pa, respectively. The R2 frequencies of G32 are mostly lower than those of G31, with a few exceptions between 0 Pa and +1000 Pa where they are similar. The R2 frequency of G31 shifts less in the positive-pressure half-cycle than in the negative-pressure half-cycle (the opposite of what happens on the manubrium), but this is not the case for G32.

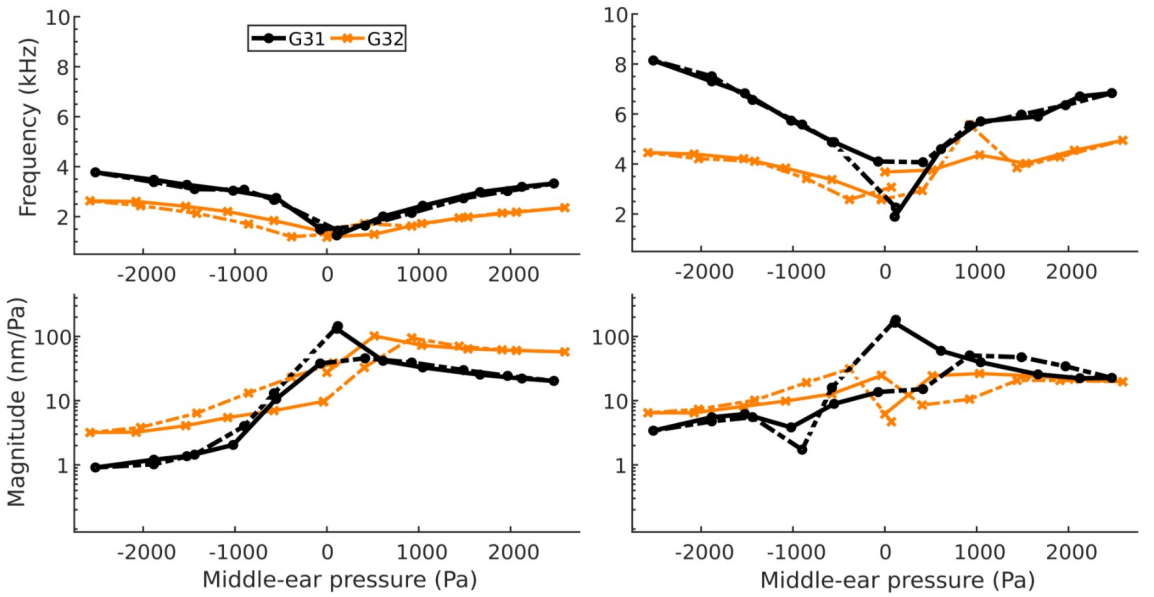


*Figure 3.14:* Behaviour of frequency-response peaks (as defined in the text) at the pars flaccida, as functions of the middle-ear pressure, for gerbils G31 and G32. Left panels = R1, right panels =R2. Top panels = peak frequency, bottom panels = peak magnitude.

The R1 and R2 peak magnitudes (lower left panel) for G31 both decrease when the pressure becomes less than zero. As the pressure is increased back to zero, the R1 peak magnitude increases to much higher than its original value. In the positive-pressure half-cycle, the R1 peak magnitude decreases as the pressure becomes positive. When the pressure is decreased back to zero, the R1 peak magnitude increases only until +500 Pa, and returns to its original value. G32 shows similar behaviour except that the magnitude changes are smaller, and the largest peak

magnitudes occur at +500 Pa and +1000 Pa in the loading and unloading phases, respectively. The R2 peak magnitude (lower right panel) for G31 shows a distinct dip at −1000 Pa, whereas for G32 the R2 peak magnitude shows smaller and less regular changes, and the largest peak magnitudes occur at −500 Pa and +500 Pa in the unloading phases for the negative-pressure and positive-pressure half-cycles, respectively. The dip in the R2 peak magnitude seen here for G31 was not observed in all pressurization cycles for that ear, nor for G32, and was thus not as consistent as the similar dip of the manubrium response. The R1 and R2 peak magnitudes (for both G31 and G32) start at similar values at 0 Pa, but the R1 peak magnitude decreases to a fraction of the R2 peak magnitude at −2500 Pa (a quarter for G31 and less than half for G32). Even though the R1 and R2 peak magnitudes varied between G31 and G32, the low-frequency magnitude behaviours were similar in all cycles.

## 3.4 Discussion

In this study, we performed in-vivo vibration measurements on 11 gerbil ears under quasi-static pressure steps in the middle-ear cavity while the ear canal was kept at ambient pressure with a ventilation tube. The vibration responses at the umbo when both sides of the eardrum were at ambient pressure were fairly consistent with previous studies (Maftoon et al. 2013). Our frequency responses had an overall larger range across ears with generally lower magnitudes and higher frequencies of the peaks. These differences could be due to dehydration during preparation, when both the eardrum and the middle-ear were exposed. Rehydration between cycles was not possible due to the fixation of the acoustic coupler to the bony ear canal and the fixation of the pressurization tube in the bulla. The effects of dehydration have been studied during various middle-ear vibration measurements (e.g., Gyo et al. 1986; Rosowski et al. 1990; Voss et al. 2001; Kei et al. 2003; Ellaham et al. 2007; Maftoon et al. 2013). Maftoon et al. (2013) measured a maximum peak shift to higher frequencies of about 2 Hz/min, and a maximum peak magnitude decrease of about 0.2 %/min, over a time span of 90 minutes for the unpressurized vibration response at the umbo. This shift was within the variability in our results over the time span of two hours, but our measurements did not a show consistent shift.

The overall vibration magnitude decreased significantly after the first ever pressurization cycle, possibly due to preconditioning. Another factor that may have contributed to this change is the variability in the static pressure (up to ±100 Pa) at each step. However, these cycle-to-cycle

changes in vibration magnitudes at any given pressure, even over a period of two hours, were smaller than the changes caused by the presence of static pressure.

When a static pressure was applied, the low-frequency magnitude decreased, and the peak frequencies shifted to higher frequencies. These changes were more rapid at pressures closer to zero, and started to plateau for pressures closer to ±2500 Pa. The changes were greater, in both magnitudes and frequencies, for negative ear-canal pressures than for positive ones for all points on the eardrum, except for some cycles on the pars flaccida in some ears. These trends are consistent with previous gerbil vibration measurements, both unpressurized (Rosowski et al. 1999; de La Rochefoucauld and Olson 2010) and pressurized (Lee and Rosowski 2001; Shapiro 2014), and also with pressurized gerbil eardrum shape measurements (von Unge et al. 1993; Dirckx and Decraemer 2001; Gea et al. 2010). For both manubrial points, the low-frequency magnitude and the R1 peak magnitude each showed a dip at −1000 to −1500 Pa, depending on the cycle. Even though the magnitude difference was small in some ears, the presence of the dip was fairly robust. This phenomenon may be due to a buckling of the eardrum, or perhaps to some effect in the ossicular chain. Lee and Rosowski (2001) observed a similar dip in magnitude at the umbo (but not on the pars flaccida) around −2000 Pa, for frequencies between 1 and 6 kHz.

There were generally also magnitude differences, sometimes small, between the loading and unloading curves for both negative and positive pressurization half-cycles. For the negative-pressure half-cycle, the vibration magnitudes were higher in the loading phase than in the unloading phase, and vice-versa for the positive-pressure half-cycle (except for some positive-pressure steps on the pars flaccida). This was seen to some extent in all ears. This difference could be due to hysteresis. Hysteresis in response to quasi-static pressures on the gerbil eardrum has been reported before. For example, pressurized moiré measurements of eardrum shape resulted in hysteresis loops (e.g., von Unge et al. 1993; Dirckx and Decraemer 2001), and Lee and Rosowski (2001) observed differences in the peak magnitude and frequency of vibrations for different directions of the pressure steps.

The overall vibration magnitudes at the mid-manubrium and at the umbo were similar at any given pressure, slightly larger at the mid-manubrium in some ears. (Maftoon et al. 2013) observed a systematic difference with the unpressurized umbo vibration magnitude being larger than that at the mid-manubrium, consistent with the classical view of rotation of the malleus

around a fixed axis of rotation. The lack of a clear difference in magnitude here may be attributable, at least in part, to the inaccuracy (±100 Pa) of our pressure steps.

Both manubrial points showed another peak at higher frequencies (R2 in the Results section), which became more distinct and shifted to higher frequencies when the pressure became either more negative or more positive. The amount that the R2 frequency shifted changed from location to location. For the posterior pars tensa, R2 showed as a double peak; Maftoon et al. (2013) also observed a double-peak feature at a similar location on the eardrum. In the positive-pressure half-cycle, R2 appeared as a series of closely-spaced peaks. The anterior pars-tensa frequency response was similar in shape to those of the manubrial points, but with larger overall magnitudes at the same pressure levels. The double-peak feature in the negative-pressure half-cycle on the posterior pars tensa, and the closely spaced peaks in the positive-pressure half-cycle, suggest that R2 may be a superimposition of small peaks on the manubrium but that these peaks become separate at some pressures on the pars tensa. The R1 and R2 peak heights both became larger at non-zero pressures, but the peak widths stayed mostly constant as pressure was decreased beyond −500 Pa or increased beyond +500 Pa. In some measurements, especially on the pars flaccida, the R1 and R2 peaks were close in frequency at 0 Pa, but ended up much further apart when the pressure was decreased. They reacted differently to the static pressure, presumably because different parts of the middle ear contributed differently when the pressure was decreased.

The pars-flaccida unpressurized frequency response was similar in shape to the manubrial response as well, with a few exceptions. The magnitude was significantly larger, as observed previously (Merchant et al. 1997; Rosowski et al. 1999; Lee and Rosowski 2001; Maftoon et al. 2013); a pars-flaccida peak (R0 in the Results section) appeared at 0.7 kHz, which was also previously reported (Lee and Rosowski 2001; Maftoon et al. 2013). R1 and R2 were present as almost buried peaks, similar to what was seen for the manubrial points. As the pressure was decreased to −500 Pa and below, however, the R0, R1, and R2 peaks became distinct with local minima between the peaks. This change in mode is consistent with the large deformation of the pars flaccida in the presence of even small static pressures. Dirckx et al. (1998) observed such large deformations for pressures as small as ±100 Pa. Teoh et al. (1997) suggested that the pars flaccida's larger deformation could be limiting the deformation of the pars tensa, effectively stiffening the pars tensa and ossicular chain.

In this study, we aimed to provide insight into the effects of middle-ear-cavity static pressures on the vibration response of the gerbil eardrum. We developed an in-vivo gerbil ear model and observed the vibration responses at multiple locations. The vibration responses over a wide frequency range for multiple pressurization cycles were given and the main resonance peaks were identified. These pressure-step responses will be useful for validating numerical models of the gerbil middle ear in conjunction with previous shape and vibration measurements that involved pressure steps. For more direct relevance to tympanometry, it will be necessary to apply the quasi-static pressures in the ear canal rather than in the middle ear, and to perform similar multiple-point vibration measurements with a sweep pressure input, which is more difficult experimentally because of the need to track the beads throughout the pressurization sweep. In the meantime, these data do provide some insight into the effects of normal and pathological changes in middle-ear pressure as reflected in clinically observed variations of the tympanometric peak pressure (TPP) due to Eustachian tube function (e.g., the interval between swallows) and dysfunction (blockage).

## Acknowledgements

The authors would like to thank Dr. Aurore Dodelet-Devillers for her help with the handling of the animals, anaesthesia, and surgical procedures; Dr. Ross Wagner for his help in the development of the acoustic coupler and the experimental setup; Mr. Sajjad Feizollah and Dr. Majid Soleimani for their help with the surgical procedure; and the McGill University Health Centre Research Institute Vivarium staff for their help in maintaining and advising on the health and comfort of the animals. This work was supported in part by the Canadian Institutes of Health Research, the Natural Sciences and Engineering Research Council (Canada), the Fonds de recherche en santé du Québec, the Montréal Children’s Hospital Research Institute, and the McGill University Health Centre Research Institute.

## Conflict-of-interest disclosure statement

The authors declare that they have no conflict of interest.

## References


Akache, F., Funnell, W. R. J., & Daniel, S. J. (2007). An experimental study of tympanic membrane and manubrium vibrations in rats. Audiology and Neuro-Otology, 12(1), 49–58.

Decraemer, W. F., Dirckx, J. J., & Funnell, W. R. J. (1991). Shape and derived geometrical parameters of the adult, human tympanic membrane measured with a phase-shift moire interferometer. Hearing research, 51(1), 107–121.

Decraemer, W. F., & Dirckx, J. J. J. (1998). Pressure regulation due to displacement of the pars flaccida and pars tensa of the tympanic membrane. ORN, 8(6), 277–281.

Decraemer, W. F., & Khanna, S. M. (2000). Three-dimensional vibration of the ossicular chain in the cat (Vol. 4072, pp. 401–411). Presented at the Fourth International Conference on Vibration Measurements by Laser Techniques: Advances and Applications. Retrieved from http://dx.doi.org/10.1117/12.386747

Decraemer, W. F., Khanna, S. M., & Funnell, W. R. J. (1997). Vibrations of the cat tympanic membrane measured with high spatial resolution. Presented at the 20th Midwinter Res. Mtg. Assoc. Res. Otolaryngol., St. Petersburg Beach, FL. Retrieved from zotero://attachment/19/

Dirckx, J. J., & Decraemer, W. F. (1991). Human tympanic membrane deformation under static pressure. Hearing research, 51(1), 93–105.

Dirckx, J. J. J., Buytaert, J. A. N., & Decraemer, W. F., W. F. (2006). Quasi-static transfer function of the rabbit middle ear, measured with a heterodyne interferometer with high-resolution position decoder. JARO, 7(4), 339–351.

Dirckx, J. J. J., & Decraemer, W. F. (2001). Effect of middle ear components on eardrum quasi-static deformation. Hearing Research, 157(1), 124–137.

Dirckx, J. J. J., Decraemer, W. F., von Unge, M., & Larsson, C. (1998). Volume displacement of the gerbil eardrum pars flaccida as a function of middle ear pressure. Hearing Research, 118(1), 35–46.

Ellaham, N. N., Akache, F., Funnell, W. R. J., & Daniel, S. J. (2007). Spatial vibration patterns of the gerbil eardrum. Canadian Acoustics, 35(4), 38–39.

Engel, J. (2008). Gerbils can tune in. J Physiol, 586(Pt 4), 919.

Gladiné, K., & Dirckx, J. J. J. (2019). Strain distribution in rabbit eardrums under static pressure. Hearing Research, 381, 107772.

Gyo, K., Goode, R. L., & Miller, C. (1986). Effect of middle ear modification on umbo vibration: human temporal bone experiments with a new vibration measuring system. Archives of Otolaryngology–Head & Neck Surgery, 112(12), 1262–1268.

Isaacson, J. E., & Vora, N. M. (2003). Differential diagnosis and treatment of hearing loss. American family physician, 68(6), 1125—1132.

de La Rochefoucauld, O., & Olson, E. S. (2010). A sum of simple and complex motions on the eardrum and manubrium in gerbil. Hearing research, 263(1), 9–15.

Lee, C.-Y., & Rosowski, J. J. (2001). Effects of middle-ear static pressure on pars tensa and pars flaccida of gerbil ears. Hearing Research, 153(1), 146–163.

Maftoon, N., Funnell, W. R. J., Daniel, S. J., & Decraemer, W. F. (2013). Experimental study of vibrations of gerbil tympanic membrane with closed middle ear cavity. JARO, 14(4), 467–481.

Maftoon, N., Funnell, W. R. J., Daniel, S. J., & Decraemer, W. F. (2014). Effect of opening middle-ear cavity on vibrations of gerbil tympanic membrane. JARO, 15(3), 319–334.

Maftoon, N., Funnell, W. R. J., Daniel, S. J., & Decraemer, W. F. (2015). Finite-element modelling of the response of the gerbil middle ear to sound. JARO, 16(5), 547–567.

Maftoon, N., Nambiar, S., Funnell, W. R. J., Decraemer, W. F., & Daniel, S. J. (2011). Experimental and modelling study of gerbil tympanic-membrane vibrations. 34th Midwinter Research Meeting, Association for Research in Otolaryngology (pp. 19–23).

Ravicz, M. E., & Rosowski, J. J. (1997). Sound-power collection by the auditory periphery of the mongolian gerbil Meriones unguiculatus: III. Effect of variations in middle-ear volume. The Journal of the Acoustical Society of America, 101(4), 2135–2147. Acoustical Society of America.

Ravicz, M. E., Rosowski, J. J., & Voigt, H. F. (1992). Sound-power collection by the auditory periphery of the mongolian gerbil Meriones unguiculatus. I: Middle-ear input impedance. The Journal of the Acoustical Society of America, 92(1), 157–177.

Rosowski, J. J., Davis, P. J., Donahue, K. M., Merchant, S. N., & Coltrera, M. D. (1990). Cadaver middle ears as models for living ears: comparisons of middle ear input immittance. Ann Otol Rhinol Laryngol, 99(5), 403–412.

Rosowski, J. J., Ravicz, M. E., Teoh, S. W., & Flandermeyer, D. (1999). Measurements of middle-ear function in the Mongolian gerbil, a specialized mammalian ear. Audiology and Neurotology, 4(3–4), 129–136.

Ruggero, M. A., & Temchin, A. N. (2003). Middle-ear transmission in humans: wide-band, not frequency-tuned? Acoustics Research Letters Online, 4(2), 53–58.

Shapiro, R. (2014). An experimental study of vibrations in the gerbil middle ear under static pressure (M.Eng. thesis). Montreal, Canada: McGill University. Retrieved from http://digitool.library.mcgill.ca/R/-?func=dbin-jump-full&object_id=126993&silo_library=GEN01

Teoh, S. W., Flandermeyer, D. T., & Rosowski, J. J. (1997). Effects of pars flaccida on sound conduction in ears of Mongolian gerbil: acoustic and anatomical measurements. Hearing Research, 106(1–2), 39–65.

von Unge, M., Decraemer, W. F., Bagger-Sjöbäck, D., & Dirckx, J. J. (1993). Displacement of the gerbil tympanic membrane under static pressure variations measured with a real-time differential moire interferometer. Hearing Research, 70(2), 229–242.

Voss, S. E., Rosowski, J. J., Merchant, S. N., & Peake, W. T. (2001). Middle-ear function with tympanic-membrane perforations. I. Measurements and mechanisms. The Journal of the Acoustical Society of America, 110(3), 1432–1444.

Zheng, Y., Ohyama, K., Hozawa, K., Wada, H., & Takasaka, T. (1997). Effect of anesthetic agents and middle ear pressure application on distortion product otoacoustic emissions in the gerbil. Hearing Research, 112(1), 167–174.

# Chapter 4: Vibration measurements of the gerbil eardrum under quasi-static pressure sweeps

Submitted to the *Journal of the Association for Research in Otolaryngology*, 2021 September.

This chapter is a continuation of the study of the previous chapter. Following that study, we were confident that the vibration response under slow ramps could be measured after some modifications to the experimental setup. In order to produce pressure ramps, the pressurization system was modified to accommodate control over the pressurization rate. Due to limitations of the manual tracking of the beads, only pars tensa and manubrium points are reported. The use of pressure ramps allowed measurements at small pressure changes throughout the cycle. Furthermore, modification to the data acquisition method improved data collection.

The full frequency spectra of the data are reported using spectrograms, and compared to results from the previous study. Furthermore, features in the frequency domain that were observed in the previous step-wise responses are seen in more detail here.

**ABSTRACT:** Tympanometry provides an objective measurement of the status of the middle ear. During tympanometry, the ear-canal pressure is varied while the response of the ear to sound pressure is measured. The effects of the pressure on the mechanics of the middle ear are not well understood. This study is a continuation of our previous work in which the vibration response of the gerbil eardrum was measured in vivo under quasi-static pressure steps. In this study we delivered a continuous pressure sweep to the middle ear, and measured the vibration response at four locations for 6 gerbils. Vibrations were recorded using a single-point laser Doppler vibrometer and glass-coated reflective beads (diameter ~40 μm) at the umbo and on the mid-manubrium, posterior pars tensa and anterior pars tensa.

The vibration magnitudes were similar to those in the previous step-wise pressurization experiments. Most gerbils showed repeatability within less than 10 dB for consecutive cycles. As described in the previous study, as the frequency was increased at ambient pressure the vibration magnitude on the manubrium increased slightly to a broad peak (referred to as R1) then decreased until a small peak appeared (referred to as R2), followed by multiple peaks and troughs as the magnitude decreased further. The low-frequency vibration magnitude (at 1 kHz) decreased monotonically as the pressure became more negative except for a dip (about 500 Pa wide) that occurred between −700 and −1800 Pa. The lowest overall magnitude was recorded in the dip at mid-manubrium. The vibration magnitudes also decreased as the middle-ear pressure was made more positive and were larger than those at negative pressures. R1 was only visible at negative and small positive middle-ear pressures, while R2 was visible for both positive and negative pressures. R2 split into multiple branches after the middle-ear pressure became slightly positive. No magnitude dip was visible for positive middle-ear pressures.

The low-frequency vibration magnitudes at negative middle-ear pressures on the pars tensa were higher than those on the manubrium. R1 was not visible for large negative middle-ear pressures on the pars tensa. R2 appeared as a multi-peak feature on the pars tensa as well, and a higher-frequency branch on the posterior pars tensa appeared as a trough on the anterior pars tensa. The magnitude dip was not present on the pars tensa. The largest overall magnitude was recorded at the R2 peak on the posterior pars tensa.

The results of this study expand on the findings of the step-wise pressurization experiments and provide further insight into the evolution of the vibration response of the eardrum under quasi-static pressures.

## 4.1 Introduction

Tympanometry provides a fast, objective and noninvasive measurement of the acoustic input admittance (and related quantities) of the external and middle ear in the presence of quasi-static pressures. In a tympanometer, a probe tip in the ear canal combines a speaker that introduces an acoustic signal, a microphone that records the sound pressure, and a pump that provides the quasi-static pressure sweeps. Clinical tympanometers typically use a low-frequency pure-tone acoustic signal (around 220 Hz), with pump speeds of somewhere between 2000 and 4000 Pa/s and pressures swept in one or both directions between 0 Pa and ±2000 to 4000 Pa. In early work, Lidén et al. (1970) assessed tympanometry for detecting ossicular-chain disruption by collecting tympanograms of healthy subjects as well as those with conductive and sensorineural hearing loss. They noted several changes in the admittance due to abnormalities in the middle ear and suggested using 800 Hz as a probe-tone frequency for better sensitivity to abnormalities. Creten and Van Camp (1974) measured the admittance at 220 and 660 Hz at various pressurization rates, and found that the most accurate measure was achieved at very low rates (about 10 Pa/s). They also observed the different tympanogram shapes that occur at 660 Hz for normal ears. Their group later concluded that tracking the tympanometric peak pressure (TPP, the pressure at which the admittance magnitude is maximal) in a single sweep did not provide an accurate assessment of the middle-ear pressure. and suggested averaging the TPPs of sweeps in opposite directions (Decraemer et al., 1984). Therkildsen & Gaihede (2005) compared clinical tympanometers and found that higher pressurization rates did not affect TPP and attributed the observed small differences to differences in the direction of the static pressure sweep. More recently, wide-band tympanometry (admittance measurements over a range of frequencies instead of a single pure tone) has been used to identify patients with otosclerosis (Shahnaz et al., 2009), Eustachian tube dysfunction (Aithal et al., 2019) and Ménière's disease (Tanno et al., 2020), among other conditions.

There have been a number of studies that tried to provide more insight by studying the movements of the eardrum and ossicles under static pressures in human temporal bones. For example, Hüttenbrink (1988) performed extensive measurements for various conditions such as fixing the incudomallear joint and simulating the activation of the middle-ear muscles. He observed a complex 3D movement of the stapes during static pressurization of the middle ear. He

also saw that the effect of muscle activation diminished as the static pressure on the eardrum became larger. Among other things, he concluded that ‘gliding’ movements in the incudomallear and incudostapedial joints are important; and that the middle-ear muscles are incapable of counterbalancing large static pressures but that the sheath of the tensor-tympani tendon provides a strong support. Dirckx and Decraemer (1991) recorded the shape of the eardrum while pressurizing the middle ear and concluded that the effects of positive and negative pressures were significantly different, and that the displacement of the malleus could not be modelled as undergoing a simple fixed-axis rotation at higher static pressures. Murakami et al. (1997) measured the vibration magnitudes of the umbo and the stapes with a tympanometer probe placed in the Eustachian tube to pressurize the middle ear. They saw that, for both positive and negative middle-ear pressures, the low-frequency vibration magnitudes decreased as the pressure was increased, and the frequency-response peaks shifted to higher frequencies. The displacements at higher frequencies increased as the pressure was increased. Gan et al. (2006) measured the effects of static pressure (and also of middle-ear fluid) and reported the displacements at the umbo and the stapes footplate. They found that increasing middle-ear pressures up to about +2000 Pa reduced vibration magnitudes uniformly up to 1.5 kHz but had less effect for higher frequencies. For negative middle-ear pressures the umbo vibration magnitude decreased up to 1.5 kHz, but increased for higher frequencies. They also found that the cochlea had its greatest effect on the eardrum vibrations at 4 kHz. Homma et al. (2010) measured the effects of static pressures on bone conduction as well as air conduction, and found that the bone-conduction resonance also shifted to higher frequencies in the presence of static pressures. Warnholtz et al. (2021) experimentally reduced the flexibility of the incudomallear joint and measured the effects on sound transmission in the presence of static pressures. They concluded that the flexible joint allows better sound transmission in the presence of static pressures.

The effects of static pressures on admittance during tympanometry are not well understood, especially for infants (e.g., Myers et al., 2019), and animal models for the vibration response of the eardrum under tympanometry-like pressure sweeps can help provide insight by allowing for extensive in-vivo measurements that are not possible in humans. For example, von Unge et al. recorded in-vivo admittance (1991) and also post-mortem eardrum shape (1993) in gerbils using a series of pressure steps in the ear canal. They noted that disrupting the ossicular chain increased

the admittance, while fixation reduced it. They also compared tympanograms at 220 and 660 Hz and described the emergence of multiple peaks at the higher frequency. Lee and Rosowski (2001) measured in-vivo vibration responses at the umbo and on the pars flaccida in gerbils with pressure steps in the middle ear. They confirmed the existence of the asymmetry observed in previous studies in gerbils, with the largest admittance changes occurring for negative middle-ear pressures. They also identified the existence of a multiple-peak tympanogram when the frequency was increased to 1 kHz or higher.

Other species have been used in addition to the gerbil. Ladak et al. (2004) measured the shape of the cat eardrum under middle-ear pressure steps. They observed that an immobilized malleus produced a more symmetric response to static pressures than a mobile malleus did. Wang et al. (2017) measured in-vivo chinchilla eardrum surface vibrations and recorded the changes due to the release of a built-up middle-ear pressure of around 1400 Pa. They observed a magnitude increase in all quadrants of the eardrum up to 2 kHz, at which frequency all of the eardrum was vibrating in phase, with the largest amplitude in the posterior pars tensa. For higher frequencies, the vibration magnitude stayed approximately constant after the release of the middle-ear pressure. Salih et al. (2016) measured rabbit ears post mortem to quantify the non-linearity in the middle ear due to harmonic quasi-static pressures. They found that the harmonic distortion was less than 10% for pressures less than 100 Pa, but the distortion increased rapidly when the pressure was increased to 1000 Pa. The harmonic distortion also increased as the frequency of the sinusoidal quasi-static pressure was increased.

In a recent paper (Kose et al., 2020) we presented in-vivo gerbil vibration responses on the pars tensa, pars flaccida and manubrium under a step-wise middle-ear pressurization protocol for 11 gerbils. We illustrated shifts of the vibration peaks, both in frequency and magnitude, and studied their behaviour throughout the pressurization cycle. We described the first two peaks that were present at similar frequencies on the pars tensa, pars flaccida and manubrium; these peaks changed rapidly for small pressures. After the second peak, other closely spaced peaks specific to each region were also discussed.

In order to be more relevant to tympanometry, the mechanics of the middle ear should be investigated with pressure sweeps rather than steps. Dirckx et al. (2006) measured the displacement of the rabbit umbo and stapes under quasi-static pressure sweeps in the ear canal.

For pressurization rates lower than 1000 Pa/s, they observed a significant change in the pressure at peak displacement. They also saw more hysteresis at the umbo than on the stapes. They suggested that lower pressurization rates could provide additional clinical information about friction in the ossicular chain.

Since the admittance of the middle ear is highly dependent on the vibration of the eardrum, measuring vibrations at multiple points on the eardrum is essential for understanding the admittance measured in tympanometry. In this study we present multi-point in-vivo gerbil eardrum vibration responses to pressure sweeps. The vibration magnitudes at two points on the manubrium and two points on the pars tensa are shown as functions of both frequency and middle-ear pressure, and the evolution of the magnitudes and frequencies of the peaks and troughs are explored in detail.

## 4.2 Materials & methods

This study has been reviewed by the Institutional Review Board of the McGill University Health Centre Research Institute (protocol number 2011-5201). Male Mongolian gerbils (*Meriones unguiculatus*) were used, with body weights ranging from 50 to 100 g (Charles River Laboratories, St-Constant, QC). Of the eight most recent gerbils, we present results for the six who survived until the end of the experiment with good middle-ear pressurization. The anaesthetic regimen and the surgical process were almost identical to those that we used previously (Kose et al., 2020). Pentobarbital was administered intraperitoneally to ensure proper anaesthesia throughout the experiment (for induction, 35 mg/kg if the animal was less than 6 months old, or 50 mg/kg if 6 months old or older; for maintenance, half of the induction dose every 30 minutes or when needed). The xylazine doses that we used previously were omitted due to issues with slow induction and inconsistent levels of anaesthesia.

After an incision between the jaw and the shoulder, the bulla was exposed starting posteriorly and moving clockwise, and then the ear canal was removed down to the bony meatus. A small hole was created in the bulla to allow access to the middle ear for pressurization. A 3D-printed acoustic coupler was attached to the ear canal with dental cement to provide an enclosed access to the eardrum. A glass window, coated to be anti-reflective around the frequency of the measurement laser, allowed access for the laser beam to focus on the glass-coated beads on the

eardrum. A bead was placed at the umbo, and another one roughly at the middle of the manubrium. One bead was placed on the posterior pars tensa and one on the anterior pars tensa, between the mid-manubrium and the annulus. These four bead locations were the same as reported in our previous paper.

The pressurization system consisted of a peristaltic pump controlled by a microcontroller (Arduino Uno, SmartProjects, Strambino, Italy) which pressurized the middle ear via a small hole in the bulla. The system was the same as in Kose et al. (2020) except for the addition of a larger and adjustable buffer volume to provide a low pressurization rate during pressure sweeps. The static pressure was varied over a range of ±2500 Pa. A full pressurization cycle included decreasing continuously from 0 Pa to −2500 Pa, increasing back to 0 Pa, increasing to +2500 Pa, and decreasing back to 0 Pa. The full pressure-cycle period was adjusted to be 210±5 s, to match the length of one cycle of our previous step-wise pressurization protocol. As in our previous study, and in contrast to clinical tympanometric practice, the static pressure was applied in the middle-ear cavity and not in the ear canal. The pressure values here are reported in terms of the actual middle-ear pressure. The pressure sensor was accurate to within 12 Pa.

The vibrational velocities of beads on the manubrium and the pars tensa were measured using a laser Dopper vibrometer (LDV) (HLV-100, Polytec, Irvine, CA) and were recorded using Polytec's VibSoft software (Version 5.5). Both the sound pressure and the vibration velocity as functions of time throughout the pressurization cycle were stored in files with a unique identifier for each cycle, and a MATLAB script used their timestamps and identifiers to synchronize the measurements. A Python script (running on the same computer that managed the VibSoft output under Microsoft Windows 10) transmitted the target pressure extremes (±2500 Pa) and the target pressurization speed to the Arduino microcontroller. After recording, the vibration velocities during each individual acoustic chirp (linear frequency sweep from 0.2 to 10 kHz) were integrated to obtain displacements and then converted to the frequency domain using a Fast Fourier Transform. The vibration displacement magnitudes (normalized by the sound pressure) were then plotted using a MATLAB script for all of the figures in the next section.

All measurements were recorded in a sound-isolation chamber where the animal and the microscope were placed on an anti-vibration pad on a table. The noise floor was recorded by focusing the vibrometer on the inside wall of the acoustic coupler at the beginning of each

experiment. For the range of frequencies considered here, the measured magnitudes were at least an order of magnitude larger than the noise floor.

At the beginning of each experiment, at least three consecutive pressurization cycles at the bead on the umbo were recorded. After three or more cycles at each of one or more of the other beads had been recorded, one or more final cycles were recorded at the umbo before sacrifice of the gerbil (pentobarbital overdose followed by pneumothorax). Figure 4.1 shows an example of the middle-ear pressure (black line) and the resulting umbo vibration magnitude (red line) at a single frequency (1.0 kHz) as a function of time throughout one pressurization cycle. The pressure signal consistently showed a slower linear loading phase (equivalent to a rate of 40 Pa/sec), and a faster nonlinear unloading phase (starting at a rate of ~70 Pa/sec and slowing to ~50 Pa/sec near 0 Pa). In order to display the vibration responses as functions of pressure in the spectrogram figures of the Results section, each chirp was matched to the static pressure at the corresponding time.

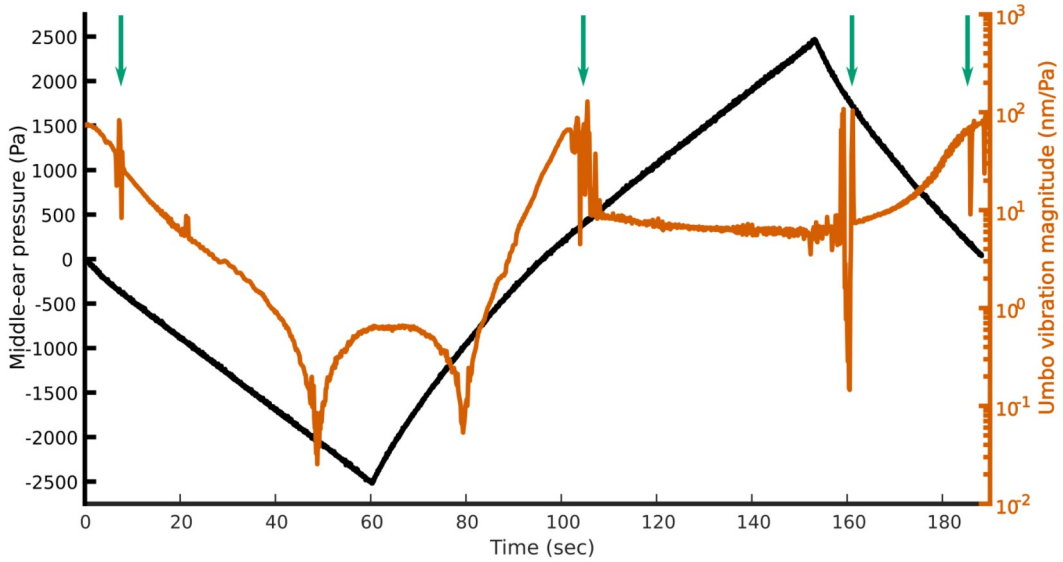


*Figure 4.1: Middle-ear pressure (black) and corresponding vibration response (red) at 1.0 kHz for gerbil G47 at the umbo, for a single cycle. Green arrows indicate the laser beam adjustments.*

The laser was manually aimed at the target bead at the beginning of each cycle, and re-aimed throughout the cycle when needed (e.g., when the bead moved outside the laser beam's diameter of ~35 μm). Especially near ambient pressure, the bead displacements were large in response to

the quasi-static pressure change and the time required for the manual re-aiming sometimes resulted in an artifact due to a brief loss of the signal (as at $t$≈7 s and $t$≈105 s in Figure 1). In this particular measurement, the bead was also re-aimed near the highest positive pressure to ensure good signal strength (at $t$≈160 s).

As discussed in the previous paper, when the middle-ear pressure was made more negative, the low-frequency vibration magnitude decreased. At $t$≈48 s in the loading phase and $t$≈78 s in the unloading phase, there is a magnitude dip as the vibration magnitude becomes larger for more negative pressures. This phenomenon will be discussed further in the following sections.

## 4.3 Results

### 4.3.1 Inter-specimen variability

Figure 4.2 compares the inter-specimen variability of the unpressurized umbo responses of the 6 gerbils of this study with the responses of the 12 gerbils in Maftoon et al (2013) (blue shading) and the 11 gerbils in our previous paper (Kose et al., 2020) (red shading). The low-frequency magnitude (at 0.5 kHz) varied between 40 and 80 nm/Pa for our 6 gerbils while Maftoon et al. recorded between 30 and 100 nm/Pa and we previously recorded between 25 and 85 nm/Pa. The vibration magnitude increased as the frequency increased, up to a broad peak (referred to here as R1, as in our previous paper) between 1.5 and 2.5 kHz, very similar in peak frequency and magnitude to what was shown in our previous paper. After the peak, the vibration magnitude decreased irregularly. The vibration magnitudes and the frequencies of the peaks were mostly within the ranges of those in our previous paper, with some small exceptions at higher frequencies.

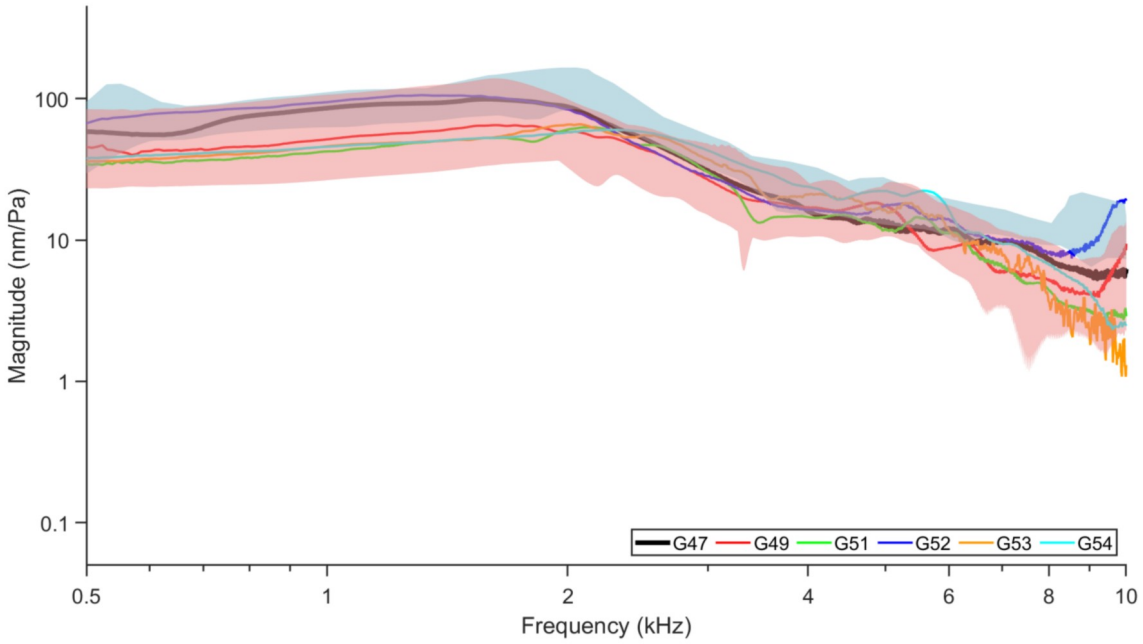


*Figure 4.2: Unpressurized vibration responses at the umbo for all 6 gerbils. Red and blue shaded areas are the vibration magnitude ranges for the 11 gerbils reported in Kose et al. (2020) and the 12 gerbils reported in Maftoon et al. (2013), respectively.*

For the following sections, gerbil G47 was chosen to show the vibration responses at various measurement locations because it was typical and it had the least noise and the fewest tracking artifacts.

### 4.3.2 Manubrial response

In order to compare the present pressure-sweep responses with the pressure-step responses from our previous paper, vibration frequency responses have been sampled at roughly 500-Pa intervals throughout the pressurization cycle. Figure 3 displays these sampled umbo vibration magnitudes for the negative-pressure half-cycle (left panel) and the positive-pressure half-cycle (right panel), in the same format as for Figure 8 of our previous paper. At 0 Pa (solid black), the vibration magnitude increases from 35 nm/Pa at 0.5 kHz to a broad peak (R1, filled circular marker). After R1, the magnitude decreases until a hint of a peak (R2, as in the previous paper, filled square marker). For higher frequencies, the vibration magnitude decreases more or less monotonically with multiple small peaks and troughs, to 5.6 nm/Pa at 10 kHz. Both peaks are difficult to discern in this pressure cycle but they were clearer in other cycles. The vibration

magnitudes at 0.5 kHz decrease as the pressure is made more negative, to 6 nm/Pa at −500 Pa and to 1.8 nm/Pa at −1000 Pa, while the slope between 0.5 kHz and R1 becomes flatter; beyond R1, the vibration magnitude decreases slightly before rising to R2. At −1500 Pa, the low-frequency vibration magnitude decreases to a very low value (around 0.09 nm/Pa) before rising slightly to R1; after R1 the vibration magnitude decreases again and then rises sharply to R2. When the pressure is reduced to −2000 and −2500 Pa, the vibration magnitude stays more or less the same at 0.5 kHz but then, instead of decreasing sharply with increasing frequency, it increases gradually until R1 and then decreases slightly before rising to R2. This decrease in the mid-frequency magnitudes, from about 0.5 kHz to 6 kHz, and for pressures between about −1000 Pa and −2000 Pa, was also observed in our previous paper, where it was described as a magnitude 'dip'.

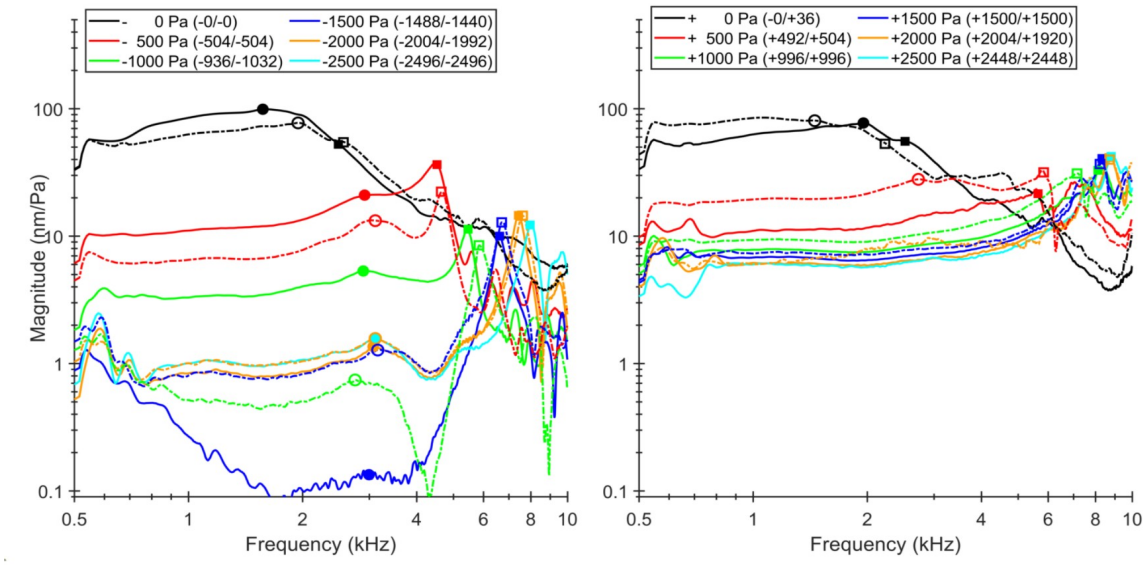


*Figure 4.3: Vibration response of G47 at the umbo for negative-pressure half-cycle (left) and positive-pressure half-cycle (right). Solid curves = loading phase, dashed = unloading phase. Circles (R1) and squares (R2) show the locations of the resonances in the loading (filled symbols) and unloading (empty symbols) phases. (Actual pressure values are given in parentheses for both loading and unloading phases.)*

At 0 Pa, R1 and R2 start as shallow peaks at 1.5 and 2.6 kHz with peak magnitudes of 100 nm/Pa and 54 nm/Pa, respectively. As the pressure becomes negative, both R1 and R2 rapidly shift to higher frequencies while their peak magnitudes decrease, reaching 2.8 and 4.5 kHz with peak magnitudes of 18 and 36 nm/Pa, respectively, at −500 Pa. As the pressure

becomes more negative, R1 and R2 slowly shift further, reaching 3.0 and 6.8 kHz, respectively, at −1500 Pa. The R1 magnitude also shows a dip at −1500 Pa, decreasing to 0.12 nm/Pa. after which it recovers to 1.2 nm/Pa at −2500 Pa while shifting slightly to 3.1 kHz. The R2 peak magnitude, on the other hand, stays more or less constant around 9.2 nm/Pa at 7.8 kHz.

In the unloading phase of the negative-pressure half-cycle, the vibration magnitude is lower than or similar to the loading phase. As the pressure is increased, the low-frequency magnitudes between 0.5 kHz and R1, and those between R1 and R2, start to decrease. The magnitude is lowest around −1000 Pa, similar to what is seen at −1500 Pa in the loading phase. After the dip, the vibration magnitudes for frequencies up to R2 recover rapidly but remain slightly less than in the loading phase.

The pattern is much simpler in the positive-pressure half-cycle. The low-frequency vibration magnitudes decrease monotonically when the pressure is increased, with very little change beyond +2000 Pa. R1 disappears for positive pressures in the loading phase while R2 shifts rapidly from 2.7 kHz at 0 Pa to 7.7 kHz at +1000 Pa, and then more slowly to 8.7 kHz at +2500 Pa. When the pressure is reduced back to zero, the vibration magnitude increases to higher values than it had during the loading phase. R1 reappears as a shallow peak at 2.7 kHz and +500 Pa before shifting back to 1.4 kHz at 0 Pa, and R2 shifts back to an almost-buried peak at about 2.2 kHz at 0 Pa, both frequencies being very close to what was seen at the beginning of the negative-pressure half-cycle.

The overall trends here are very similar to what was seen with the step-wise pressurization protocol in our previous paper. For both negative-pressure and positive-pressure half-cycles, the low-frequency vibration magnitudes and the R1 and R2 frequencies and magnitudes in different pressurization cycles and in other gerbils were within the ranges of the ones in Kose et al. (2020).

To illustrate the continuous frequency-response evolution throughout the pressurization-sweep cycle, Figure 4 shows a spectrogram of the vibration magnitude at the umbo for G47 (the same data as shown in Figure 3). The horizontal axis is the quasi-static middle-ear pressure while the vertical axis is the frequency on a linear scale. Both R1 and R2 were traced where they were visible. Between 0 Pa and −300 Pa, both R1 (thick red line) and R2 (medium red line) are difficult to discern. After −400 Pa, R1 becomes faintly visible at about 2.7 kHz as a slight

rightward convexity of the isomagnitude contours, and it then rises slowly to about 3.1 kHz at −2500 Pa. R2, on the other hand, appears as a sharp peak at 4 kHz by about −200 Pa and shifts rapidly to 7.8 kHz at −2500 Pa. Multiple higher-frequency peaks and troughs start to appear between 0 and −300 Pa, shifting rapidly to higher frequencies. The peak with the lowest frequency after R2 can be tracked throughout the cycle (thin red line), but peaks at higher frequencies shift beyond 10 kHz as the pressure becomes more negative.

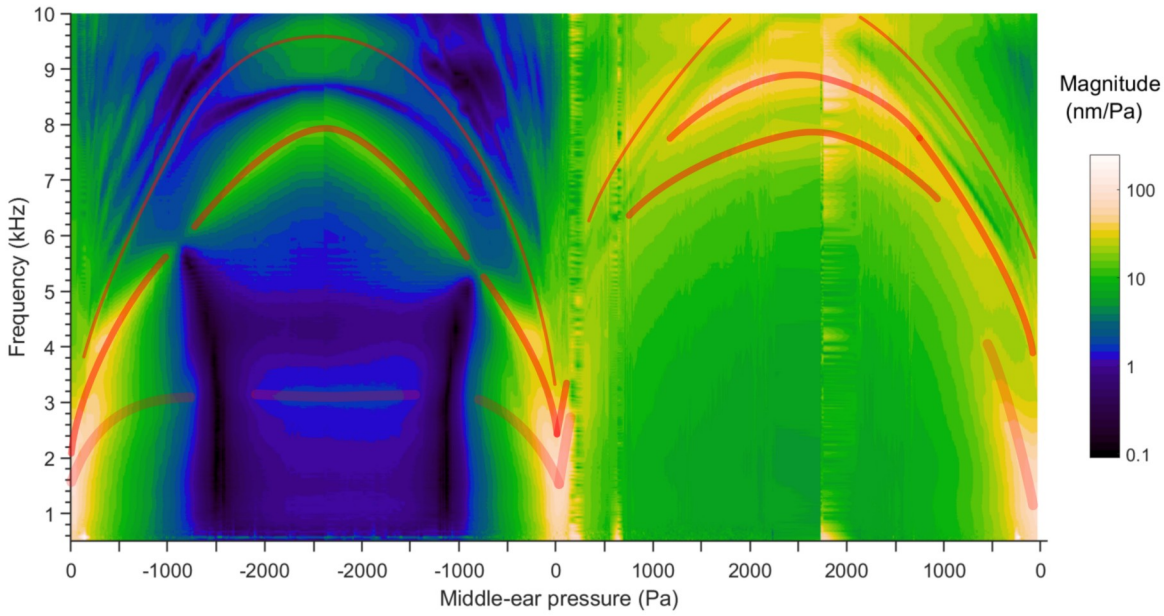


*Figure 4.4: Vibration response of G47 at the umbo over the pressurization cycle as a spectrogram. The vertical axis shows the frequency on a linear scale. The trajectories of R1 (thick red lines), R2 and its branches (medium red lines) and higher-frequency peaks (thin red lines) are highlighted.*

When the pressure is decreased from zero to about −1100 Pa, the magnitude dip (described above) appears at about 5.9 kHz, near R2. The dip very rapidly shifts to 3.6 kHz at −1250 Pa, its range broadening until it extends from 0.5 to 5.1 kHz at −1400 Pa. The magnitude at the centre of this dip is about 0.2 nm/Pa. After being effectively buried in the dip, R1 reappears as a broad peak at about 3 kHz as the pressure drops to about −1700 Pa, reaching a magnitude of about 1 nm/Pa at −2500 Pa. The R2 magnitude also rapidly recovers after the dip, to 5.5 nm/Pa at −1300 Pa, and it continues to increase to 11 nm/Pa at 8.0 kHz by −2500 Pa. When the pressure is increased from −2500 Pa back to 0 Pa, the behaviour of the peaks is approximately the reverse of

what happened in the loading phase, with a slight asymmetry. The magnitude dip occurs between about −1200 and −900 Pa in the unloading phase.

In the positive-pressure half-cycle, the vibration magnitudes are seen to change much less than in the negative-pressure half-cycle, as also seen in Figure 3. The R1 peak rapidly shifts to 2.8 kHz with a peak magnitude of 20 nm/Pa at +350 Pa (it is partially hidden due to the artifact between +150 and +300 Pa) before disappearing for more positive pressures. The R2 frequency rapidly shifts from 0 Pa to +200 Pa, and then is seen with two separate branches; first one appears at 6.5 kHz at +700 Pa, and the second one appears at 7.7 kHz at +1200 Pa. Both shift further as the pressure reaches +2500 Pa, to 7.8 kHz and 8.8 kHz, respectively. After a sharp trough that follows a trajectory similar to that of the second branch of R2, another substantial peak (thin red line) also shifts to higher frequencies as the pressure is increased. In the unloading phase, the two branches of R2 converge at about 6.9 kHz at +1300 Pa, before shifting back to lower frequencies. R1 reappears at 4 kHz at +500 Pa, and shifts to lower frequencies when the pressure is reduced back to 0 Pa.

Figure 5 shows a collage of the spectrograms for all six gerbils. The features described for G47 are all also seen for the other gerbils, with some quantitative differences. All of the gerbils display a magnitude dip in the negative-pressure half-cycle, but there are some qualitative differences. For G49 the dip is divided by R1 (around 4 kHz), while the magnitude dip for G51 has 2 splits, being divided by R1 (around 3.5 kHz) and by a trough after R1 (around 4.2 kHz). The magnitude dip for G50 occurs for even higher frequencies than R2 (around 7 kHz in the loading phase). The magnitude dip in G49 occurs at a more negative pressure, and the vibration magnitude does not recover much at −2500 Pa. The splitting of R2 in the positive-pressure half-cycle is present in all of the gerbils, with some differences in the pressure and frequency at which they converge again.

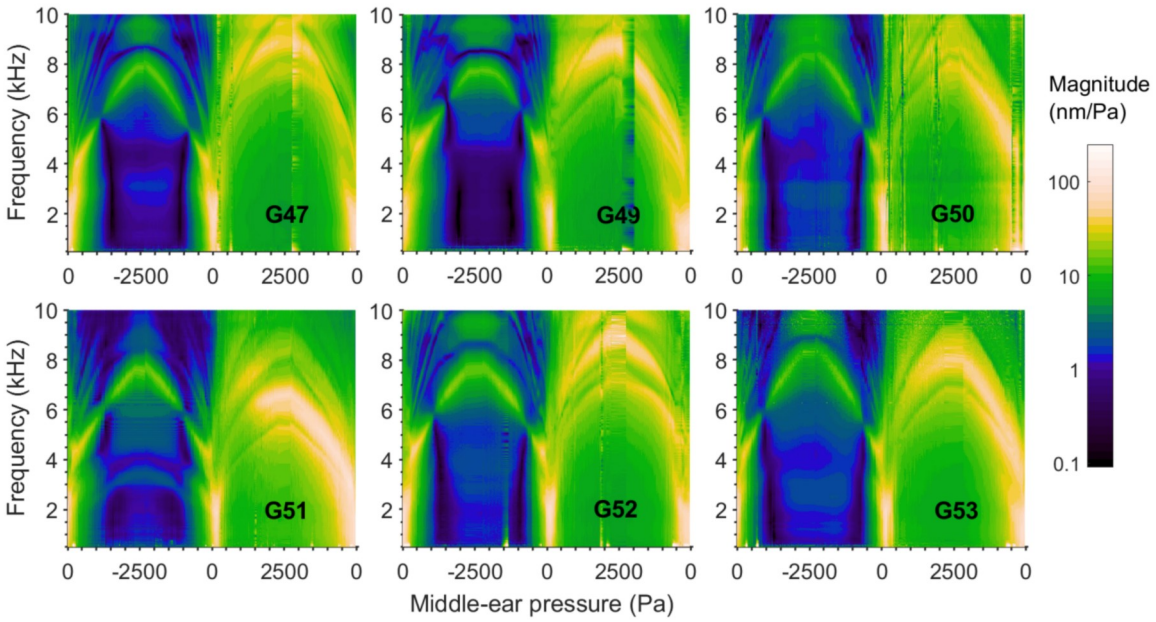


*Figure 4.5: Vibration response of all 6 gerbils at the umbo over the pressurization cycle as a spectrogram. The vertical axis shows the frequency on a linear scale.*

Figure 6 shows another way of looking at the same data, with the vibration responses at several individual frequencies, from 0.5 to 10 kHz, shown as functions of the static pressure. Black lines indicate the loading phases while the red lines indicate the unloading phases. The green boxes show the locations of the R2 peaks in each half-cycle at each frequency. The vertical and horizontal dashed lines help locate the ambient pressure and the vibration magnitude at −2500 Pa, respectively. At 0.5 kHz the vibration magnitude is quite noisy. The largest magnitude occurs at 0 Pa and the smallest magnitudes occur at the ends of the sweeps (±2500 Pa). As described for Figures 3 and 4, the magnitude decreases more in the negative-pressure half-cycle than in the positive-pressure half-cycle. From 1 to 5 kHz, magnitude dips are clearly visible in the negative-pressure half-cycle. From 1 kHz to about 2 kHz, the largest magnitude occurs at 0 Pa. At higher frequencies the magnitudes at −200 Pa and at +150 Pa become larger than the magnitude at 0 Pa. At 3 kHz (not shown), the largest magnitudes correspond to R2, at −250 Pa and at +250 Pa. At 4 and 5 kHz, the R2 peaks in both the negative-pressure and positive-pressure half-cycles have similar magnitudes. At 6 kHz, the magnitude dip is no longer visible, and the largest magnitude occurs at +600 Pa instead of in the negative-pressure half-cycle. At 8 and 10 kHz, there is a broad magnitude dip in the negative-pressure half-cycle between −600 Pa and

−2000 Pa. The largest magnitude at 10 kHz corresponds to the higher-frequency peak (thin red line in Figure 4), at +2000 Pa.

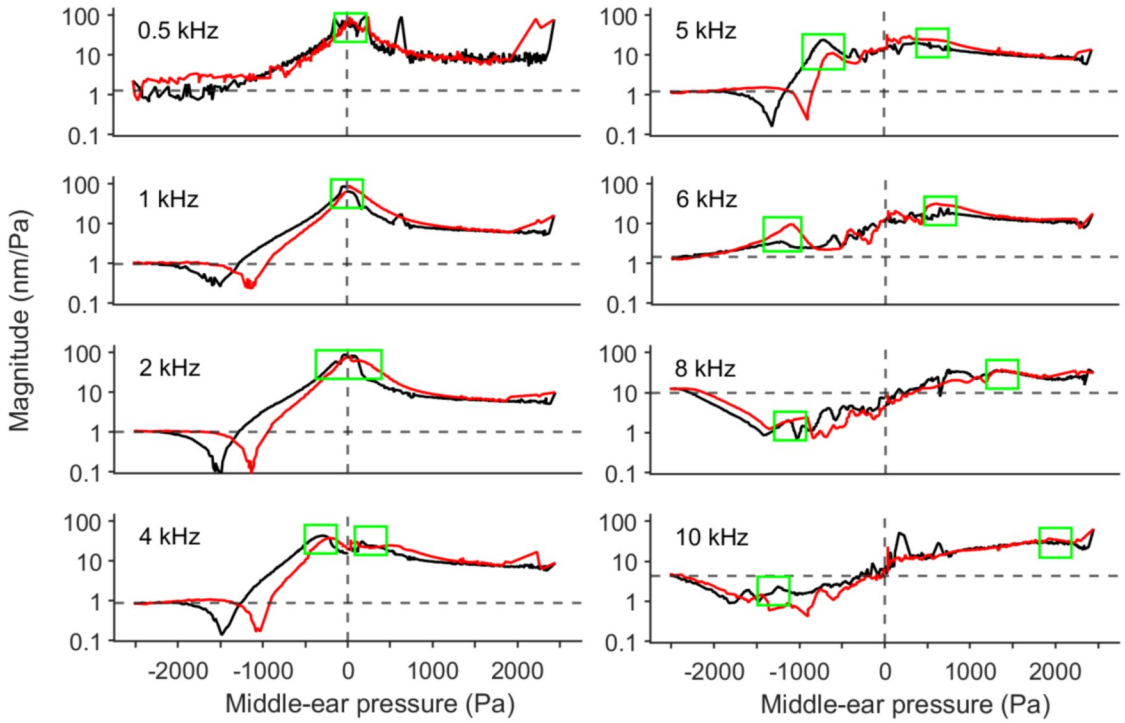


*Figure 4.6: Vibration responses of G47 at the umbo as functions of the middle-ear pressure, at several frequencies. Green boxes show the locations of the highest magnitude (at 0.5, 1 and 2 kHz) or of R2 (for frequencies>2 kHz).*

The vibration responses at mid-manubrium were very similar to the ones at the umbo. For each gerbil, the frequencies of R2 and of the higher-frequency peaks were within 0.5 kHz of the ones at the umbo in the negative-pressure half-cycle, and within 0.8 kHz in the positive-pressure half-cycle. The low-frequency magnitude dip occurred at more negative pressures (from −1800 to −2200 Pa) than at the umbo.

### 4.3.3 Pars-tensa response

Figure 7 shows a spectrogram for the vibration response on the posterior pars tensa for the same gerbil as in Figure 4 (G47). Due to larger displacements of the pars tensa in response to the static pressure, more readjustments of the laser beam were necessary than for the umbo, resulting in more artifacts in the vibration response (such as from 0 to −600 Pa, from −2200 to −2400 Pa,

between the negative-pressure and positive-pressure half-cycles, etc.). As observed in our previous paper, the vibration responses on the pars tensa are similar overall to those at the umbo but with some key differences: the overall vibration magnitudes are larger; the magnitude dip in the negative-pressure half-cycle is absent for both pars-tensa points; and R1 disappears rapidly for large pressures, both negative and positive. The low-frequency magnitude on the posterior pars tensa (at 0.5 kHz) slowly decreases from 15 nm/Pa at −600 Pa to 1.8 nm/Pa as the pressure is reduced to −2500 Pa. Although hard to distinguish due to artifacts, R1 (thick red line) is an almost buried peak at 1.4 kHz (confirmed in other pressurization cycles at the same location in this ear) at 0 Pa, and shifts to 2.1 kHz at −400 Pa before disappearing for more negative pressures. The behaviour of R2 (medium red line) is similar to that seen at the umbo, shifting from 2.6 kHz at 0 Pa (peak magnitude 110 nm/Pa) to 3.8 kHz at −500 Pa (peak magnitude 100 nm/Pa), and then to 7.8 kHz at −2500 Pa (peak magnitude 39 nm/Pa). At about −300 Pa a cluster of peaks separates from R2, extending from 4.5 kHz to 6.8 kHz. (They are obscured due to the tracking artifact here, but they are confirmed by other cycles). The peak with the lowest frequency within the cluster (denoted by the thin red line) shifts more slowly than the others, reaching 8.8 kHz at −2500 Pa with a magnitude of 40 nm/Pa. This peak has about the same frequency as the trough between R2 and the thin red line in Figure 4. As the pressure is increased back to zero, the low-frequency magnitude increases, reaching 61 nm/Pa at 0 Pa, and all of the peaks shift back to lower frequencies.

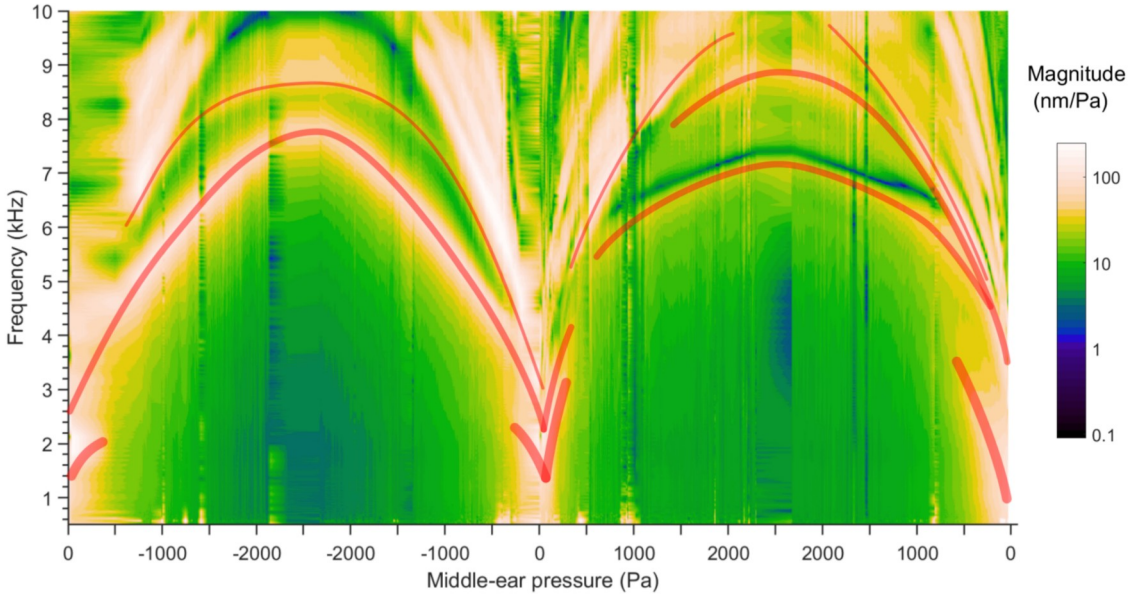


*Figure 4.7: Vibration response of G47 on the posterior pars tensa over the pressurization cycle as a spectrogram. The vertical axis shows the frequency on a linear scale. The trajectories of R1 (thick red lines), R2 and its branches (medium red lines) and higher frequency peaks (thin red lines) are highlighted.*

In the positive-pressure half-cycle, the low-frequency magnitude drops from 61 nm/Pa at 0 Pa to 3.3 nm/Pa at +2500 Pa. R1 shifts to 3.1 kHz at +300 Pa and is not visible when the pressure is increased further. R2 and the cluster of peaks quickly diverge and shift to higher frequencies until +450 Pa where R2 reaches 4.1 kHz with a peak magnitude of 30 nm/Pa. R2 reaches 7.1 kHz at +2500 Pa with a peak magnitude of 1.5 nm/Pa, while the second branch reaches 8.9 kHz with a peak magnitude of 30 nm/Pa. The highest-frequency peak of the cluster reaches 9.9 kHz at +2000 Pa. A minimum lies between the two lowest-frequency branches of R2. This minimum reaches 7.3 kHz at +2500 Pa, and stays about 0.1 to 0.3 kHz higher in frequency than the first branch of R2. When the pressure is reduced back to 0 Pa, the low-frequency vibration magnitude increases back to 90 nm/Pa, while R1 becomes visible at +500 Pa around 3.5 kHz and shifts back to 1 kHz at 0 Pa. R2 shifts back to 4.4 kHz at +300 Pa, where it joins the cluster of peaks and shifts back to 3.6 kHz with a peak magnitude of 181 nm/Pa. The trough between the clusters disappears at about 6.3 kHz at +700 Pa.

The anterior pars-tensa response for the same gerbil was very similar to that of the posterior pars tensa. The R2 frequency in the negative-pressure half-cycle was within 0.5 kHz of that for

the posterior pars tensa (as well as those of the umbo and mid-manubrium). The sharp peak that diverged from the cluster of peaks on the posterior pars tensa in the negative-pressure half-cycle was replaced by a sharp minimum on the anterior pars tensa. On the other hand, the sharp trough that followed the lowest-frequency branch of R2 on the posterior pars tensa in the positive-pressure half-cycle was replaced by a sharp peak on the anterior pars tensa. The low-frequency magnitudes for both pars-tensa points were similar to each other throughout the pressure cycle.

In other gerbils the pars-tensa responses were very similar to what is described here for G47 except that in G46 and G52 even the cluster peak with the lowest frequency shifted rapidly to higher frequencies on both the anterior and posterior pars tensa as the pressure was made more negative; and in some G50 and G52 the sharp minimum on the anterior pars tensa (which appeared in the place of the sharp peak in the posterior pars tensa) also split for pressures lower than about −1500 Pa.

## 4.4 Discussion

In this paper we have expanded upon the findings of Kose et al. (2020), by observing the gradual changes in the vibration response under quasi-static pressure sweeps. The vibration magnitudes and peak frequencies found here with the sweeps were the same as those identified in the previous paper using steps, within the range of inter-specimen variability. This is consistent with the idea that the pressure sweep was slow enough to be similar to the series of steps in terms of viscoelastic effects (after the initial transient of the step subsides). With the sweeps, the rapid shifts of the peaks for small pressure changes (smaller than the 500-Pa steps of the previous paper) could be studied, as could the shifts of the numerous high-frequency features.

The pressurization rate was non-uniform but consistently so. The effect of this non-uniform rate was presumably small since the greatest rate change occurred at the beginnings of the unloading phases, near the extreme pressure values where the changes in displacement were smallest.

For both the manubrial and pars-tensa points, the dependence of the vibration magnitude on static pressure resembled a single-peak tympanogram at low frequencies (Figure 6, 0.5 kHz). However, as the frequency increased, more complex shapes were caused by the local peaks and troughs and by the dip at about −1500 Pa. Lee and Rosowski (2001) showed complex

displacement curves in gerbils at frequencies as low as 4 kHz, which is in line with our umbo response. The separate peaks in the negative-pressure and positive-pressure half-cycles (our Figure 6, at 4 and 5 kHz) coincide with our R2 peaks, and as the frequency is increased further they create more complex displacement curves.

Lee and Rosowski (2001) observed magnitude dips at negative middle-ear pressures between 1 kHz and 4 or 6 kHz, while in our experiments the dip was visible from 0.5 kHz up to 5 or 6 kHz. Their dip was visible around −2000 Pa when they swept the pressures from negative to positive, and around −1000 Pa when they swept from positive to negative. In our results the effect of the sweep direction was smaller, with the dip occurring around −1400 Pa for negative-to-positive sweeps and around −1100 Pa for positive-to-negative sweeps. They attributed the differences between the directions to viscoelastic effects in the middle ear. They also suggested that the behaviour for negative middle-ear pressures could be affected by the pars flaccida sticking to the head of the malleus. Feizollah (2019) observed a phenomenon that might be relevant to the magnitude dip: under quasi-static pressure sweeps, the displacements of the incudostapedial joint increased as the ear-canal pressure increased up to +1000 Pa and then decreased for more extreme pressures.

As described in our previous paper, the low-frequency peak (designated as R1) occurs at all of the measured locations, but with differences in the range of pressures where it is visible: on the manubrium it disappears at large positive middle-ear pressures but is still visible at negative pressures, while on the pars tensa it disappears at both positive and negative large pressures. It is not clear whether this might be related to the conclusion by Homma et al. (2010), based on a combination of experimental measurements and modelling, that for positive ear-canal pressures (or negative middle-ear pressures) the stiffening of the eardrum may be greater than that of the ligaments that act on the malleus, while for negative ear-canal pressures (or positive middle-ear pressures) their degrees of stiffening may be similar.

The largest peak (designated as R2) was visible on both the manubrium and the pars tensa. It seems to be a superposition of multiple resonances at small pressures, since at higher pressures it appears to split into multiple peaks on the pars tensa. The lowest-frequency branch of R2 on the posterior pars tensa appears to correspond in frequency to a trough on the anterior pars tensa. This is consistent with previous studies that have shown peaks at high frequencies that are local

to specific regions of the pars tensa and are out of phase with vibrations in other regions (e.g., Decraemer et al., 1997 in cat; as cited by Fay et al., 2006; Cheng et al., 2013 in human; Maftoon et al., 2013 in gerbil).

The observations of the gradual changes of vibration magnitudes in response to slow pressure sweeps provide insight into the mechanoacoustical response of the middle ear under tympanometric pressures. The mechanisms underlying the evolution of the peaks and the presence of the magnitude dip could be explored with a computational model validated using the present experimental data. To be more closely related to tympanometry, however, the effects of pressurization rates closer to those of clinical tympanometers should be investigated experimentally.

## Acknowledgements

The authors would like to thank Dr. Aurore Dodelet-Devillers of the McGill University Health Centre Research Institute Vivarium, for her help with the handling of the animals, anaesthesia, and surgical procedures, and the rest of the Vivarium staff for their help in maintaining and advising on the health and comfort of the animals. We also thank Dr. Ross Wagner for his help in the development of the acoustic coupler and the experimental setup, and Mr. Sajjad Feizollah for his help with the surgical procedure and the development of the pressure control for the sweep. This work was supported in part by the Canadian Institutes of Health Research, the Natural Sciences and Engineering Research Council (Canada), the Fonds de recherche en santé du Québec, the Montréal Children’s Hospital Research Institute, and the McGill University Health Centre Research Institute.

## Conflict-of-interest disclosure statement

The authors declare that they have no conflicts of interest

## References


Aithal, S., Aithal, V., Kei, J., Anderson, S., & Liebenberg, S. (2019). Eustachian tube dysfunction and wideband absorbance measurements at tympanometric peak pressure and 0 daPa. J Am Acad Audiol, 30(9), 781–791.

Cheng, J. T., Hamade, M., Merchant, S. N., Rosowski, J. J., Harrington, E., & Furlong, C. (2013). Wave motion on the surface of the human tympanic membrane: Holographic measurement and modeling analysis. J Acoust Soc Am, 133(2), 918–937.

Creten, W. L., Heyning, P. H. V. de, & Van Camp, K. J. (1985). Immittance audiometry normative data at 220 and 660 Hz. Scandinavian Audiology, 14(3), 115–121. Taylor & Francis.

Creten, W. L., & Van Camp, K. J. (1974). Transient and quasi-static tympanometry. Scandinavian Audiology, 3(1), 39–42. Taylor & Francis.

Decraemer, W. F., Creten, W. L., & Van Camp, K. J. (1984). Tympanometric middle-ear pressure determination with two-component admittance meters. Scandinavian Audiology, 13(3), 165–172. Taylor & Francis.

Dirckx, J. J., & Decraemer, W. F. (1991). Human tympanic membrane deformation under static pressure. Hearing research, 51(1), 93–105.

Dirckx, J. J. J., Buytaert, J. A. N., & Decraemer, W. F., W. F. (2006). Quasi-static transfer function of the rabbit middle ear, measured with a heterodyne interferometer with high-resolution position decoder. JARO, 7(4), 339–351.

Dirckx, J. J. J., & Decraemer, W. F. (1992). Area change and volume displacement of the human tympanic membrane under static pressure. Hearing Research, 62(1), 99–104.

Feizollah, S. (2019). Microstructure and displacements of the gerbil incudostapedial joint under static pressures (M.Eng. thesis). Montreal, Canada: McGill University.

Gan, R. Z., Dai, C., & Wood, M. W. (2006). Laser interferometry measurements of middle ear fluid and pressure effects on sound transmission. The Journal of the Acoustical Society of America, 120(6), 3799–3810.

Homma, K., Shimizu, Y., Kim, N., Du, Y., & Puria, S. (2010). Effects of ear-canal pressurization on middle-ear bone- and air-conduction responses. Hearing Research, MEMRO 2009: Middle-Ear Science and Technology, 263(1), 204–215.

Hunter, L. L., Feeney, M. P., Lapsley Miller, J. A., Jeng, P. S., & Bohning, S. (2010). Wideband reflectance in newborns: Normative regions and relationship to hearing screening results. Ear Hear, 31(5), 599–610.

Hüttenbrink, K. B. (1988). The mechanics of the middle-ear at static air pressures: The role of the ossicular joints, the function of the middle-ear muscles and the behaviour of stapedial prostheses. Acta Oto-Laryngologica, 105(sup451), 1–35. Taylor & Francis.

Kose, O., Funnell, W. R. J., & Daniel, S. J. (2020). Vibration measurements of the gerbil eardrum under quasi-static pressure steps. JARO, 21(4), 287–302.

Ladak, H. M., Decraemer, W. F., Dirckx, J. J., & Funnell, W. R. J. (2004). Response of the cat eardrum to static pressures: mobile versus immobile malleus. The Journal of the Acoustical Society of America, 116(5), 3008–3021.

Lee, C.-Y., & Rosowski, J. J. (2001). Effects of middle-ear static pressure on pars tensa and pars flaccida of gerbil ears. Hearing Research, 153(1), 146–163.

Lidén, G., Peterson, J. L., & Björkman, G. (1970). Tympanometry. Archives of Otolaryngology, 92(3), 248–257.

Liu, Y.-W., Sanford, C. A., Ellison, J. C., Fitzpatrick, D. F., Gorga, M. P., & Keefe, D. H. (2008). Wideband absorbance tympanometry using pressure sweeps: System development and results on adults with normal hearing. The Journal of the Acoustical Society of America, 124(6), 3708–3719.

Maftoon, N., Funnell, W. R. J., Daniel, S. J., & Decraemer, W. F. (2013). Experimental study of vibrations of gerbil tympanic membrane with closed middle ear cavity. JARO, 14(4), 467–481.

Murakami, S., Gyo, K., & Goode, R. L. (1997). Effect of middle ear pressure change on middle ear mechanics. Acta Oto-Laryngologica, 117(3), 390–395. Taylor & Francis.

Muyshondt, P. G. G., & Dirckx, J. J. J. (2021). Structural stiffening in the human middle ear due to static pressure: Finite-element analysis of combined static and dynamic middle-ear behavior. Hearing Research, 400, 108116.

Myers, J., Joseph Kei, Sreedevi Aithal, Venkatesh Aithal, Driscoll Carlie, Khan Asaduzzaman, Alehandrea Manuel, Anjali Joseph, & Alicja N. Malicka. (2019). Diagnosing conductive dysfunction in infants using wideband acoustic immittance: Validation and development

of predictive models. Journal of Speech, Language, and Hearing Research, 62(9), 3607–3619. American Speech-Language-Hearing Association.

Okabe, M., & Ito, K. (2002). Color Universal Design (CUD) - How to make figures and presentations that are friendly to Colorblind people -. Retrieved February 14, 2022, from https://jfly.uni-koeln.de/color/#pallet

Prieve, B. A., Vander Werff, K. R., Preston, J. L., & Georgantas, L. (2013). Identification of conductive hearing loss in young infants using tympanometry and wideband reflectance. Ear and Hearing, 34(2), 168–178.

Salih, W. H. M., Soons, J. A. M., & Dirckx, J. J. J. (2016). 3D displacement of the middle ear ossicles in the quasi-static pressure regime using new X-ray stereoscopy technique. Hearing Research, MEMRO 2015 – Basic Science meets Clinical Otology, 340, 60–68.

Seidman, M. D., Standring, R. T., Ahsan, S., Marzo, S., Shohet, J., Lumley, C., & Verzal, K. (2013). Normative data of incus and stapes displacement during middle ear surgery using laser Doppler vibrometry. Otology & Neurotology, 34(9), 1719–1724.

Shahnaz, N., Longridge, N., & Bell, D. (2009). Wideband energy reflectance patterns in preoperative and post-operative otosclerotic ears. International Journal of Audiology, 48(5), 240–247. Taylor & Francis.

Tanno, G. A. Y., Santos, M. A. de O., Sanches, M. T. D., Durante, A. S., Almeida, K. de, Gameiro, M. S., Roque, N. M. C. de F., & Sousa Neto, O. M. de. (2020). Analysis of wideband tympanometry in Ménière's disease. Brazilian Journal of Otorhinolaryngology. Retrieved from http://www.sciencedirect.com/science/article/pii/S1808869420301014

Therkildsen, A. G., & Gaihede, M. (2005). Accuracy of tympanometric middle ear pressure determination: The role of direction and rate of pressure change with a fast, modern tympanometer. Otology & Neurotology, 26(2), 252–256.

von Unge, M., Decraemer, W. F., Bagger-Sjöbäck, D., & Dirckx, J. J. (1993). Displacement of the gerbil tympanic membrane under static pressure variations measured with a real-time differential moire interferometer. Hearing Research, 70(2), 229–242.

von Unge, M., Decraemer, W. F., Dirckx, J. J., & Bagger-Sjöbäck, D. (1995). Shape and displacement patterns of the gerbil tympanic membrane in experimental otitis media with effusion. Hearing Research, 82(2), 184–196.

Vanhuyse, V. J., Creten, W. L., & Van Camp, K. J. (1975). On the W-Notching of tympanograms. Scandinavian Audiology, 4(1), 45–50. Taylor & Francis.

Wali, H. A., Mazlan, R., & Kei, J. (2019). A longitudinal analysis of pressurized wideband absorbance measures in healthy young infants. Ear and Hearing, 40(5), 1233–1241.

Wang, B., Ghanta, P., Vinnikova, S., Bao, S., Liang, J., Lu, H., & Wang, S. (2017). Wrinkling of tympanic membrane under unbalanced pressure. Journal of Applied Mechanics, 84(4), 041002.

Warnholtz, B., Schär, M., Sackmann, B., Lauxmann, M., Chatzimichalis, M., Prochazka, L., Dobrev, I., Huber, A. M., & Sim, J. H. (2021). Contribution of the flexible incudo-malleal joint to middle-ear sound transmission under static pressure loads. Hearing Research, 108272.

# Chapter 5: A non-linear finite-element model of the gerbil middle ear under quasi-static pressures

To be submitted to the *Journal of the Association for Research in Otolaryngology*.

This chapter describes the finite-element model that was developed for comparisons with the experimental results from Chapters 3 and 4. The model was based on a previous model from our lab that was able to simulate the superimposed response to sound pressure and static pressure. The key difference was the implementation of a series of pressure steps and sweeps for the model input.

## 5.1 Introduction

Tympanometry is a clinical test that is used to evaluate the status of the middle ear. It has been used to detect cholesteatoma (Colletti, 1975), Menière's disease (Bianchedi et al., 1996), and otitis media (Ferekidis et al., 1999), among other pathologies. A tympanometer records the input acoustic admittance at the ear-canal opening while varying the quasi-static pressure within the canal. Acoustic admittance is a ratio of volume velocity to acoustic pressure. The input admittance of the ear canal gives some insight into the overall status of the eardrum. However, it does not provide information about spatial vibration patterns on the eardrum, which are complex and are sensitive to changes in the middle ear (e.g., Khanna & Tonndorf, 1972; Decraemer et al., 1989, 1997; Eiber et al., 2000; Maftoon et al., 2013). Pressurization rate and direction and anatomical differences can create differences in tympanogram shapes and meanings (e.g., Feldman et al., 1984; Shanks & Wilson, 1986; Holte et al., 1991; Roush et al., 1995; Therkildsen & Gaihede, 2005). In order to acquire more information, newer tympanometric methods use multi-frequency (Colletti, 1975) and wideband (Keefe et al., 1992) acoustic inputs. These methods have been shown to detect otherwise undetectable features but the additional information is more difficult to interpret.

To obtain a deeper understanding of tympanometry, and hopefully provide clinicians with more precise conclusions from tympanograms, computational models of the middle ear under both sound stimuli and quasi-static pressures should be useful. Chen and Shen (1996) reported a lumped-circuit model of tympanometry, with parameters that varied with the applied static pressure. Although they were able to show the effect of static pressure on the input admittance, they were unable to distinguish which component contributed to the asymmetric response of the middle ear.

Finite-element (FE) modelling is a more powerful tool for simulating complex mechanoacoustic systems such as the middle ear (as reviewed in Funnell et al., 2012). FE analysis of the middle ear was introduced by Funnell and Laszlo (1978) for cats. FE models have also been developed for the human middle ear (e.g., Wada et al., 1992; Beer et al., 1999; Prendergast et al., 1999; Sun et al., 2002; Gan et al., 2004) and other species (e.g., Funnell et al., 1987; Funnell, 1996; Funnell & Decraemer, 1996b; Motallebzadeh & Puria, 2021). These models provided insight into the motion of the eardrum and the middle ear in response to sound.

Modelling tympanometry requires representing non-linearity over a wide range of pressure and time scales: quasi-static pressure changes of thousands of Pascals within several seconds, and sound-pressure changes of fractions of a Pascal within microseconds. In addition to material non-linearity, the eardrum and middle ear also introduce geometrical non-linearity, as well as contact non-linearity (e.g., Soleimani et al., 2018). The response of the middle ear to the large quasi-static pressures of tympanometry was first studied with a FE model of the cat eardrum that included geometric non-linearities but linear material properties (Ladak & Funnell, 1996; Ladak et al., 2006). Qi et al. (2006, 2008) then developed FE models of the newborn human external and middle ear that included material non-linearities. Wang et al. (2007) also presented a non-linear model for the response to quasi-static pressures, in their case for the adult human middle ear, and then modelled the pressurized response to sounds using an empirical formula for the changing material properties as functions of the quasi-static pressure. Motallebzadeh et al. (2013) combined viscoelasticity using a 3-element Prony series and material non-linearity using an Ogden model. Their model of a strip of eardrum was able to simulate non-linear responses, including hysteresis, for large quasi-static deformations.

Gerbil middle-ear models are specially attractive due to their large body-to-eardrum-size ratio and smaller variability than humans (Ravicz et al., 1992; Rosowski et al., 1999). The deformation of the gerbil eardrum under quasi-static pressures has been studied previously (Dirckx et al., 1998; Dirckx & Decraemer, 2001; Larsson et al., 2001). Our lab has recorded extensive unpressurized vibration measurements on the gerbil eardrum (Ellaham et al., 2007; Maftoon et al., 2011, 2013, 2014) and with quasi-static pressures (Shapiro, 2014; Kose et al., 2020; 2021, under review). Several finite-element models of the gerbil middle ear have been developed in our lab (Elkhouri et al., 2006; Maftoon et al., 2011, 2015; Choukir, 2017; Qian, 2020).

Based the linear gerbil middle-ear model of Maftoon et al. (2015), a non-linear model of the gerbil middle ear was developed using a Mooney-Rivlin material model (Choukir, 2017). The geometry was simplified to reduce the computational expense, replacing the ossicular chain with a large stiff wedge supported by a block that ensured a fixed axis of ossicular rotation. They represented viscoelasticity using a 6-term Prony series. The acoustic stimulus was superimposed on the quasi-static pressure variations. They reported hysteresis in the vibration responses for pressurization rates between 200 and 1500 Pa/s. They observed an irregularity around +150 to

+300 Pa, which they suggested might be attributed with a buckling of the tympanic membrane (TM). This model was further developed to include the incudostapedial joint, the lenticular plate, and the contributions of middle-ear ligaments and other supporting structures (Qian, 2020). They simulated quasi-static pressure changes in the form of a step, similar to the experiments we described in Kose et al. (2020). Their simulated low-frequency vibration responses were comparable to those in the experiments. As the pressure was increased, the vibration magnitudes decreased and the peaks shifted to higher frequencies, in line with experimental observations. Although a very sharp peak at around 1.8 kHz was visible at 0 Pa, this peak was not visible at other pressures in the model when the pressure was increased. The peak around 2.4 kHz shifted to 8.2 kHz at 2500 Pa, similar to the experimental observations.

In this study, we have modified the material properties and solver settings used by Qian (2020) to better fit the features of the pressurized responses in the experimental results in Kose et al. (2020) and (Kose et al., 2021, under review). The details of the model and the modified material properties are given in the following section. The simulated displacements of the points on the eardrum where the experimental measurements were made are reported and compared with the experimental findings. Finally, limitations of the model and directions for future improvement are discussed.

## 5.2 Methods

### 5.2.1 Mesh geometry and model components

The FE simulations were done using the open-source FEBio (https://febio.org, version 2.0), on the Béluga cluster of Compute Canada (https://www.computecanada.ca). The specific node used for the simulations had two Intel Gold 6148 Skylake processors running at 2.4 GHz and had a maximum available memory of 96 GB. The simulations were performed on 8 cores in parallel, each core using 1 GB of RAM. Each simulation for a full pressurization cycle (210 s) took close to 7 days.

The FE model used in the simulations is shown in Figure 5.1. The model includes the pars flaccida (PF) and pars tensa (PT) of the TM; two wedge structures representing the rest of the malleus and the part of the incus lateral to the pedicle; the pedicle and the lenticular plate; the incudostapedial joint; and a block representation of the stapes. The $x$ and $y$ directions of the

model are perpendicular and parallel to the manubrium, respectively, and the *z* direction of the model is opposite to the normal of the manubrium at the umbo. All the elements of the mesh are quadratic tetrahedra (tet10). The model also includes discrete elements, including springs that represent the anterior mallear process, the posterior incudal ligament, and the stapedial annular ligament; and four dashpots that account for the cochlear load. The geometry is identical to the one used by Qian (2020), which itself was derived from that of Choukir (2017) by modifying the wedge block and adding the incudostapedial joint and surrounding structures. The geometry of Choukir (2017) was based on that of Maftoon et al. (2015), simplified to accommodate the increased computational requirements of non-linearity.

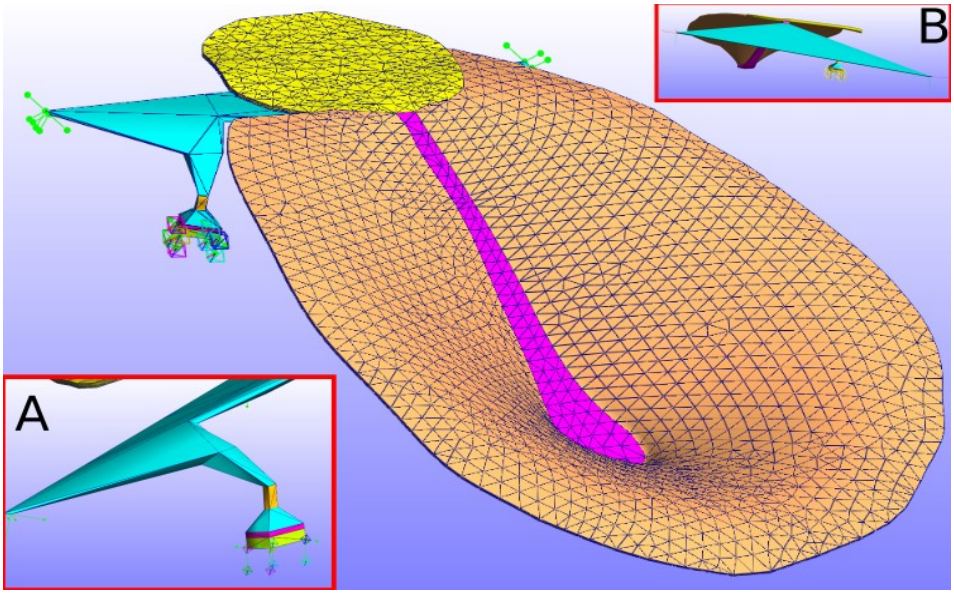


*Figure 5.1: 3D model geometry. Orange = PT, yellow = PF, magenta = manubrium, cyan = malleus and incus replacement wedges 1&2. Insert A: Close-up of the wedges and the ISJ from the posteroinferior direction. Dark gold = pedicle, purple = ISJ, yellow = stapes block. Insert B: View from superior to the TM, showing the fixed rotation axis of the wedge from left to right.*

The pressure input was calculated as the superposition of a quasi-static pressure input and a sound-pressure input. Two separate pressure protocols were modelled: (1) a series of 500-Pa steps with a rise time of 0.25 s (corresponding to a rate of 2000 Pa/s), held for 10 s each; and (2) a series of sweeps with a pressurization rate of 50 Pa/s (or 500 Pa in 10 s). For both protocols, the pressure is decreased from 0 Pa to −2500 Pa, increased to +2500 Pa, and then decreased back

to 0 Pa. This is the pressure profile that was used in the experimental measurements. The rise time of 0.25 s for the series of steps was chosen to facilitate convergence of the stiffness matrix in the FE solver. The pressure protocols are illustrated in Figure 5.2.

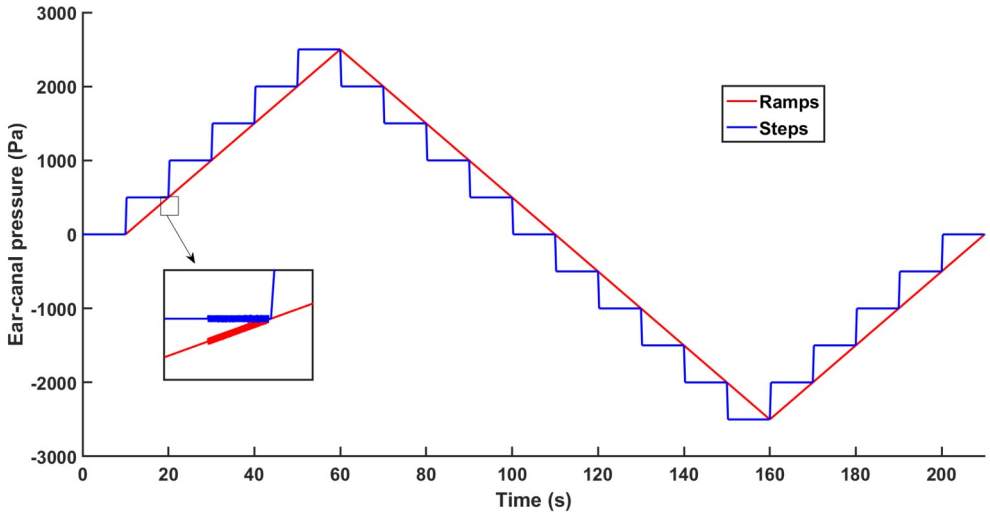


*Figure 5.2: Pressure profiles for both protocols.*

The sound input had an amplitude of 1 Pa, the same as in Qian (2020). However, the shape was changed from the single-frequency tone burst used by Qian to a chirp with the frequency varying linearly between 0.5 and 6 kHz in 128 ms. The sound pressure is only applied near the end of each 10 s interval to ensure that the transient effect of the step has died out (The same time point is used in the sweeps for consistency). Only a single chirp is applied per interval in order to save computation time. The pressure is applied to the lateral side of the eardrum. Both quasi-static pressure protocols had a total simulated time of 210 s.

In order to reduce the overall computation time, each 10-s interval (equivalent to one 500-Pa step or a 500-Pa rise of the sweep) was divided into two sections (referred to as ‘control steps’ in FEBio). The first control step was referred to as the ‘transient’ step, where no sound pressure is applied and the transient due to the abrupt pressure increase can die down. This section had a relatively large solver time step of 1/32 s. The ‘stimulus’ control step is located at the end of the 10-s window and is where the sound pressure is applied; it has a total duration of 140 ms and a solver time step of 31.25 μs (equivalent to 32000 Hz). There are 42 control steps in all.

The quasi-static pressure variations during the responses to the chirps were separated using additional simulations that only included the quasi-static pressure inputs. The results from these simulations were subtracted from the corresponding response to both quasi-static pressures and chirps. The frequency response was computed using an FFT window of 140 ms for the whole duration of the stimulus section, including 12 ms of zero padding after the stimulus itself, to allow the vibrations to die out to less than 1%.

### 5.2.2 Boundary conditions

The boundary conditions were the same as in Qian (2020). The annulus around the PT and PF was considered to be fully clamped (no translation or rotation allowed). The ossicles were assumed to have a fixed axis of rotation around a line between the most anterior and most posterior nodes of the incudomallear wedge (Figure 5.1B). This fixed axis of rotation represents the frequently described low-frequency anatomical axis between the anterior mallear ligament and the posterior incudal ligament.

The wedge was supported at its medial superior edge by two sets of very stiff translational springs (k=1000 N/m) that enforce the fixed axis of rotation (since the wedges are effectively rigid), and laterally by two sets of three orthogonal springs (k=10 N/m) that provide the effective rotational stiffness of the suspensory ligaments of the ossicular chain.

At the footplate there are four sets of three orthogonal springs (k=55 N/m each) and matching dashpots (c=0.006 $Ns/m^3$ each), aligned parallel to the coordinate axes, that represent the stapedial annular ligament and the cochlear damping, respectively. The springs represent the stapedial annular ligament, with the stiffness fitted to match the low-frequency magnitude at the umbo recorded in the experimental measurements. The damping coefficient was based on stapes footplate measurements (de La Rochefoucauld et al., 2008).

### 5.2.3 Material properties

There have not been any measurements of the material properties of the gerbil middle ear and our previous models used estimated parameters (Maftoon et al. 2015; Choukir 2017; Qian 2020). Most of the parameters here were based on Qian (2020). Some of the viscoelastic and non-linear parameters for the PF and PT were modified to make the simulated vibration responses better fit

our experimental results (Kose et al. 2020; 2021, under review). The following sections provide more details.

#### 5.2.3.1 Tympanic membrane

Qian (2020) utilized a time-dependent and non-linear material model for the TM. The non-linearity was represented by a hyperelastic Mooney-Rivlin model as used by Wang et al. (2007). This model defines the strain energy density function ($W$) as a linear summation of two invariants ($I_1$ and $I_2$) of the left Cauchy-Green deformation tensor. The general strain energy density function can be related to material stress by

$$S_{ij} = \frac{\delta \rho_0 W}{\delta E_{ij}}$$

where $S_{ij}$ are the first Piola Kirchhoff stress components in each direction, $E_{ij}$ are the corresponding strain components, and $\rho_0$ is the material density. The equation for the strain energy density function for a Mooney-Rivlin material is written as

$$W = C_{10}(I_1 - 3) + C_{01}(I_2 - 3) + \frac{\kappa}{2}(J-1)^2$$

where $C_{10}$ and $C_{01}$ are material constants, $\kappa$ is the bulk modulus, and $J$ is the Jacobian (the determinant of the deformation gradient). The ratios of $C_{10}$ to $C_{01}$ for both PF and PT were doubled from the values used by Qian (2020) without changing their sum, to keep the low-frequency magnitudes comparable to the experimental findings while increasing the resonance frequencies.

The time dependence was represented by a Prony series. This method represents the damping of the TM over the wide frequency range of the input with a set of time constants. The relaxation function can be represented as

$$G(t) = g_\infty + \sum_{i=1}^{N} g_i \exp(-t/\tau_i)$$

where $g_\infty$ is the long-term coefficient and the $g_i$ ($i$>0) are the Prony-series coefficients with the time constants $\tau_i$ for $N$ exponential terms. Following Qian (2020), we used six terms to model the time dependence of the TM (as FEBio has a limit of 6 terms). A common method of applying damping across the frequency range is to spread the time constants evenly on the logarithmic

time axis, ideally about a decade apart (Tschoegl 1989, p. 130). Here the six time constants were set ~2.2 decades apart to cover the range from the ultra-low frequencies (20 mHz corresponding to τ=52 s) of the quasi-static pressure variations to the high frequencies (100 kHz corresponding to τ=10 μs) of the acoustic stimulus. Although Qian (2020) kept all of the coefficients for both PF and PT at 0.07 except for $g_2$ in the pars flaccida (which was set to 0.40 to better fit the experimental results), these values caused the simulated middle-ear resonance peak to be much sharper than in our experimental results. The values of $g_2$ and $g_3$ for both PF and PT were increased here to 0.4, to reduce the peak magnitude while keeping a similar resonance frequency. A summary of the PF and PT material properties is given in Table 1.

*Table 1: Material properties of the TM*

| Material parameters | | PF | PT |
|---|---|---|---|
| Mooney-Rivlin coefficients | $C_{10}$ (MPa) | 1.3073 | 0.0974 |
| | $C_{01}$ (MPa) | 0.3705 | 0.0244 |
| | $\kappa$ (MPa) | 167.785 | 12.18 |
| | $\rho_0$ (kg/m$^3$) | 1100 | 1300 |
| Prony series parameters | $g_1$-$g_6$ | [0.07, 0.4, 0.4, 0.07, 0.07, 0.07] | [0.07, 0.4, 0.4, 0.07, 0.07, 0.07] |
| | $\tau_1$-$\tau_6$ (s) | [1e-5, 2.2e-4, 5e-3, 1.1e-1, 2.3, 52] | [1e-5, 2.2e-4, 5e-3, 1.1e-1, 2.3, 52] |

#### *5.2.3.2 Other structures*

Following Qian (2020), the incudostapedial joint (ISJ) was modelled as viscoelastic, represented by a 2-term Prony series with coefficients 0.8 and 0.5 at time constants 1.5 and 35 s, respectively, as suggested by Soleimani et al. (2020). Unlike the PT and PF, the ISJ was modelled as a linear isotropic material with a fitted long-term Young's modulus of 10 MPa.

The material properties for the rest of the components (the manubrium, the wedges that replaced the malleus and most of the incus, the pedicle near the lenticular plate, and the stapes block) were all assigned a Young's modulus of 16 GPa, so as to be effectively rigid.

The Poisson's ratio was set to 0.3 for all structures except the TM. The material density was set to 1100 kg/m$^3$ for all structures except the PT, for which it was set to 1300 kg/m$^3$.

## 5.3 Results

In this section, the simulated umbo responses for both the step and sweep pressurization protocols are compared with the sweep experimental responses of G47 from Kose et al. (2021, in review). The umbo response of G47 was typical among the 6 gerbils reported in that paper. The first subsection below illustrates the static displacement at the umbo (which could not be measured experimentally) and the following subsection shows the vibration response. Note that even though the horizontal axis is shown as middle-ear pressure, the pressure input was applied on the lateral side of the TM in the simulations; it was converted from external-canal pressure to middle-ear pressure for the following sections, since the middle-ear was pressurized in the experimental results.

### 5.3.1 Quasi-static response

The quasi-static umbo displacements for both pressurization protocols are given in Figure 5.3. The static displacement was highly asymmetric for negative and positive pressures. The displacement for the negative middle-ear pressure reached around 0.15 mm at −2500 Pa and had almost plateaued. The displacement in the positive middle-ear pressure half cycle was much larger, reaching 0.65 mm at +2500 Pa, and was still changing rapidly at that pressure. The step and sweep protocols gave very similar displacement magnitudes for large pressures, with the largest but still small differences between −500 Pa and +500 Pa. The largest difference between the two protocols was at the end of the cycle, 9 μm at 0 Pa. There was very little hysteresis for both protocols. The sweep protocol produced a displacement difference of 21 μm at 0 Pa, compared to only 5 μm for the step protocol. Since Kose et al. (2020, 2021, under review) did not include displacement measurements, these simulated values were compared to earlier displacement measurements in gerbil (von Unge et al., 1993; Dirckx & Decraemer, 2001). Von Unge et al. (1993) reported the static displacements over the whole gerbil TM with open middle-ear cavity and found the average umbo displacement of 18 ears to be around 0.2 mm at +20 cm $H_2O$ in the external ear canal (corresponding to about −2000 Pa in the middle ear). (For negative canal pressures they described wrinkling of the PT but did not plot displacement profiles.) Dirckx and Decraemer (2001) recorded a more or less symmetrical response at the umbo, with displacements of around 0.2 mm at +2000 Pa and 0.15 mm at −2000 Pa.

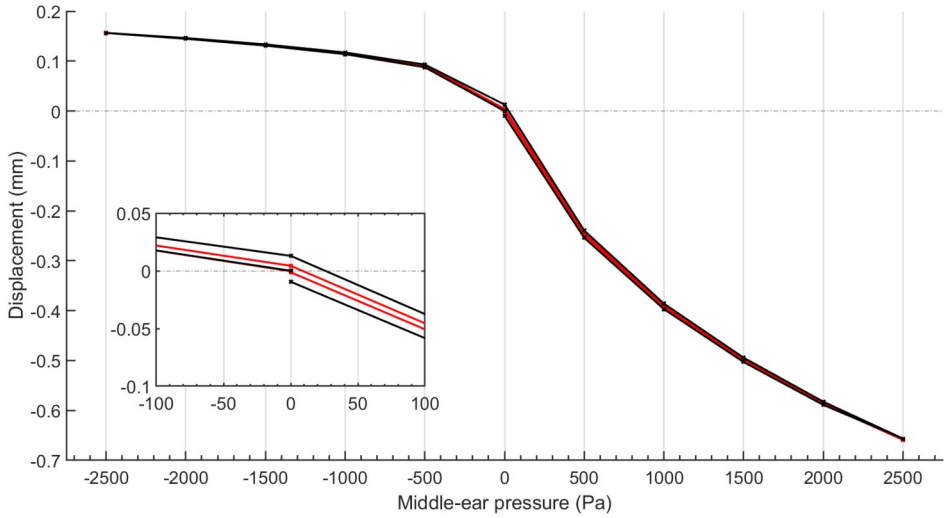


*Figure 5.3: Static displacement at the umbo for* sweeps *(black) and steps (red). Inset shows the difference for small pressures.*

### 5.3.2 Vibration response

The low-frequency (1 kHz) vibration magnitudes for both protocols are compared with the experimental sweep-protocol results (Kose et al. 2021, in review) in Figure 5.4. A frequency of 1 kHz is selected as it was well below the main resonance for both the model and G47. As seen from the figure, the unpressurized low-frequency magnitude was similar for both simulated protocols and for G47, at 60 and 63 nm/Pa, respectively. In the negative middle-ear pressure half-cycle, the vibration magnitude for both simulated protocols rapidly decreased to around 2.7 nm/Pa at −1000 Pa, and more slowly for lower pressures. Until −1000 Pa, the vibration magnitude of G47 was higher than the magnitude for the model. When the pressure was decreased further, the vibration magnitude of the models decreased down to 1.3 nm/Pa at −2500 Pa, slightly greater than the value of 1 nm/Pa for G47. Unlike the experimental observations, the model did not show any magnitude dip for intermediate pressures with the sound stimulus at 500-Pa intervals. Furthermore, the large difference between the experimental loading and unloading phases in the negative middle-ear pressure half-cycle was not seen in the models. The simulated vibration magnitude was only slightly different between the step and sweep protocols when the pressure was increased back to 0 Pa, about 8 nm/Pa (62 and 54 nm/Pa, respectively).

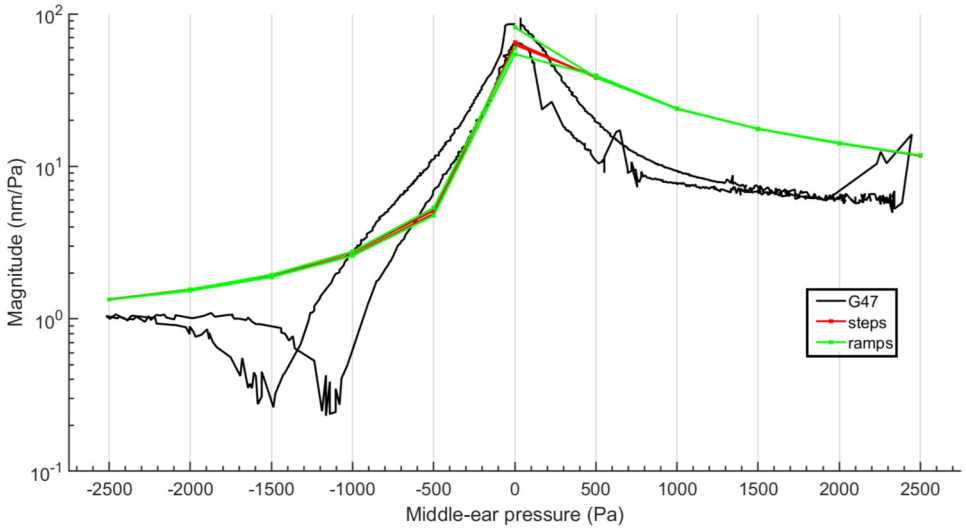


*Figure 5.4: Vibration response at the umbo at 1 kHz for the sweep experimental results (G47) and the model results (step protocol in red,* sweep *protocol in green)*

When the pressure was increased from zero to positive middle-ear pressures, the simulated vibration magnitude slowly decreased, down to 11.8 nm/Pa at +2500 Pa. G47 showed a much lower 1 kHz vibration magnitude in the positive middle-ear pressure half-cycle, decreasing quickly at first and then more slowly down to 6.3 nm/Pa (ignoring the artefact at the end). Smaller than in the negative middle-ear pressure half-cycle, the difference between the loading and unloading phases in the experiments is not observed for either simulated protocol except at 0 Pa. The simulated step and sweep pressurization protocols differed greatly at the end, with the step protocol reaching 66 nm/Pa, while the sweep protocol reaches 82 nm/Pa. The G47 1-kHz vibration magnitude is close to the sweep protocol at the end of the cycle, at 85 nm/Pa.

The complete frequency responses for the G47 experimental data (top panel) and for the step and sweep simulated protocols (middle and bottom panels) are illustrated in Figure 5.5. The initial unpressurized vibration responses for the models (solid black lines in the middle and bottom left-hand panels) increase slightly from 45 nm/Pa to a sharp peak at 1.7 kHz with a peak magnitude of 820 nm/Pa. For higher frequencies, the vibration magnitude decreases almost monotonically until 10 kHz. With the exception of the very sharp peak at 1.6 kHz, the model response is very similar to the unpressurized response of G47 (solid black line in the top-left panel). As explained in the experimental study (Kose et al., 2021), the G47 response shows an almost buried peak at 1.6 kHz (designated as R1), and another almost buried peak around

2.4 kHz (designated as R2) on the decreasing slope. These features are not seen in the simulated unpressurized frequency responses.

As the pressure is decreased from zero to negative values (from red lines at −500 Pa to cyan lines at −2500 Pa), the low-frequency vibration magnitude decreases, and when the frequency increases the magnitude is flat until the large peak. The peak magnitude decreases to 63 nm/Pa as its frequency shifts higher, reaching 6 kHz at −2500 Pa. After the main peak, there are multiple smaller peaks in the negative middle-ear pressure half-cycle. This pattern is significantly different from that of G47, especially for frequencies below R2. The magnitude dip until R1 and the small dip between R1 and R2 are not visible in the simulated results. The R2 frequency shifts somewhat further than the sharp peak in the model, reaching 8 kHz with a peak magnitude of 12 nm/Pa. The differences between the simulated step and sweep protocols are small in the negative middle-ear pressure loading direction, with peak-frequency differences less than 0.2 kHz. This is also true for the unloading direction, except for −500 Pa and 0 Pa, where the sweep protocol resonance was 150 Hz higher than in the loading direction.

The experimental vibration response showed a large difference between the loading and unloading directions of the negative middle-ear pressure half-cycle, largest at −1000 and −1500 Pa. The low-frequency magnitude dip, the dip between R1 and R2, and R1 itself were not visible in the model responses.

When the pressure was increased to positive values, the vibration response for both simulated protocols shifted less than in the negative-pressure half cycle. The main resonance gradually shifts from 1.7 kHz at 0 Pa to 3.1 kHz at +2500 Pa. The experimental responses, similar to those in the negative middle-ear pressure half-cycle, did not show a sharp peak, and R1 was visible up to +500 or +1000 Pa. Both simulated protocols showed very little difference between the loading and unloading directions in this half cycle, with the exception of 0 Pa at the end. The model responses displayed a more heavily damped resonance at 0 Pa at the end of the unloading direction, with a peak magnitude of 210 nm/Pa compared to the 700 nm/Pa at the beginning of the loading direction. The simulated sweep protocol also shows a significant difference in the frequency of the peak, 1.5 kHz compared to the 1.7 kHz in the loading direction. The differences between the 0 Pa values in the simulated loading and unloading directions were much smaller in the experimental responses.

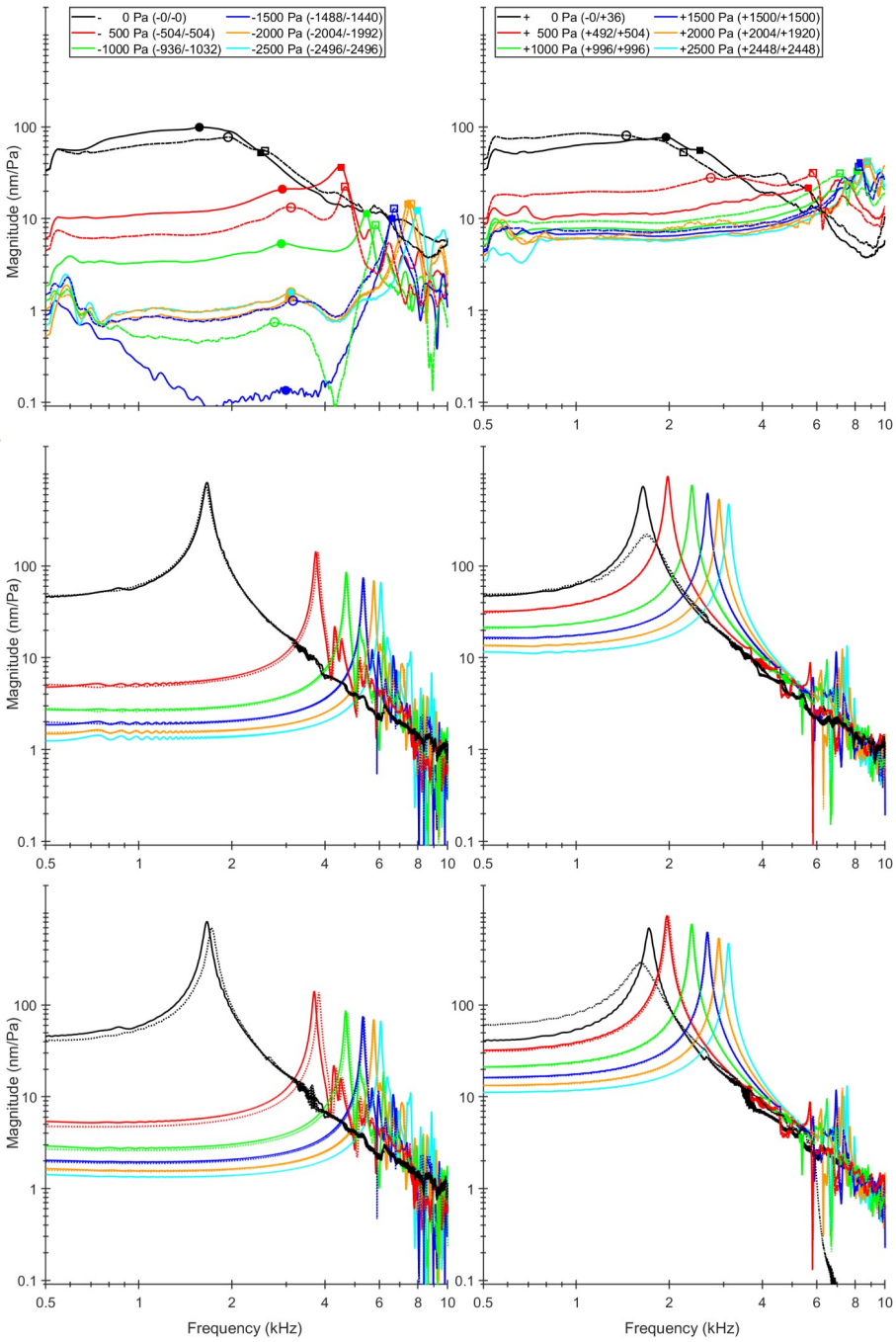


*Figure 5.5: Vibration response at the umbo for G47 (Kose et al. 2021, in review; top panels), and our model responses: step-wise pressurization protocol (middle panels), and* sweep *pressurization protocol (bottom panels). Loading phase = solid lines, unloading phase = dashed lines. The middle-ear pressure values are given in the top panel (experimental values are given in parentheses).*

## 5.4 Discussion

In this study we present a gerbil finite-element model that can simulate series of quasi-static pressure steps or sweeps in combination with sound stimuli. The results of the model compare reasonably well to some of the experimental findings (Kose et al., 2021, under review), but was not able to simulate some of the features.

The simulated static displacements were highly asymmetric between positive and negative middle-ear pressures. Some previous experimental measurements in gerbils did not find such an asymmetry (Dirckx & Decraemer, 2001). However, Gea et al. (2010) reported a strong asymmetry for their gerbil measurements up to ±2000 Pa ear-canal pressure. The cause of this asymmetry should be further explored with our model to determine the components that affect it.

Due to the computational cost of the simulations, the study was limited to 6 kHz, which excludes several key high-frequency features, such as the branches of the main resonance observed on the pars tensa (Kose et al. 2021, under review). In order to reduce the computation time of the model, optimization methods such as reduction of the degrees of freedom can be employed. For example, Ihrle et al. (2013), used Petrov–Galerkin projection to reduce the number of degrees of freedom, and found that it did not create any significant change to the vibration response at all static-pressure levels.

The simulated low-frequency vibration magnitudes for both the step and sweep protocols were within the inter-specimen variability of the experiments. However, the low-frequency pars-flaccida resonance that should be visible at the umbo as a peak was absent for all curves except the initial unpressurized response. Maftoon et al. (2015) observed this peak in their model and were able to remove it by applying 100 Pa on the lateral face of the pars flaccida. This suggests that the presence of even a small static pressure removes the peak from the vibration response.

Even though the Prony coefficients for the TM viscoelasticity were significantly increased from the values used by Qian (2020), the main resonance magnitude was much higher and sharper than those observed in experiments. The model of Maftoon et al. (2015) was able to replicate an unpressurized damped resonance similar to those observed in our experiments, but with Rayleigh damping for the TM. However, further investigation is needed of the effects of the Prony coefficients in our model.

The shifts of the resonance frequency with pressure were much smaller than the experimentally observed shifts in most of the pressure range except for small negative middle-ear pressures. Zhang et al. (2020) looked at the difference between elastic and viscoelastic modelling of the TM. They also observed larger frequency shifts of the resonances with increased static pressure when the TM damping was reduced. Their TM was approximated with a 1-term Prony series and an Ogden hyperelastic model. Therefore an analysis accounting for both our Mooney-Rivlin hyperelastic model parameters and our Prony coefficients may be necessary to ensure resonance frequencies similar to the ones observed in the experiments at all static pressure levels.

The experimentally observed manubrium magnitude dip was not visible in the simulated results. The magnitude dip may be related to the bending of the manubrium. Funnell et al. (1992) observed bending of the manubrium in their cat model. They also found that a rigid manubrium would increase the vibration magnitude at the umbo. The source of the magnitude dip could also be related to other simplifications of the ossicular chain in our model and should be further investigated.

The overall difference between the responses with steps and sweeps was small and similar to what was seen in the previous iterations of the model (Choukir, 2017; Qian, 2020), with the exception of the increased hysteresis produced by the sweep protocol. This suggests that the transient response is significant in the sweeps, even at a such low pressurization rate. It will be important to further investigate the effects of pressurization parameters such as the rate and the direction.

## Acknowledgements

This work was supported in part by the Canadian Institutes of Health Research, the Fonds de recherche en santé du Québec, the Natural Sciences and Engineering Research Council (Canada), the Montréal Children’s Hospital Research Institute, and the McGill University Health Centre Research Institute. Computations were made on the supercomputer Béluga at École de technologie supérieure, managed by Calcul Québec and Compute Canada. The authors thank Royan Jafari and Tina Qian for their contributions during the development of the model.

## References


Beer, H.-J., Bornitz, M., Hardtke, H.-J., Schmidt, R., Hofmann, G., Vogel, U., Zahnert, T., & Hüttenbrink, K.-B. (1999). Modelling of components of the human middle ear and simulation of their dynamic behaviour. Audiol Neurotol, 4(3–4), 156–162.

Bianchedi, M., Croce, A., Neri, G., & Moretti, A. (1996). [Multifrequency tympanometry in Meniere's disease: preliminary results]. Acta Otorhinolaryngol Ital, 16(1), 1–5.

Chen, L., & Shen, Y. (1996). A computational model for tympanometry. The Journal of the Acoustical Society of America, 99(6), 3558–3565. Acoustical Society of America.

Choukir, S. (2017). Finite-element modelling of tympanic-membrane vibrations under quasi-static pressurization (M.Eng. thesis). Montreal, Canada: McGill University.

Colletti, V. (1975). Methodologic observations on tympanometry with regard to the probe tone frequency. Acta Oto-Laryngologica, 80(1–6), 54–60. Taylor & Francis.

Decraemer, W. F., Khanna, S. M., & Funnell, W. R. J. (1989). Interferometric measurement of the amplitude and phase of tympanic membrane vibrations in cat. Hearing Research, 38(1), 1–17.

Decraemer, W. F., Khanna, S. M., & Funnell, W. R. J. (1997). Vibrations of the cat tympanic membrane measured with high spatial resolution. Presented at the 20th Midwinter Res. Mtg. Assoc. Res. Otolaryngol., St. Petersburg Beach, FL. Retrieved from zotero://attachment/19/

Dirckx, J. J. J., & Decraemer, W. F. (2001). Effect of middle ear components on eardrum quasi-static deformation. Hearing Research, 157(1), 124–137.

Dirckx, J. J. J., Decraemer, W. F., von Unge, M., & Larsson, C. (1998). Volume displacement of the gerbil eardrum pars flaccida as a function of middle ear pressure. Hearing Research, 118(1), 35–46.

Eiber, A., Freitag, H.-G., & Hocke, T. (2000). On the relationship between multifrequency tympanogram pattern and the dynamic behavior of the middle ear. In J. J. Rosowski & S. N. Merchant (Eds.), The function and mechanics of normal, diseased and reconstructed middle ears (pp. 157–166). Kugler Publications.

Elkhouri, N., Liu, H., & Funnell, W. R. J. (2006). Low-frequency finite-element modeling of the gerbil middle ear. J Assoc Res Otolaryngol, 7(4), 399–411.

Ellaham, N. N., Akache, F., Funnell, W. R. J., & Daniel, S. J. (2007). Spatial vibration patterns of the gerbil eardrum. Canadian Acoustics, 35(4), 38–39.

Feldman, R. M., Fria, T. J., Palfrey, C. C., & Dellecker, C. M. (1984). Effects of rate of air pressure change on tympanometry. Ear Hear, 5(2), 91–95.

Ferekidis, E., Vlachou, S., Douniadakis, D., Apostolopoulos, N., & Adamopoulos, G. (1999). Multiple-frequency tympanometry in children with acute otitis media. Otolaryngology - Head and Neck Surgery, 121(6), 797–801.

Funnell, W. R. J. (1996). Low-frequency coupling between eardrum and manubrium in a finite-element model. J Acoust Soc Am, 99(5), 3036–3043.

Funnell, W. R. J., & Decraemer, W. F. (1996). Finite-element modelling of the cat middle ear with elastically suspended malleus and incus. 19th ARO MidWinter Meeting.

Funnell, W. R. J., Decraemer, W. F., & Khanna, S. M. (1987). On the damped frequency response of a finite-element model of the cat eardrum. The Journal of the Acoustical Society of America, 81(6), 1851–1859.

Funnell, W. R. J., Khanna, S. M., & Decraemer, W. F. (1992). On the degree of rigidity of the manubrium in a finite-element model of the cat eardrum. The Journal of the Acoustical Society of America, 91(4), 2082–2090.

Funnell, W. R. J., & Laszlo, C. A. (1978). Modeling of the cat eardrum as a thin shell using the finite-element method. J Acoust Soc Am, 63(5), 1461–1467.

Funnell, W. R. J., Maftoon, N., & Decraemer, W. F. (2012). Mechanics and modelling for the middle ear. Retrieved from http://audilab.bme.mcgill.ca/mammie/

Gan, R. Z., Feng, B., & Sun, Q. (2004). Three-dimensional finite element modeling of human ear for sound transmission. Ann Biomed Eng, 32(6), 847–859.

Gea, S. L. R., Decraemer, W. F., Funnell, W. R. J., Funnell, R. W. J., Dirckx, J. J. J., & Maier, H. (2010). Tympanic membrane boundary deformations derived from static displacements observed with computerized tomography in human and gerbil. J Assoc Res Otolaryngol, 11(1), 1–17.

Holte, L., Margolish, R. H., & Cavanaugh, R. M. (1991). Developmental changes in multifrequency tympanograms. Audiology, 30(1), 1–24. Taylor & Francis.

Ihrle, S., Lauxmann, M., Eiber, A., & Eberhard, P. (2013). Nonlinear modelling of the middle ear as an elastic multibody system — Applying model order reduction to acousto-structural

coupled systems. Journal of Computational and Applied Mathematics, Fifth International Conference on Advanced COmputational Methods in ENgineering (ACOMEN 2011), 246, 18–26.

Keefe, D. H., Ling, R., & Bulen, J. C. (1992). Method to measure acoustic-impedance and reflection coefficient. Journal of the Acoustical Society of America, 91(1), 470–485.

Khanna, S. M., & Tonndorf, J. (1972). Tympanic membrane vibrations in cats studied by time-averaged holography. J Acoust Soc Am, 51(6), 1904–1920.

Kose, O., Funnell, W. R. J., & Daniel, S. J. (2020). Vibration measurements of the gerbil eardrum under quasi-static pressure steps. JARO, 21(4), 287–302.

Kose, O., Funnell, W. R. J., & Daniel, S. J. (2021). Vibration measurements of the gerbil eardrum under quasi-static pressure sweeps. JARO.

de La Rochefoucauld, O., Decraemer, W. F., Khanna, S. M., & Olson, E. S. (2008). Simultaneous measurements of ossicular velocity and intracochlear pressure leading to the cochlear input impedance in gerbil. JARO, 9(2), 161–177.

Ladak, H. M., & Funnell, W. R. J. (1996). Finite-element modeling of the normal and surgically repaired cat middle ear. The Journal of the Acoustical Society of America, 100(2), 933–944.

Ladak, H. M., Funnell, W. R. J., Decraemer, W. F., & Dirckx, J. J. J. (2006). A geometrically nonlinear finite-element model of the cat eardrum. The Journal of the Acoustical Society of America, 119(5), 2859–2868.

Larsson, C., von Unge, M., Dirckx, J. J. J., Decraemer, W. F., & Bagger-Sjöbäck, D. (2001). Displacement pattern of the normal pars flaccida in the gerbil. Otology & Neurotology, 22(4), 558–566.

Maftoon, N. (2014). Experimental and modelling study of gerbil middle ear (Ph.D.). Montreal, Canada: McGill University. Retrieved from http://audilab.bme.mcgill.ca/~funnell/AudiLab/theses/maftoon_2014_thesis.pdf

Maftoon, N., Funnell, W. R. J., Daniel, S. J., & Decraemer, W. F. (2013). Experimental study of vibrations of gerbil tympanic membrane with closed middle ear cavity. JARO, 14(4), 467–481.

Maftoon, N., Funnell, W. R. J., Daniel, S. J., & Decraemer, W. F. (2014). Effect of opening middle-ear cavity on vibrations of gerbil tympanic membrane. JARO, 15(3), 319–334.

Maftoon, N., Funnell, W. R. J., Daniel, S. J., & Decraemer, W. F. (2015). Finite-element modelling of the response of the gerbil middle ear to sound. JARO, 16(5), 547–567.

Maftoon, N., Nambiar, S., Funnell, W. R. J., Decraemer, W. F., & Daniel, S. J. (2011). Experimental and modelling study of gerbil tympanic-membrane vibrations. 34th Midwinter Research Meeting, Association for Research in Otolaryngology (pp. 19–23).

Motallebzadeh, H., & Puria, S. (2021). Mouse middle-ear forward and reverse acoustics. The Journal of the Acoustical Society of America, 149(4), 2711–2731. Acoustical Society of America.

Prendergast, P. J., Ferris, P., Rice, H. J., & Blayney, A. W. (1999). Vibro-acoustic modelling of the outer and middle ear using the finite-element method. Audiol Neurotol, 4(3–4), 185–191.

Qi, L., Funnell, W. R. J., & Daniel, S. J. (2008). A nonlinear finite-element model of the newborn middle ear. The Journal of the Acoustical Society of America, 124(1), 337–347.

Qi, L., Liu, H., Lutfy, J., Funnell, W. R. J., & Daniel, S. J. (2006). A nonlinear finite-element model of the newborn ear canal. The Journal of the Acoustical Society of America, 120(6), 3789–3798.

Qian, T. (2020). Finite-element modelling of middle-ear vibrations under quasi-static pressurization (M.Eng. thesis). Montreal, Canada: McGill University.

Ravicz, M. E., Rosowski, J. J., & Voigt, H. F. (1992). Sound-power collection by the auditory periphery of the Mongolian gerbil Meriones unguiculatus I: Middle-ear input impedance. The Journal of the Acoustical Society of America, 92(1), 157–177.

Rosowski, J. J., Ravicz, M. E., Teoh, S. W., & Flandermeyer, D. (1999). Measurements of Middle-Ear Function in the Mongolian Gerbil, a Specialized Mammalian Ear. Audiol Neurotol, 4(3–4), 129–136.

Roush, J., Bryant, K., Mundy, M., Zeisel, S., & Roberts, J. (1995). Developmental changes in static admittance and tympanometric width in infants and toddlers. J Am Acad Audiol, 6(4), 334–338.

Shanks, J. E., & Wilson, R. H. (1986). Effects of direction and rate of ear-canal pressure changes on tympanometric measures. Journal of Speech, Language, and Hearing Research, 29(1), 11–19. American Speech-Language-Hearing Association.

Shapiro, R. (2014). An experimental study of vibrations in the gerbil middle ear under static pressure (M.Eng. thesis). Montreal, Canada: McGill University. Retrieved from http://digitool.library.mcgill.ca/R/-?func=dbin-jump-full&object_id=126993&silo_library=GEN01

Soleimani, M., Funnell, W. R. J., & Decraemer, W. F. (2018). A new finite-element model of the incudostapedial joint (p. 110003). Presented at the To The Ear And Back Again - Advances In Auditory Biophysics: Proceedings of the 13th mechanics of hearing workshop, St Catharines, Canada. Retrieved from http://aip.scitation.org/doi/abs/10.1063/1.5038503

Soleimani, M., Funnell, W. R. J., & Decraemer, W. F. (2020). A non-linear viscoelastic model of the incudostapedial joint. JARO, 21(1), 21–32.

Sun, Q., Gan, R. Z., Chang, K.-H., & Dormer, K. J. (2002). Computer-integrated finite element modeling of human middle ear. Biomechanics and Modeling in Mechanobiology, 1(2), 109–122.

Therkildsen, A. G., & Gaihede, M. (2005). Accuracy of tympanometric middle ear pressure determination: The role of direction and rate of pressure change with a fast, modern tympanometer. Otology & Neurotology, 26(2), 252–256.

Tschoegl, N. W. (1989). The phenomenological theory of linear viscoelastic behavior. Berlin, Heidelberg: Springer Berlin Heidelberg. Retrieved from http://link.springer.com/10.1007/978-3-642-73602-5

von Unge, M., Decraemer, W. F., Bagger-Sjöbäck, D., & Dirckx, J. J. (1993). Displacement of the gerbil tympanic membrane under static pressure variations measured with a real-time differential moire interferometer. Hearing Research, 70(2), 229–242.

Wada, H., Metoki, T., & Kobayashi, T. (1992). Analysis of dynamic behavior of human middle ear using a finite-element method. The Journal of the Acoustical Society of America, 92(6), 3157–3168.

Wang, X., Cheng, T., & Gan, R. Z. (2007). Finite-element analysis of middle-ear pressure effects on static and dynamic behavior of human ear. The Journal of the Acoustical Society of America, 122(2), 906–917.

Zhang, J., Jiao, C., Zou, D., Ta, N., & Rao, Z. (2020). Assigning viscoelastic and hyperelastic properties to the middle-ear soft tissues for sound transmission. Biomech Model Mechanobiol, 19(3), 957–970.

# Chapter 6: Conclusion

## 6.1 Summary

The aim of this work was to gain insight into the vibration response of the in-vivo gerbil eardrum under quasi-static pressures, in order to ultimatelyextract more information from clinical tympanometry. We developed a method of measuring eardrum point vibrations using LDV while introducing quasi-static pressure steps and ramps in the gerbil middle-ear cavity. Vibration responses for the pars tensa, pars flaccida and manubrium were reported. Due to the shift of the peaks when the static pressure was introduced, as well as features that were visible in certain pressure ranges, single-frequency plots similar to tympanograms were not able to capture the complexity of the response. Therefore peak-frequency-versus-static-pressure plots and also spectrograms were used to present different perspectives. Similarities and differences between the responses to pressurization steps and ramps were highlighted. Finally, a previous finite-element model from our lab was modified, and simulated frequency responses under quasi-static pressures were compared to the experimental findings.

## 6.2 Original contributions

1. An experimental setup was developed to measure the in-vivo vibration response of the gerbil eardrum under quasi-static pressures

2. Vibrations of the gerbil eardrum in response to sound during quasi-static pressure steps were studied in vivo. The major findings are:

    a) The pressurized vibration responses on the manubrium and on the pars flaccida showed multiple peaks and troughs that were not visible in the unpressurized response.

    b) On the manubrium, a low-frequency feature that appeared as a broad shoulder at 1.8–2.3 kHz at 0 Pa became a distinct peak that shifted to around 2.6–4.5 kHz at −2500 Pa. This peak was also visible for pressures up to +1000 Pa, but not for higher pressures.

c) This same peak was only visible for pressures between −1000 to −500 Pa and +500 Pa to +1000 Pa on the anterior and posterior pars tensa.

d) A common peak that was observed across all points shifted from 2.2–3.2 kHz at 0 Pa to 2.6–9.2 kHz at −2500 Pa. The same peak shifted to 6–9 kHz at +2500 Pa.

e) This peak was part of a cluster at the anterior and posterior pars-tensa points.

f) The vibration response at the mid-manubrium was similar to that at the umbo for all pressure levels, but overall lower in magnitude.

g) A pronounced magnitude dip around 1.3–2 kHz was observed in the negative-pressure half-cycle at the manubrial points but not at the other measurement points.

h) The vibration response on the pars flaccida changed drastically even for pressures as low as ±500 Pa, and multiple peaks and troughs were observed.

3. Vibrations of the gerbil eardrum in response to sound during quasi-static pressure sweeps were studied in vivo. The key additional observations are:

   a) The vibration responses at the umbo and the pars tensa under quasi-static pressure ramps were similar to those under quasi-static steps, but with more hysteresis, especially at low frequencies.

   b) The magnitude dip at the manubrium was observed near the main resonance around −900–1400 Pa and rapidly shifted to include all frequencies below the resonance. The dip also appeared at frequencies above the resonance at smaller pressures (−700 to 1100 Pa) in some gerbils.

   c) In the negative middle-ear pressure half-cycle, the main resonance shifted mostly linearly with pressure. There were multiple closely spaced peaks observed at higher frequencies that rapidly shifted when the pressure was changed.

   d) In the positive middle-ear pressure half-cycle, the main resonance split into multiple branches on both the manubrium and the pars tensa, and plateaued around +1700 to +2000 Pa. A major branch split at around +700–1000 Pa and shifted to 8–9.2 kHz at +2500 Pa. On the posterior pars tensa, a trough between these two branches was observed which was visible as a peak on the anterior pars tensa.

4. A finite-element model was developed and simulation results were compared to the previously mentioned experimental results. Both step-wise and ramp pressurization responses were reported. Highlights of the results are:

    a) The static displacement at the umbo was highly asymmetric between the negative and positive middle-ear pressures, with the latter having around four times larger displacements. This was in line with gerbil TM shape measurements in the literature.

    b) The simulated low-frequency umbo vibration magnitude was similar for both pressure protocol, but the ramp protocol produced more hysteresis, especially in the positive middle-ear pressure half-cycle.

    c) The models had low-frequency umbo vibration magnitudes that were similar to the experimental results in a number of ways, but they were not able to replicate the magnitude dip in the negative middle-ear pressure half-cycle.

    d) Even with Prony-series coefficients larger than the ones used in the previous model by Qian (2020), the main resonance at the umbo of the model was not as heavily damped as the ones observed in the experiments.

    e) The frequency shift of the main resonance of the model was much less than in the experimental results in the positive middle-ear pressure half-cycle.

## 6.3 Future work

### 6.3.1 Experimental work

The current study was able to provide an animal model for in-vivo multi-point eardrum measurements. However, certain shortcomings of the current setup could be alleviated. For one thing, the acoustic coupler described in Chapter 3 currently needs to remain attached to the bony meatus throughout the experiment, making it impossible to rehydrate or ventilate the lateral side of the eardrum. Making it removable could reduce the effects of dehydration and possibly account for the differences between our unpressurized responses and those of Maftoon et al. (2013).

Another main area for improvement in the experimental setup is the bead tracking. Due to the quasi-static pressure displacements, using the LDV’s joystick becomes essential for keeping the

reflective glass bead in focus. However, pressurization rates like those in clinical tympanometry are too fast for manual tracking. Therefore an automated tracking method using an electromechanical positioner on the joystick, the mirror and/or the gerbil eardrum is required. Since the rotation of the mirror for tracking a single bead during the pressurization cycle is less than 1°, a miniature platform could be installed and attached to the joystick controller, similar to those used in scanning LDV systems (e.g., Tirabassi & Rothberg, 2009; Chen et al., 2012). Either a camera sensor or a laser-strength-based algorithm could be implemented to ensure rapid aiming of the laser beam during the pressurization cycle. This would also permit measurements at points where the large displacement make it impossible to record using manual tracking (e.g., on the pars flaccida).

Faster pressurization rates, similar to those in clinical tympanometry, will provide a more relevant representation of the effects of static pressure ramps on the gerbil eardrum. The effects of the pressurization rate itself are also an important question to investigate. Clinical tympanometers can have various rates (typically between 500 and 2000 Pa/s) and the effects are not well understood (e.g., Feldman et al., 1984; Shanks & Wilson, 1986; Therkildsen & Gaihede, 2005). An experiment that explores various pressurization rates, as well as both positive and negative sweep directions, could provide more understanding of the hysteresis in the system.

The results from this work could also be compared with admittance measurements. Von Unge et al. (1991) measured the gerbil admittance at two probe tones and concluded that a gerbil tympanometry model could be used for studying middle-ear pathologies. A robust setup that can compare multi-frequency or wideband tympanometry with the multi-point LDV vibration measurements could help determine the specific contributions of the ear canal and eardrum to the input admittance.

### 6.3.2 Modelling work

The model described in Chapter 5 gives insight into the parameters that determine the effects of static pressure on the vibration response of the gerbil eardrum. Due to the heavy computational load, several parts of the model were simplified. Maftoon et al. (2015) included detailed ligament and ossicular geometry in their linear model, but it was replaced by the wedges and the stapes block in the model of Qian (2020). The full geometry could be restored to see if the wedge-and-block approximation was acceptable under quasi-static pressures. As discussed in

Chapter 5, the model fails to simulate certain features observed in the experiments, such as the magnitude dip at the manubrial points, and low-frequency peaks. It will be important to explore why that is.

The long simulation times of the model also prevented us from increasing the sampling frequency, limiting our upper frequency limit to 6 kHz. For the ramp pressurization protocol, it will be desirable to simulate many more chirps (with their required much smaller step sizes) so that the vibration response of the model to small pressure changes can be investigated and spectrograms like those in Chapter 4 can be computed. Using the restart feature of FEBio could allow modelling of the higher-frequency features observed in the experiments, by allowing us to exceed the maximum run times allowed on the Compute Canada clusters. However, it will also be important to find ways to speed up the computations. This can be achieved through a multitude of approaches. For example, specifying that structures like the ossicles are perfectly rigid should help, by reducing the number of degrees of freedom to be computed. Other methods include hybrid multi-body modelling (e.g., Ihrle et al., 2013; Calero et al., 2020), substructuring (e.g., El Maani et al., 2018), model reduction (Ihrle et al., 2013) and “metamodelling” (e.g., Viana et al., 2014; Liu et al., 2018).

A complete sensitivity analysis of the material and geometrical parameters is required to determine the appropriate parameter ranges and improve the fit between model and experiment. Another key benefit of the analysis would be to identify less important parts of the model for removal, to reduce computation time. A sensitivity analysis that takes parameter interactions into account can be shortened by using optimization techniques such as the Taguchi method (Qi et al., 2005). As also mentioned in the section on future experimental work, modelling of the effects of pressurization rate and direction could augment the comparison of the gerbil results to clinical tympanometry.

## 6.4 Significance

Tympanometry is useful to noninvasively evaluate the status of the middle ear. Understanding middle-ear mechanics under sound and static pressures will lead to improvements in the clinical use of tympanometry. Due to the complexity of sound transmission through the external and middle ear, pressurized vibration measurements such as those in this study can provide useful

insights. Better understanding the effects of static pressure on the middle ear could give the clinician more detailed and accurate information from tympanometry. Furthermore, studies on the effects of static pressure on the middle ear could help with understanding the effects of everyday pressure changes and temporary pressure imbalances such as diving, airplanes, or negative-pressure medical rooms.

WBT is a more comprehensive tool that allows clinicians to distinguish between different middle-ear diseases, compared to traditional tympanometry. One advantage of WBT is to record on perforated eardrums. Performing wideband ambient-pressure tympanometry allows measurement of the frequency response of the input admittance. With a validated model, subtle features in the ambient admittance measurements such as the peaks and troughs in the unpressurized response reported here can be further investigated.

Another use of the frequency content of WBT is to identify key frequency ranges where presence of middle-ear fluid reduces the absorbance measurements. Computational models can simulate various cases to assess the vibration response of the middle ear filled with various fluids with different viscosities and at different levels. Developing such a pathology model can be used for classification of these fluids and their volumes.

Traditional clinical tympanometry can also benefit from the development of middle-ear models that address static pressures. An important observation in the literature is the shift in the overall admittance, especially the tympanometric peak pressure, due to procedural variables such as consecutive testing and pressurization profiles. The highly non-linear and viscoelastic behaviour of the eardrum and the other soft tissues can be observed as hysteresis and preconditioning effects. Our experimental data includes many consecutive pressurization cycles at each point. Furthermore, the vibration response during the initial sweep from 0 Pa to the pressure limit, as well as the final unloading phase, are also recorded in our experiments. This differs from many commercial tympanometers where only the decreasing pressure sweep from positive to negative ear-canal pressure is considered in the calculation of the admittance. The finite-element model can be an excellent tool for simulating the effect of the direction of the pressure sweep as well as for consecutive pressure sweeps.

Chapters 3 and 4 summarize experiments that show various features identified in the vibration response of the eardrum, which are dependent on different vibration modes of the middle ear.

These modes are determined by interactions among the eardrum, the ossicular chain, the ligaments, and the middle-ear cavity. Chapter 5 proposes a non-linear middle-ear model. Such models can help study the effects of various parameters that are linked to physiological differences. A more complete model could be used predict outcomes of pathological changes.

One long-term goal of this series of studies is to assess the use of tympanometry as a complementary test for newborn hearing screening. Tympanometry could provide crucial information due to its relatively fast and simple assessment of the external and middle ear, and it might help reduce the high false-positive rates in current screening tests.

# References

This list of references is for Chapters 1, 2 and 6 only.


Aithal, S., Aithal, V., Kei, J., Anderson, S., & Liebenberg, S. (2019). Eustachian tube dysfunction and wideband absorbance measurements at tympanometric peak pressure and 0 daPa. *J. Am. Acad. Audiol.*, *30*(9), 781–791.

Akache, F., Funnell, W. R. J., & Daniel, S. J. (2007). An experimental study of tympanic membrane and manubrium vibrations in rats. *Audiol. Neurootol.*, *12*(1), 49–58.

Alaerts, J., Luts, H., & Wouters, J. (2007). Evaluation of middle ear function in young children: Clinical guidelines for the use of 226- and 1,000-hz tympanometry. *Otol. Neurotol.*, *28*(6), 727–732.

Alberti, P. W., & Jerger, J. F. (1974). Probe-tone frequency and the diagnostic value of tympanometry. *Arch. Otolaryngol.*, *99*(3), 206–210.

Anthwal, N., & Thompson, H. (2016). The development of the mammalian outer and middle ear. *J. Anat.*, *228*(2), 217–232.

Beer, H.-J., Bornitz, M., Hardtke, H.-J., Schmidt, R., Hofmann, G., Vogel, U., Zahnert, T., & Hüttenbrink, K.-B. (1999). Modelling of components of the human middle ear and simulation of their dynamic behaviour. *Audiol. Neurotol.*, *4*(3–4), 156–162.

Békésy, G. von. (1941). Über die Messung der Schwingungsamplitude der Gehörknöchelchen mittels einer kapazitiven Sonde [On the measurement of the vibration amplitude of the auditory ossicles using a capacitive probe]. *Akust Z*, *6*(1), 1–16.

Bergevin, C., & Olson, E. S. (2014). External and middle ear sound pressure distribution and acoustic coupling to the tympanic membrane. *J. Acoust. Soc. Am.*, *135*(3), 1294–1312.

Bianchedi, M., Croce, A., Neri, G., & Moretti, A. (1996). [Multifrequency tympanometry in Meniere's disease: preliminary results]. *Acta Otorhinolaryngol. Ital. Organo Uff. Della Soc. Ital. Otorinolaringol. E Chir. Cerv.-facc.*, *16*(1), 1–5.

Boedts, D., & Kuijpers, W. (1978). Epithelial migration on the tympanic membrane: An experimental study. *Acta Otolaryngol. (Stockh.)*, *85*(1–6), 248–252. Taylor & Francis.

Buytaert, J. A. N., Salih, W. H. M., Dierick, M., Jacobs, P., & Dirckx, J. J. J. (2011). Realistic 3D computer model of the gerbil middle ear, featuring accurate morphology of bone and soft tissue structures. *J. Assoc. Res. Otolaryngol.*, *12*(6), 681–696.

Calero, D., Lobato, L., Paul, S., & Cordioli, J. A. (2020). Analysis of the human middle ear dynamics through multibody modeling. *J. Biomech. Eng.*, *142*(7), 071012.

CDC. (2019, December 4). Summary of infants not passing hearing screening diagnosed by 3 months. *Cent. Dis. Control Prev.* Retrieved August 17, 2021, from https://www.cdc.gov/ncbddd/hearingloss/2017-data/07-diagnosed-by-3-months.html

Chen, C.-D., Wang, Y.-J., & Chang, P. (2012). A novel two-axis MEMS scanning mirror with a PZT actuator for laser scanning projection. *Opt. Express*, *20*(24), 27003.

Chen, L., & Shen, Y. (1996). A computational model for tympanometry. *J. Acoust. Soc. Am.*, *99*(6), 3558–3565. Acoustical Society of America.

Cheng, J. T., Aarnisalo, A. A., Harrington, E., Hernandez-Montes, M. del S., Furlong, C., Merchant, S. N., & Rosowski, J. J. (2010). Motion of the surface of the human tympanic membrane measured with stroboscopic holography. *Hear. Res.*, MEMRO 2009: Middle-Ear Science and Technology, *263*(1), 66–77.

Cheng, J. T., Hamade, M., Merchant, S. N., Rosowski, J. J., Harrington, E., & Furlong, C. (2013). Wave motion on the surface of the human tympanic membrane: Holographic measurement and modeling analysis. *J. Acoust. Soc. Am.*, *133*(2), 918–937.

Chole, R. A., & Kodama, K. (1989). Comparative histology of the tympanic membrane and its relationship to cholesteatoma. *Ann. Otol. Rhinol. Laryngol.*, *98*(10), 761–766.

Choukir, S. (2017). *Finite-element modelling of tympanic-membrane vibrations under quasi-static pressurization* (M.Eng. thesis). Montreal, Canada: McGill University.

Colletti, V. (1975). Methodologic observations on tympanometry with regard to the probe tone frequency. *Acta Otolaryngol. (Stockh.)*, *80*(1–6), 54–60. Taylor & Francis.

Creten, W. L., & Van Camp, K. J. (1974). Transient and quasi-static tympanometry. *Scand. Audiol.*, *3*(1), 39–42. Taylor & Francis.

Cull, P. (1989). *The Sourcebook of medical illustration : Over 900 anatomical, medical, and scientific illustrations available for general re-use and adaptation free of normal copyright restrictions*. Carnforth, Lancs, U.K. ; Parthenon Pub. Group.

Dai, C., Wood, M. W., & Gan, R. Z. (2007). Tympanometry and laser Doppler interferometry measurements on otitis media with effusion model in human temporal bones. *Otol. Neurotol.*, *28*(4), 551–558.

De Greef, D., Goyens, J., Pintelon, I., Bogers, J.-P., Van Rompaey, V., Hamans, E., Van de Heyning, P., & Dirckx, J. J. J. (2016). On the connection between the tympanic membrane and the malleus. *Hear. Res.*, *340*, 50–59.

Decraemer, W. F., Creten, W. L., & Van Camp, K. J. (1984). Tympanometric middle-ear pressure determination with two-component admittance meters. *Scand. Audiol.*, *13*(3), 165–172. Taylor & Francis.

Decraemer, W. F., & Dirckx, J. J. J. (1998). Pressure regulation due to displacement of the pars flaccida and pars tensa of the tympanic membrane. *Oto-Rhino-Laryngol. Nova*, *8*(6), 277–281.

Decraemer, W. F., & Funnell, W. R. J. (2008). Anatomical and mechanical properties of the tympanic membrane. *Chronic Otitis Media Pathog.-Oriented Ther. Manag.*, 51–84.

Decraemer, W. F., & Khanna, S. M. (2000). Three-dimensional vibration of the ossicular chain in the cat (Vol. 4072, pp. 401–411). Presented at the Fourth International Conference on Vibration Measurements by Laser Techniques: Advances and Applications. Retrieved from http://dx.doi.org/10.1117/12.386747

Decraemer, W. F., Khanna, S. M., & Funnell, W. R. J. (1989). Interferometric measurement of the amplitude and phase of tympanic membrane vibrations in cat. *Hear. Res.*, *38*(1), 1–17.

Decraemer, W. F., Khanna, S. M., & Funnell, W. R. J. (1997). Vibrations of the cat tympanic membrane measured with high spatial resolution. Presented at the 20th Midwinter Res. Mtg. Assoc. Res. Otolaryngol., St. Petersburg Beach, FL. Retrieved from zotero://attachment/19/

Dirckx, J. J., & Decraemer, W. F. (1991). Human tympanic membrane deformation under static pressure. *Hear. Res.*, *51*(1), 93–105.

Dirckx, J. J. J., Buytaert, J. A. N., & Decraemer, W. F., W. F. (2006). Quasi-static transfer function of the rabbit middle ear, measured with a heterodyne interferometer with high-resolution position decoder. *J. Assoc. Res. Otolaryngol.*, *7*(4), 339–351.

Dirckx, J. J. J., & Decraemer, W. F. (2001). Effect of middle ear components on eardrum quasi-static deformation. *Hear. Res.*, *157*(1), 124–137.

Dirckx, J. J. J., Decraemer, W. F., von Unge, M., & Larsson, C. (1998). Volume displacement of the gerbil eardrum pars flaccida as a function of middle ear pressure. *Hear. Res.*, *118*(1), 35–46.

Eiber, A., Freitag, H.-G., & Hocke, T. (2000). On the relationship between multifrequency tympanogram pattern and the dynamic behavior of the middle ear. In J. J. Rosowski & S. N. Merchant (Eds.), *Funct. Mech. Norm. Dis. Reconstr. Middle Ears* (pp. 157–166). Kugler Publications.

El Maani, R., Makhloufi, A., Radi, B., & Hami, A. E. (2018). Reliability-based design optimization with frequency constraints using a new safest point approach. *Eng. Optim.*, *50*(10), 1715–1732. Informa UK Limited.

Elkhouri, N., Liu, H., & Funnell, W. R. J. (2006). Low-frequency finite-element modeling of the gerbil middle ear. *J. Assoc. Res. Otolaryngol. JARO*, *7*(4), 399–411.

Ellaham, N. N., Akache, F., Funnell, W. R. J., & Daniel, S. J. (2007). Spatial vibration patterns of the gerbil eardrum. *Can. Acoust.*, *35*(4), 38–39.

Fay, J. P., Puria, S., & Steele, C. R. (2006). The discordant eardrum. *Proc. Natl. Acad. Sci.*, *103*(52), 19743–19748. National Academy of Sciences.

Feizollah, S. (2019). *Microstructure and displacements of the gerbil incudostapedial joint under static pressures* (M.Eng. thesis). Montreal, Canada: McGill University.

Feldman, R. M., Fria, T. J., Palfrey, C. C., & Dellecker, C. M. (1984). Effects of rate of air pressure change on tympanometry. *Ear Hear.*, *5*(2), 91–95.

Ferekidis, E., Vlachou, S., Douniadakis, D., Apostolopoulos, N., & Adamopoulos, G. (1999). Multiple-frequency tympanometry in children with acute otitis media. *Otolaryngol. Head Neck Surg.*, *121*(6), 797–801.

Fu, Y., Pedrini, G., & Li, X. (2014). Interferometric dynamic measurement: techniques based on high-speed imaging or a single photodetector. *Sci. World J.*, *2014*, 232906.

Funnell, W. R. J. (1983). On the undamped natural frequencies and mode shapes of a finite-element model of the cat eardrum. *J. Acoust. Soc. Am.*, *73*(5), 1657–1661.

Funnell, W. R. J. (1996). Low-frequency coupling between eardrum and manubrium in a finite-element model. *J. Acoust. Soc. Am.*, *99*(5), 3036–3043.

Funnell, W. R. J., & Decraemer, W. F. (1996a). On the incorporation of moiré shape measurements in finite-element models of the cat eardrum. *J. Acoust. Soc. Am.*, *100*(2), 925–932.

Funnell, W. R. J., & Decraemer, W. F. (1996b). Finite-element modelling of the cat middle ear with elastically suspended malleus and incus. *19th ARO MidWinter Meet.*

Funnell, W. R. J., Decraemer, W. F., & Khanna, S. M. (1987). On the damped frequency response of a finite-element model of the cat eardrum. *J. Acoust. Soc. Am.*, *81*(6), 1851–1859.

Funnell, W. R. J., Khanna, S. M., & Decraemer, W. F. (1992). On the degree of rigidity of the manubrium in a finite-element model of the cat eardrum. *J. Acoust. Soc. Am.*, *91*(4), 2082–2090.

Funnell, W. R. J., & Laszlo, C. A. (1978). Modeling of the cat eardrum as a thin shell using the finite-element method. *J. Acoust. Soc. Am.*, *63*(5), 1461–1467.

Funnell, W. R. J., & Laszlo, C. A. (1982). A critical review of experimental observations on ear-drum structure and function. *ORL J. Oto-Rhino-Laryngol. Its Relat. Spec.*, *44*(4), 181–205.

Funnell, W. R. J., Maftoon, N., & Decraemer, W. F. (2012). Mechanics and modelling for the middle ear. Retrieved from http://audilab.bme.mcgill.ca/mammie/

Funnell, W. R. J., Siah, T. H., McKee, M. D., Daniel, S. J., & Decraemer, W. F. (2005). On the coupling between the incus and the stapes in the cat. *J. Assoc. Res. Otolaryngol.*, *6*(1), 9–18.

Gan, R. Z., Dai, C., & Wood, M. W. (2006). Laser interferometry measurements of middle ear fluid and pressure effects on sound transmission. *J. Acoust. Soc. Am.*, *120*(6), 3799–3810.

Gan, R. Z., Feng, B., & Sun, Q. (2004). Three-dimensional finite element modeling of human ear for sound transmission. *Ann. Biomed. Eng.*, *32*(6), 847–859.

Gea, S. L. R., Decraemer, W. F., Funnell, W. R. J., Funnell, R. W. J., Dirckx, J. J. J., & Maier, H. (2010). Tympanic membrane boundary deformations derived from static displacements observed with computerized tomography in human and gerbil. *J. Assoc. Res. Otolaryngol. JARO*, *11*(1), 1–17.

Gladiné, K., Wales, J., Silvola, J., Muyshondt, P., Topsakal, V., Van de Heyning, P., Dirckx, J., & von Unge, M. (2019). Evaluation of artificial fixation of the incus and malleus with minimally invasive intraoperative laser vibrometry (MIVIB) in a temporal bone model. *Otol. Neurotol.*, *41*, 1.

Graham, M. D., Reams, C., & Perkins, R. (1978). Human tympanic membrane - malleus attachment preliminary study. *Ann. Otol. Rhinol. Laryngol.*, *87*(3), 426–431. SAGE Publications Inc.

Gulya, A. J. (2007). *Anatomy of the temporal bone with surgical implications, Third Edition.* New York: Informa Healthcare USA. Retrieved from http://ebookcentral.proquest.com/lib/qut/detail.action?docID=1405498

Helmholtz, H. (1868). Die Mechanik der Gehörknöchelchen und des Trommelfells [Mechanics of the auditory ossicles and the eardrum]. *Arch. Für Gesamte Physiol. Menschen Tiere*, *1*(1), 1–60.

Holte, L., Margolish, R. H., & Cavanaugh, R. M. (1991). Developmental changes in multifrequency tympanograms. *Audiology*, *30*(1), 1–24. Taylor & Francis.

Homma, K., Shimizu, Y., Kim, N., Du, Y., & Puria, S. (2010). Effects of ear-canal pressurization on middle-ear bone- and air-conduction responses. *Hear. Res.*, MEMRO 2009: Middle-Ear Science and Technology, *263*(1), 204–215.

Hüttenbrink, K. B. (1988). The mechanics of the middle-ear at static air pressures: The role of the ossicular joints, the function of the middle-ear muscles and the behaviour of stapedial prostheses. *Acta Otolaryngol. (Stockh.)*, *105*(sup451), 1–35. Taylor & Francis.

Ihrle, S., Lauxmann, M., Eiber, A., & Eberhard, P. (2013). Nonlinear modelling of the middle ear as an elastic multibody system — Applying model order reduction to acousto-structural coupled systems. *J. Comput. Appl. Math.*, Fifth International Conference on Advanced COmputational Methods in ENgineering (ACOMEN 2011), *246*, 18–26.

Karmody, C. S., Northrop, C. C., & Levine, S. R. (2009). The incudostapedial articulation: New concepts. *Otol. Neurotol.*, *30*(7), 990–997.

Keefe, D. H., & Levi, E. (1996). Maturation of the middle and external ears: acoustic power-based responses and reflectance tympanometry. *Ear Hear.*, *17*(5), 361–373.

Keefe, D. H., Ling, R., & Bulen, J. C. (1992). Method to measure acoustic-impedance and reflection coefficient. *J. Acoust. Soc. Am.*, *91*(1), 470–485.

Kei, J., Allison-Levick, J., Dockray, J., Harrys, R., Kirkegard, C., Wong, J., Maurer, M., Hegarty, J., … Tudehope, D. (2003). High-frequency (1000 hz) tympanometry in normal neonates. *J. Am. Acad. Audiol.*, *14*(1), 20–28. American Academy of Audiology.

Kessel, J. (1874). On the influence of the middle-ear muscles on the displacements and vibrations of the eardrum in the cadaver ear. *Arch Ohrenheilkd*, *8*, 80–92.

Khaleghi, M., Furlong, C., Ravicz, M., Cheng, J. T., & Rosowski, J. J. (2015). Three-dimensional vibrometry of the human eardrum with stroboscopic lensless digital

holography. *J. Biomed. Opt.*, *20*(5), 051028.

Khanna, S. M., & Tonndorf, J. (1972). Tympanic membrane vibrations in cats studied by time-averaged holography. *J. Acoust. Soc. Am.*, *51*(6), 1904–1920.

Khanna, S. M., & Tonndorf, J. (1975). Tympanic membrane shape determined by moiré topography. *J. Acoust. Soc. Am.*, *57*(S1), S72–S72.

Kobrak, H. G. (1941). A cinematographic study of the conduction of sound in the human ear. *J. Acoust. Soc. Am.*, *13*(2), 179–181.

Kobrak, H. G. (1948). Construction material of the sound conduction system of the human ear. *J. Acoust. Soc. Am.*, *20*(2), 125–130.

Koike, T., Wada, H., & Kobayashi, T. (2002). Modeling of the human middle ear using the finite-element method. *J Acoust Soc Am*, *111*(3), 13.

Kose, O., Funnell, W. R. J., & Daniel, S. J. (2020). Vibration measurements of the gerbil eardrum under quasi-static pressure steps. *J. Assoc. Res. Otolaryngol.*, *21*(4), 287–302.

Kose, O., Funnell, W. R. J., & Daniel, S. J. (2021). Vibration measurements of the gerbil eardrum under quasi-static pressure sweeps. *J. Assoc. Res. Otolaryngol.*

de La Rochefoucauld, O., Decraemer, W. F., Khanna, S. M., & Olson, E. S. (2008). Simultaneous measurements of ossicular velocity and intracochlear pressure leading to the cochlear input impedance in gerbil. *J. Assoc. Res. Otolaryngol.*, *9*(2), 161–177.

de La Rochefoucauld, O., & Olson, E. S. (2010). A sum of simple and complex motions on the eardrum and manubrium in gerbil. *Hear. Res.*, *263*(1), 9–15.

Ladak, H. M., Decraemer, W. F., Dirckx, J. J., & Funnell, W. R. J. (2004). Response of the cat eardrum to static pressures: mobile versus immobile malleus. *J. Acoust. Soc. Am.*, *116*(5), 3008–3021.

Ladak, H. M., & Funnell, W. R. J. (1996). Finite-element modeling of the normal and surgically repaired cat middle ear. *J. Acoust. Soc. Am.*, *100*(2), 933–944.

Ladak, H. M., Funnell, W. R. J., Decraemer, W. F., & Dirckx, J. J. J. (2006). A geometrically nonlinear finite-element model of the cat eardrum. *J. Acoust. Soc. Am.*, *119*(5), 2859–2868.

Larsson, C., von Unge, M., Dirckx, J. J. J., Decraemer, W. F., & Bagger-Sjöbäck, D. (2001). Displacement pattern of the normal pars flaccida in the gerbil. *Otol. Neurotol.*, *22*(4), 558–566.

Lee, C.-Y., & Rosowski, J. J. (2001). Effects of middle-ear static pressure on pars tensa and pars flaccida of gerbil ears. *Hear. Res.*, *153*(1), 146–163.

Lidén, G., Björkman, G., & Peterson, J. L. (1972). Clinical equipment for measurement of middle-ear muscle reflexes and tympanometry. *J. Speech Hear. Disord.* Retrieved from https://pubs.asha.org/doi/abs/10.1044/jshd.3701.100

Lidén, G., Peterson, J. L., & Björkman, G. (1970). Tympanometry. *Arch. Otolaryngol.*, *92*(3), 248–257.

Lim, D. J. (1968a). Tympanic Membrane: Part I: Pars Tensa. *Acta Otolaryngol. (Stockh.)*, *66*(1–6), 181–198.

Lim, D. J. (1968b). Tympanic membrane Part II.: Pars flaccida. *Acta Otolaryngol. (Stockh.)*, *66*(1–6), 515–532. Taylor & Francis.

Liu, H., Ong, Y.-S., & Cai, J. (2018). A survey of adaptive sampling for global metamodeling in support of simulation-based complex engineering design. *Struct. Multidiscip. Optim.*, *57*(1), 393–416.

Maftoon, N., Funnell, W. R. J., Daniel, S. J., & Decraemer, W. F. (2013). Experimental study of vibrations of gerbil tympanic membrane with closed middle ear cavity. *J. Assoc. Res. Otolaryngol.*, *14*(4), 467–481.

Maftoon, N., Funnell, W. R. J., Daniel, S. J., & Decraemer, W. F. (2014). Effect of opening middle-ear cavity on vibrations of gerbil tympanic membrane. *J. Assoc. Res. Otolaryngol.*, *15*(3), 319–334.

Maftoon, N., Funnell, W. R. J., Daniel, S. J., & Decraemer, W. F. (2015). Finite-element modelling of the response of the gerbil middle ear to sound. *J. Assoc. Res. Otolaryngol.*, *16*(5), 547–567.

Maftoon, N., Nambiar, S., Funnell, W. R. J., Decraemer, W. F., & Daniel, S. J. (2011). Experimental and modelling study of gerbil tympanic-membrane vibrations. *34th Midwinter Res. Meet. Assoc. Res. Otolaryngol.* (pp. 19–23).

Manley, G. A., Irvine, D. R., & Johnstone, B. M. (1972). Frequency response of bat tympanic membrane. *Nature*, *237*, 112–113.

Manley, G. A., & Johnstone, B. M. (1974). Middle-ear function in the guinea pig. *J. Acoust. Soc. Am.*, *56*(2), 571–576.

Møller, A. R. (1963). Transfer function of the middle ear. *J. Acoust. Soc. Am.*, *35*(10), 1526–1534. Acoustical Society of America.

Møller, A. R. (1984). Neurophysiological basis of the acoustic middle-ear reflex. In S. Silman (Ed.), *Acoust. Reflex* (pp. 1–34). Academic Press. Retrieved from https://www.sciencedirect.com/science/article/pii/B9780126434507500068

Motallebzadeh, H., Charlebois, M., & Funnell, W. R. J. (2013). A non-linear viscoelastic model for the tympanic membrane. *J. Acoust. Soc. Am.*, *134*(6), 4427–4434.

Motallebzadeh, H., Maftoon, N., Pitaro, J., Funnell, W. R. J., & Daniel, S. J. (2017a). Finite-element modelling of the acoustic input admittance of the newborn ear canal and middle ear. *J. Assoc. Res. Otolaryngol.*, *18*(1), 25–48.

Motallebzadeh, H., Maftoon, N., Pitaro, J., Funnell, W. R. J., & Daniel, S. J. (2017b). Fluid-structure finite-element modelling and clinical measurement of the wideband acoustic input admittance of the newborn ear canal and middle ear. *J. Assoc. Res. Otolaryngol.*, *18*(5), 671–686.

Motallebzadeh, H., & Puria, S. (2021). Mouse middle-ear forward and reverse acoustics. *J. Acoust. Soc. Am.*, *149*(4), 2711–2731. Acoustical Society of America.

Murakami, S., Gyo, K., & Goode, R. L. (1997). Effect of middle ear pressure change on middle ear mechanics. *Acta Otolaryngol. (Stockh.)*, *117*(3), 390–395. Taylor & Francis.

Muyshondt, P. G. G., & Dirckx, J. J. J. (2021). Structural stiffening in the human middle ear due to static pressure: Finite-element analysis of combined static and dynamic middle-ear behavior. *Hear. Res.*, *400*, 108116.

Myers, J., Joseph Kei, Sreedevi Aithal, Venkatesh Aithal, Driscoll Carlie, Khan Asaduzzaman, Alehandrea Manuel, Anjali Joseph, & Alicja N. Malicka. (2019). Diagnosing conductive dysfunction in infants using wideband acoustic immittance: Validation and development of predictive models. *J. Speech Lang. Hear. Res.*, *62*(9), 3607–3619. American Speech-Language-Hearing Association.

Park, M. K. (2017). Clinical applications of wideband tympanometry. *Korean J Otorhinolaryngol-Head Neck Surg*, *60*(8), 375–380. Korean Society of Otolaryngology-Head and Neck Surgery.

Peterson, J. L., & Lidén, G. (1970). Tympanometry in human temporal bones. *Arch. Otolaryngol.*, *92*(3), 258–266.

Polytec. (2015). Hearing Laser Vibrometer (HLV).

Prendergast, P. J., Ferris, P., Rice, H. J., & Blayney, A. W. (1999). Vibro-acoustic modelling of the outer and middle ear using the finite-element method. *Audiol. Neurotol.*, *4*(3–4), 185–191.

Qi, L., Funnell, W. R. J., & Daniel, S. J. (2008). A nonlinear finite-element model of the newborn middle ear. *J. Acoust. Soc. Am.*, *124*(1), 337–347.

Qi, L., Liu, H., Lutfy, J., Funnell, W. R. J., & Daniel, S. J. (2006). A nonlinear finite-element model of the newborn ear canal. *J. Acoust. Soc. Am.*, *120*(6), 3789–3798.

Qi, L., Mikhael, C. S., & Funnell, W. R. J. (2005). Application of the Taguchi Method to sensitivity analysis of a middle-ear finite-element model. *CMBES Proc.*, *28*. Retrieved from https://proceedings.cmbes.ca/index.php/proceedings/article/view/471

Qian, T. (2020). *Finite-element modelling of middle-ear vibrations under quasi-static pressurization* (M.Eng. thesis). Montreal, Canada: McGill University.

Ravicz, M. E., & Rosowski, J. J. (1997a). Sound-power collection by the auditory periphery of the Mongolian gerbil *Meriones unguiculatus* : III. Effect of variations in middle-ear volume. *J. Acoust. Soc. Am.*, *101*(4), 2135–2147.

Ravicz, M. E., & Rosowski, J. J. (1997b). Sound-power collection by the auditory periphery of the mongolian gerbil Meriones unguiculatus: III. Effect of variations in middle-ear volume. *J. Acoust. Soc. Am.*, *101*(4), 2135–2147. Acoustical Society of America.

Ravicz, M. E., Rosowski, J. J., & Voigt, H. F. (1992). Sound-power collection by the auditory periphery of the mongolian gerbil Meriones unguiculatus. I: Middle-ear input impedance. *J. Acoust. Soc. Am.*, *92*(1), 157–177.

Ravicz, M. E., Rosowski, J. J., & Voigt, H. F. (1996). Sound-power collection by the auditory periphery of the mongolian gerbil Meriones unguiculatus. II. External-ear radiation impedance and power collection. *J. Acoust. Soc. Am.*, *99*(5), 3044–3063.

Rosowski, J., Cheng, J., Merchant, S., Harrington, E., & Furlong, C. (2011). New data on the motion of the normal and reconstructed tympanic membrane. *Otol. Neurotol. Off. Publ. Am. Otol. Soc. Am. Neurotol. Soc. Eur. Acad. Otol. Neurotol.*, *32*(9), 1559–1567.

Rosowski, J. J. (2013). Comparative middle ear structure and function in vertebrates. In S. Puria, R. R. Fay, & A. N. Popper (Eds.), *Middle Ear Sci. Otosurgery Technol.*, Springer

Handbook of Auditory Research (pp. 31–65). New York, NY: Springer. Retrieved from https://doi.org/10.1007/978-1-4614-6591-1_3

Rosowski, J. J., Cheng, J. T., Ravicz, M. E., Hulli, N., Hernandez-Montes, M., Harrington, E., & Furlong, C. (2009). Computer-assisted time-averaged holograms of the motion of the surface of the mammalian tympanic membrane with sound stimuli of 0.4-25 kHz. *Hear. Res.*, *253*(1–2), 83–96.

Rosowski, J. J., & Lee, C.-Y. (2002). The effect of immobilizing the gerbil's pars flaccida on the middle-ear's response to static pressure. *Hear. Res.*, *174*(1–2), 183–195.

Rosowski, J. J., Mehta, R. P., & Merchant, S. N. (2003). Diagnostic utility of laser-Doppler vibrometry in conductive hearing loss with normal tympanic membrane: *Otol. Neurotol.*, *24*(2), 165–175.

Rosowski, J. J., Ravicz, M. E., Teoh, S. W., & Flandermeyer, D. (1999). Measurements of middle-ear function in the Mongolian gerbil, a specialized mammalian ear. *Audiol. Neurotol.*, *4*(3–4), 129–136.

Rossi, G. L., & Tomasini, E. P. (1995). Hand-arm vibration measurement by a laser scanning vibrometer. *Measurement*, Vibration measurement by laser techniques, *16*(2), 113–124.

Roush, J., Bryant, K., Mundy, M., Zeisel, S., & Roberts, J. (1995). Developmental changes in static admittance and tympanometric width in infants and toddlers. *J. Am. Acad. Audiol.*, *6*(4), 334–338.

Salih, W. H. M., Soons, J. A. M., & Dirckx, J. J. J. (2016). 3D displacement of the middle ear ossicles in the quasi-static pressure regime using new X-ray stereoscopy technique. *Hear. Res.*, MEMRO 2015 – Basic Science meets Clinical Otology, *340*, 60–68.

Shahnaz, N., Longridge, N., & Bell, D. (2009). Wideband energy reflectance patterns in preoperative and post-operative otosclerotic ears. *Int. J. Audiol.*, *48*(5), 240–247. Taylor & Francis.

Shanks, J. E., & Wilson, R. H. (1986). Effects of direction and rate of ear-canal pressure changes on tympanometric measures. *J. Speech Lang. Hear. Res.*, *29*(1), 11–19. American Speech-Language-Hearing Association.

Shapiro, R. (2014). *An experimental study of vibrations in the gerbil middle ear under static pressure* (M.Eng. thesis). Montreal, Canada: McGill University. Retrieved from

http://digitool.library.mcgill.ca/R/-?func=dbin-jump-full&object_id=126993&silo_library=GEN01

Shimokura, R., Hosoi, H., Nishimura, T., Yamanaka, T., & Levitt, H. (2014). Cartilage conduction hearing. *J. Acoust. Soc. Am.*, *135*(4), 1959–1966.

Soleimani, M., Funnell, W. R. J., & Decraemer, W. F. (2018). A new finite-element model of the incudostapedial joint (p. 110003). Presented at the To The Ear And Back Again - Advances In Auditory Biophysics: Proceedings of the 13th Mechanics of Hearing Workshop, St Catharines, Canada. Retrieved from http://aip.scitation.org/doi/abs/10.1063/1.5038503

Soleimani, M., Funnell, W. R. J., & Decraemer, W. F. (2020). A non-linear viscoelastic model of the incudostapedial joint. *J. Assoc. Res. Otolaryngol.*, *21*(1), 21–32.

Spivak, L., & Sokol, H. (2005). Beyond newborn screening: Early diagnosis and management of hearing loss in infants. *Adv. Neonatal Care*, *5*(2), 104–112.

Stepp, C. E., & Voss, S. E. (2005). Acoustics of the human middle-ear air space. *J. Acoust. Soc. Am.*, *118*(2), 861–871.

Sun, Q., Gan, R. Z., Chang, K.-H., & Dormer, K. J. (2002). Computer-integrated finite element modeling of human middle ear. *Biomech. Model. Mechanobiol.*, *1*(2), 109–122.

Szucs, E., Diependaele, R., & Clement, P. A. (1995). The accuracy of tympanometry assessed by its sensitivity and specificity. *Acta Otorhinolaryngol. Belg.*, *49*(3), 287–292.

Tanno, G. A. Y., Santos, M. A. de O., Sanches, M. T. D., Durante, A. S., Almeida, K. de, Gameiro, M. S., Roque, N. M. C. de F., & Sousa Neto, O. M. de. (2020). Analysis of wideband tympanometry in Ménière's disease. *Braz. J. Otorhinolaryngol.* Retrieved from http://www.sciencedirect.com/science/article/pii/S1808869420301014

Teoh, S. W., Flandermeyer, D. T., & Rosowski, J. J. (1997). Effects of pars flaccida on sound conduction in ears of Mongolian gerbil: acoustic and anatomical measurements. *Hear. Res.*, *106*(1–2), 39–65.

Therkildsen, A. G., & Gaihede, M. (2005). Accuracy of tympanometric middle ear pressure determination: The role of direction and rate of pressure change with a fast, modern tympanometer. *Otol. Neurotol.*, *26*(2), 252–256.

Tirabassi, M., & Rothberg, S. J. (2009). Scanning LDV using wedge prisms. *Opt. Lasers Eng.*, Optical Measurements, *47*(3), 454–460.

Tonndorf, J., & Khanna, S. M. (1968). Submicroscopic Displacement Amplitudes of the Tympanic Membrane (Cat) Measured by a Laser Interferometer. *J. Acoust. Soc. Am.*, *44*(6), 1546–1554. Acoustical Society of America.

Tschoegl, N. W. (1989). *The phenomenological theory of linear viscoelastic behavior*. Berlin, Heidelberg: Springer Berlin Heidelberg. Retrieved from http://link.springer.com/10.1007/978-3-642-73602-5

von Unge, M., Bagger-Sjöbäck, D., & Borg, E. (1991). Mechanoacoustic properties of the tympanic membrane: a study on isolated Mongolian gerbil temporal bones. *Am. J. Otol.*, *12*(6), 407–419.

von Unge, M., Decraemer, W. F., Bagger-Sjöbäck, D., & Dirckx, J. J. (1993). Displacement of the gerbil tympanic membrane under static pressure variations measured with a real-time differential moire interferometer. *Hear. Res.*, *70*(2), 229–242.

Viana, F. A. C., Simpson, T. W., Balabanov, V., & Toropov, V. (2014). Special Section on Multidisciplinary Design Optimization: Metamodeling in Multidisciplinary Design Optimization: How Far Have We Really Come? *AIAA J.*, *52*(4), 670–690.

Wada, H., Metoki, T., & Kobayashi, T. (1992). Analysis of dynamic behavior of human middle ear using a finite-element method. *J. Acoust. Soc. Am.*, *92*(6), 3157–3168.

Wang, B., Ghanta, P., Vinnikova, S., Bao, S., Liang, J., Lu, H., & Wang, S. (2017). Wrinkling of tympanic membrane under unbalanced pressure. *J. Appl. Mech.*, *84*(4), 041002.

Wang, X., Cheng, T., & Gan, R. Z. (2007). Finite-element analysis of middle-ear pressure effects on static and dynamic behavior of human ear. *J. Acoust. Soc. Am.*, *122*(2), 906–917.

Warnholtz, B., Schär, M., Sackmann, B., Lauxmann, M., Chatzimichalis, M., Prochazka, L., Dobrev, I., Huber, A. M., & Sim, J. H. (2021). Contribution of the flexible incudo-malleal joint to middle-ear sound transmission under static pressure loads. *Hear. Res.*, 108272.

Winerman, I., Nathan, H., & Arensburg, B. (1980). Posterior ligament of the incus: variations in its components. *Ear. Nose. Throat J.*, *59*(5), 227–231.

Yeh, Y., & Cummins, H. Z. (2004). Localized fluid-flow measurements with an He-Ne laser spectrometer. *Appl. Phys. Lett.*, *4*(10), 176. American Institute of PhysicsAIP.

Zhang, J., Jiao, C., Zou, D., Ta, N., & Rao, Z. (2020). Assigning viscoelastic and hyperelastic properties to the middle-ear soft tissues for sound transmission. *Biomech. Model. Mechanobiol.*, *19*(3), 957–970.

Zienkiewicz, O. C., Taylor, R. L., & Zhu, J. Z. (2013). *The finite element method: Its basis and fundamentals* (7th ed.). Butterworth-Heinemann. Retrieved from https://www.elsevier.com/books/the-finite-element-method-its-basis-and-fundamentals/zienkiewicz/978-1-85617-633-0

Zwillenberg, D., Konkle, D. F., & Saunders, J. C. (1981). Measures of middle ear admittance during experimentally induced changes in middle ear volume in the hamster. *Otolaryngol.--Head Neck Surg. Off. J. Am. Acad. Otolaryngol.-Head Neck Surg.*, *89*(5), 856–860.

# Appendix: Figure source

*A1: Reproduced from [Bergevin, C., & Olson, E. S. (2014). External and middle ear sound pressure distribution and acoustic coupling to the tympanic membrane. The Journal of the Acoustical Society of America, 135(3), 1294–1312], with the permission of AIP Publishing*